Progress in Materials Science 124 (2022) 100872

Contents lists available at ScienceDirect

Progress in Materials Science

journal homepage: www.elsevier.com/locate/pmatsci

Manganese-based permanent magnet materials

Thomas Keller, Ian Baker *

Thayer School of Engineering, Dartmouth College, Hanover, NH 03755, USA

ARTICLE INFO

Keywords:
Permanent magnets
Processing
Magnetic properties
Mn-Al
Mn-Bi
Mn-Ga

ABSTRACT

Manganese-based permanent magnetic materials have become an area of significant research activity in recent years as a potential alternative to permanent magnets based on Rare Earth (RE) metals. Manganese compounds are capable of achieving a relatively high energy product, **BH**, when processed to have a strong texture. Research has identified three promising compounds for Mn-based permanent magnets: Mn-Ga, Mn-Bi, and Mn-Al. While calculations show that these compounds cannot achieve the theoretical maximum energy products, $(\mathbf{BH})_{max}$, of RE magnets, current research suggests than they can fill the property gap between inexpensive, but low-performance, ferrites and expensive high-performance RE magnets. Many researchers have produced Mn-based magnets through a variety of methods that fall into three basic categories: bulk processing, particulate processing, and thin film deposition. This review discusses the various processing methods for each compound and their impact on the microstructure and resulting magnetic properties. We also present unresolved questions and outline opportunities for future research.

1. Introduction

Rare-earth based magnets are prevalent in high-performance permanent magnet applications, such as motors for electric and hybrid vehicles or wind turbine generators, due to their high theoretical maximum energy product ($(\mathbf{BH})_{max}$), 358 kJ/m^3 for Nd-Fe-B and 255 kJ/m^3 for Sm-Co magnets [1]. The energy product, **BH** is defined as the product of the magnetic field, H (SI units A/m), and the magnetic flux density, B (SI units tesla). In SI units, the two are related by the formula: $B = \mu_0(H + M)$ where M is the magnetization (SI units A/m) and μ_0 is the permeability of free space (see appendix for CGS to SI unit conversions) [2]. However, rare-earth based magnets have high apparent costs due to the costs of extracting and refining the raw materials. Neodymium is estimated to make up 0.00415% of the earth's crust (a unit equivalent to 41.5 parts per million) while samarium is 0.000705% [3]. These magnets also bear the hidden costs of environmental degradation due to the required mining practices and lack of recycled material, and the possibility for supply chain disruption due to the lack of geographically diverse production [4]. Other magnet types, such as ferrites, are very low cost and are composed of abundant raw materials but lack the magnetic properties for high-performance applications due to their relatively low $(\mathbf{BH})_{max}$ of around 30 kJ/m^3. This gap, between expensive high-performance rare-earth magnets and low-cost low-performance alternatives presents an opportunity for Mn-based alternatives to fill the divide.

The three main Mn compounds of interest reviewed in this paper are Mn-Ga, Mn-Bi, and Mn-Al. In the U.S in 2019, 99.7% pure manganese flake cost roughly $2.15/kg, $7.50/kg for 99.99% bismuth, and $2.20/kg for aluminum [4]. Comparing this with 99.5% neodymium at $45/kg, it is apparent how Mn-Al and Mn-Bi-based magnets have a strong cost incentive compared to RE magnets. We also note that since 99.99% gallium costs $150/kg there is less economic incentive to develop bulk Mn-Ga-based magnets.

* Corresponding author.
E-mail addresses: thomas.r.keller.th@dartmouth.edu (T. Keller), ian.baker@dartmouth.edu (I. Baker).

https://doi.org/10.1016/j.pmatsci.2021.100872
Received 10 June 2021; Received in revised form 22 September 2021; Accepted 27 September 2021
Available online 29 September 2021

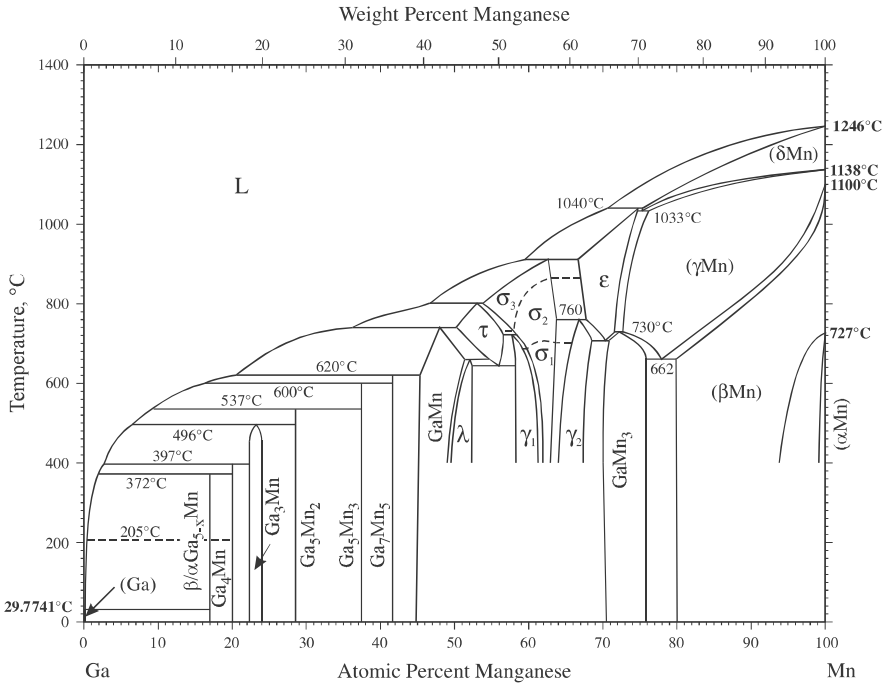

Fig. 1. Binary Mn-Ga phase diagram showing the MnGa ($L1_0$) and Mn_3Ga ($D0_{22}$) phase regions. From [14].

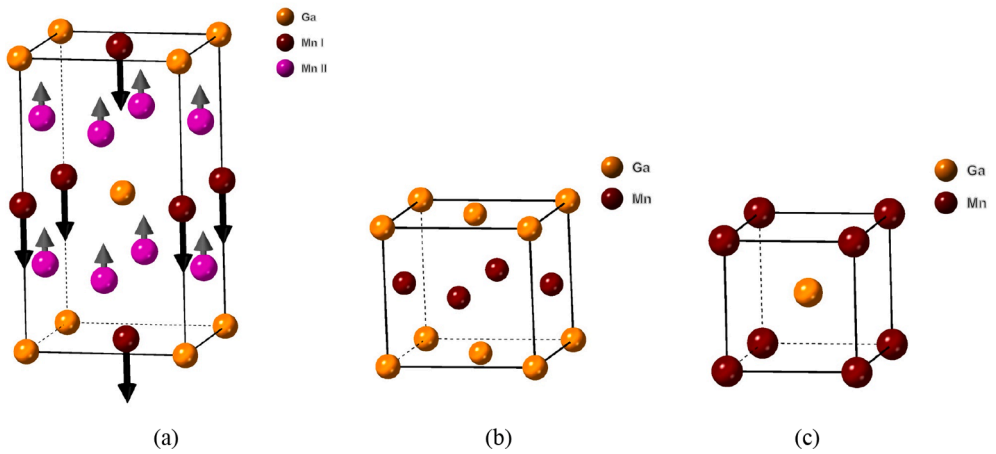

Fig. 2. The unit cells of the two most promising Mn-Ga phases for permanent magnet applications: (a) $D0_{22}$ Mn_3Ga, and $L1_0$ MnGa. The latter is shown both as (b) base-centered tetragonal and (c) simple tetragonal. The $D0_{22}$ ferrimagnetic dipole moments are shown as arrows.

There is also an argument that, given the lack of abundant or geographically diverse production of RE elements paired with the current shift towards permanent-magnet motors in electric cars and generators, the future cost of RE elements is likely going to increase or become volatile due to an imbalance between supply and demand. Compare this to an exceptionally abundant element like Al (8.23% of the earth's crust), for which roughly 45% of U.S. consumption demand is met by discarded scrap aluminum products alone, and a more stable forecast of raw material supply chains can be imagined [4]. Mn is also relatively abundant (0.095% of the earth's crust), while Ga is less common (0.0019%) and Bi is rare (8.5×10^{-7}%)[3]. Beyond the economic terms, this review will now focus on the material and magnetic properties of the compounds in question. The review is set out as follows: we discuss magnets based on Mn-Ga, Mn-Bi, and Mn-Al; for each system we relate the magnetic moments to the crystal structure and consider the phase equilibria before focusing on processing as bulk material, particulates, and thin films.

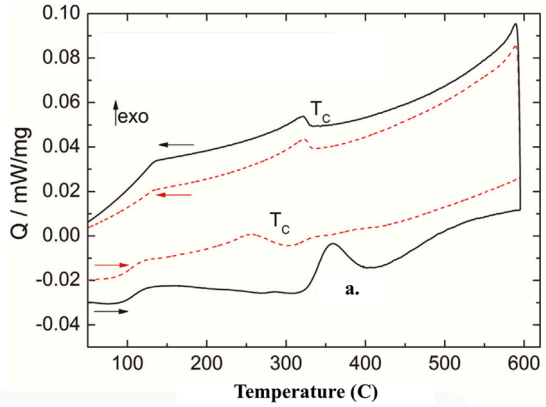

Fig. 3. DSC curves at a heating and cooling rate of 5 K/min in Ar for the formation of the $L1_0$ phase (exotherm a.) starting from the rhombohedral τ phase (solid line), and DSC curves of $L1_0$ phase indicating its stability (dashed line). T_C indicates the Curie temperature. From [15].

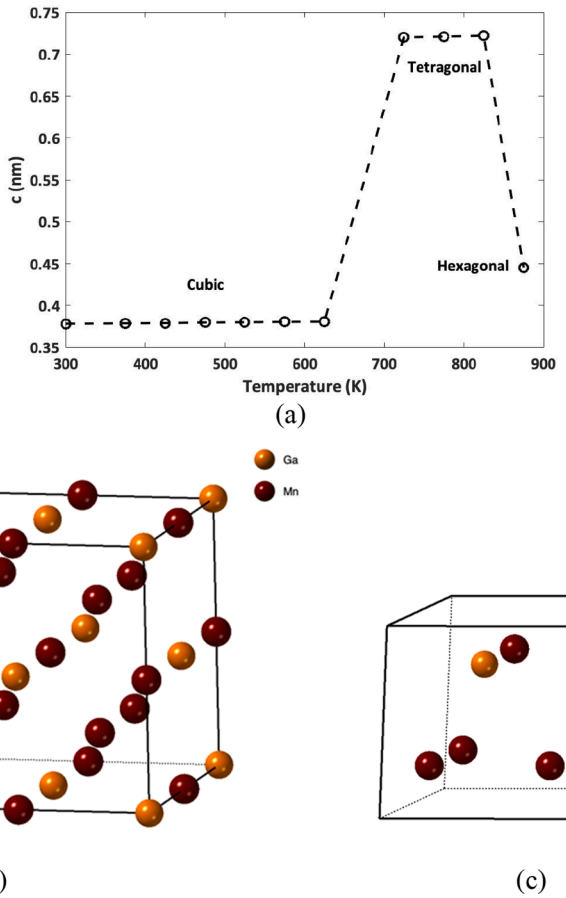

Fig. 4. The calculated c-axis lattice parameter from XRD analysis at various temperatures showing the formation of the tetragonal $D0_{22}$ phase from the cubic $L2_1$ phase equivalent to $D0_3$ (b) and decomposition into $D0_{19}$ phase (c). Redrawn (a) from [16] with permission, © IOP Publishing. All rights reserved.

2. Manganese-Gallium based magnetic materials

2.1. Mn-Ga crystal structure and phase equilibria

There are numerous intermetallic compounds formed between Mn and Ga, see Fig. 1. Several phases of the Mn-Ga binary system exhibit magnetic properties, but research has focused on two crystal structures for permanent magnet applications: the ferromagnetic

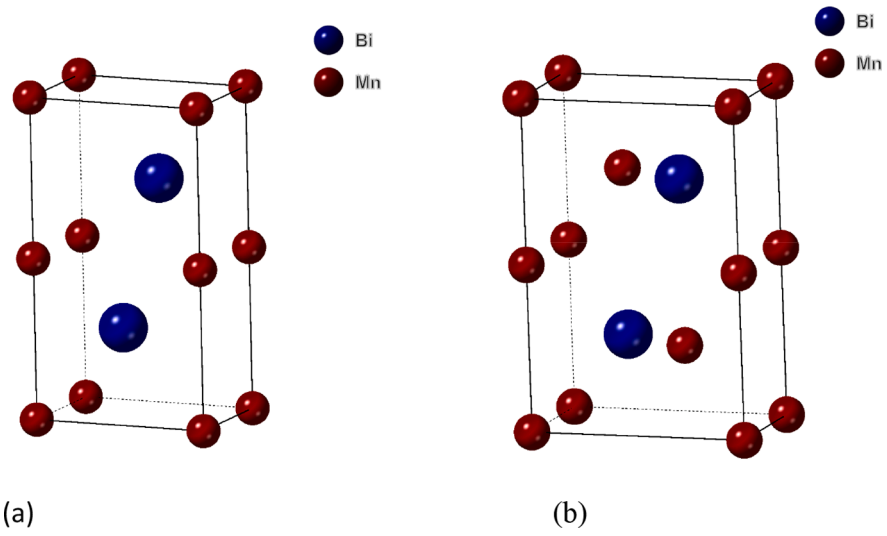

Fig. 5. The unit cells of the two most promising magnetic phases of Mn-Bi for permanent magnet applications: (a) $B8_1$ MnBi LTP and (b) $B8_2$ $Mn_{52}Bi_{48}$ HTP.

(FM) tetragonal $L1_0$ phase and the ferrimagnetic tetragonal $D0_{22}$ phase, see in Fig. 2. Generally speaking, the $L1_0$ phase corresponds to the roughly equi-atomic fraction region of the phase diagram, MnGa, while the $D0_{22}$ phase occurs in the Mn_3Ga region [5]. However, consensus on the exact phase boundaries for Mn-Ga has yet to be reached.

The ferrimagnetic $D0_{22}$ unit cell has lattice parameters $a = 0.391$ nm and $c = 0.710$–0.717 nm [6–8], see Fig. 2(a), with the c parameter increasing with an increase in Ga content. There are two types of Mn atoms in the unit cell with opposing orientations of their magnetizations, Mn_I and Mn_{II}, with magnetic moments of -2.8 μ_B and 1.6 μ_B respectively, see Fig. 2(a) [9,6,7]. The theoretical $(\mathbf{BH})_{max}$ has been reported to be ~143 kJ/m^3 at a density of 7180 kg/m^3, a saturation magnetization of 0.26 μ_B per Mn atom, and uniaxial magneto-crystalline anisotropy energy of 1 MJ/m^3 [8].

The ferromagnetic $L1_0$ structure is highly magnetically anisotropic when the ratio of Mn to Ga atoms is unity. At 63 at.% Mn, the $L1_0$ unit cell (Fig. 2(b)) has lattice parameters $a = 0.390$ nm and $c = 0.363$ nm [6]. The compound can also be drawn as a simple tetragonal unit cell (Fig. 2(c)), with $a = 0.274$ nm and $c = 0.369$ at 54.5 at.% Mn, and $c = 0.358$ at 70 at.% Mn [10]. Both depictions of the unit cell are shown in Fig. 2. The magnetic moment of each Mn atom along the c-axis is 2.51 μ_B, while the oppositely-oriented Ga atom has a magnetic moment of -0.09 μ_B resulting in a magneto-crystalline anisotropy of 2.6 MJ/m^3 [11]. The theoretical saturation magnetization, M_s, is ~116 Am^2/kg, which implies a $(\mathbf{BH})_{max}$ of ~223 kJ/m^3 at a density of 7300 kg/m^3 [12,13].

The equilibrium tetragonal MnGa $L1_0$ phase forms below 1045 K from a peritectic reaction between the liquid and τ phases, within a limited range of Ga concentration from ~45–52 at.%. Mix *et al.* performed differential scanning calorimetry (DSC) analysis to examine the formation of the $L1_0$ phase in a $Mn_{55}Ga_{45}$ alloy, see Fig. 3 [15]. Starting with a sample composed of quenched-in high-temperature τ phase (see Fig. 1), they found upon heating that the transformation from the τ phase to the $L1_0$ phase occurred at 630 K. Upon cooling, no reverse transformation to τ phase occurred, only a reversible peak at the Curie temperature, T_C. They repeated the analysis starting with the $L1_0$ phase and did not see a transformation back to the τ phase, indicating that a stable $L1_0$ phase can be formed by simply heating as-cast τ phase material to above the temperature of the transformation and cooling. They observed that the $L1_0$ phase began to transform into τ phase at 928 K in the $Mn_{55}Ga_{45}$ alloy and that the transformation is reversible.

Depending on the composition, in the range from 24 to 30 at.% Ga, the Mn_3Ga phase forms from either the high temperature ε or γ-Mn phases when cooled below 1003 K. However, three crystal structures have been observed in the Mn_3Ga phase region: hexagonal, tetragonal, and cubic (see Figs. 2 and 5). Kharel *et al.* found that the formation of the different Mn_3Ga structures depends on the thermal treatment. Starting with a rapidly-quenched ribbon, they obtained X-ray diffractometry (XRD) patterns at various increasing temperatures and plotted the resulting c lattice parameter as shown in Fig. 4 [16]. The as-quenched ribbon showed a cubic $L2_1$ structure, which transformed into a tetragonal $D0_{22}$ structure beginning at ~600 K. This further transformed into a hexagonal $D0_{19}$ structure beginning at ~800 K. They confirmed that this hexagonal phase remained present upon cooling back to room temperature. However, related work has also shown that if the tetragonal $D0_{22}$ phase is formed by annealing and not heated above 800 K, the $D0_{22}$ structure remains when cooled back to room temperature [17]. This indicates that the tetragonal phase is relatively stable down to room temperature and can be produced from annealing the high-temperature cubic phase below 800 K. It is worth noting that T_C of the $D0_{22}$ phase has not been experimentally determined as it is greater than the temperature of transition to the $D0_{19}$ phase [18]. Further research in the structure and stability of the three Mn_3Ga phases is needed to fully understand the preparation of the $D0_{22}$ phase for permanent magnet applications.

2.2. Mn-Ga bulk processing

Due to the relative scarcity and high cost of gallium noted earlier, bulk processing of large Mn-Ga permanent magnets faces the hurdle of economic viability. Despite this, notable research has used two different processing methodologies for Mn-Ga: heat treatment of a cast ingot and consolidating powder into a bulk magnet.

For ingots, high purity Ga and Mn are typically melted in an arc furnace under an argon atmosphere. The as-cast ingot is then annealed to homogenize the ingot and produce either of the desired magnetic phases, MnGa ($L1_0$) or Mn_3Ga ($D0_{22}$). To form the $L1_0$ phase, the annealing is performed under argon at 723–923 K, followed by furnace cooling [12,15]. Mix *et al.* found that annealing bulk $Mn_{55}Ga_{45}$ at 723 K for 7 days and then furnace cooling to room temperature at a rate of 5 K/min produced poorly ordered single-phase $L1_0$ MnGa with a low M_s of 62 Am^2/kg under a 4 MA/m applied field (abbreviated $M_{4MA/m}$ to show the saturating field under which the measurement was carried out) [15]. To improve M_s, they raised the annealing temperature to 973 K, which is above the $L1_0$ to τ phase transition, for the same duration and rate of furnace cooling. This method produced a magnet with a higher saturation magnetization of $M_{4MA/m}$ = 85 Am^2/kg. This suggests that annealing slightly above the transformation temperature is effective at speeding up diffusion but also enables a reversible transformation back into $L1_0$ phase upon cooling to room temperature at 5 K/min. Since the anneal is taking place at the equilibrium temperature of the τ phase, this implies that the long anneal duration is beneficial to the formation of homogeneous τ phase and the transformation to the $L1_0$ phase appears to occur during the slow cooling. Lu *et al.* observed that the optimum annealing temperature may depend on the composition, and that the $L1_0$ phase can be formed without the furnace cooling technique [12]. They performed 7 day anneals at 700–900 K and quenched the samples in ice water. They determined optimal annealing conditions for each composition: for $Mn_{54}Ga_{46}$, this was 740 K, for $Mn_{57}Ga_{43}$, 870 K, and for $Mn_{60}Ga_{40}$, 885 K. They noted that while optimizing the annealing temperature was critical to forming well-ordered $L1_0$ phase, anneal time was not significant and there was no difference between samples annealed for 2 or 7 days. The $M_{11MA/m}$ values, measured at 5 K, were 92, 86, and 70 Am^2/kg, respectively. This drop in M_s with increasing Mn content is attributed to antiferromagnetic (AFM) coupling between excess Mn atoms sitting substitutionally on Ga sites in the $L1_0$ structure [19].

Mix *et al.* showed that milling a bulk $L1_0$ ingot into a powder can greatly increase H_c [15]. They observed that upon vibration-milling the powder to particles of diameter <100 μm, the H_c of the $Mn_{55}Ga_{45}$ alloy increased dramatically from 17 kA/m in the bulk to 313 kA/m in the powder form. However, this was accompanied by a decrease in $M_{4MA/m}$ from 85 Am^2/kg in the bulk to 63 Am^2/kg in the powder. They observed that the resulting powder particles were polycrystalline and showed significant densities of twin defects. They concluded that the defects, introduced during the milling process, served as domain wall pinning sites and this resulted in increased H_c but reduced M_s. They also observed that the c/a ratio of the tetragonal $L1_0$ structure was significantly lower in the milled powder, $c/a = 0.9077$, than in the original bulk material, $c/a = 0.9486$. Since Yang *et al.* indicated that the distance between Mn atom sites is responsible for the magnitude of the magnetic moment per Mn atom, then it follows that the decrease in c/a for the milled powder is one factor responsible for the decrease in M_s compared to the bulk [10]. Upon annealing the powder at 673 K for 1 h and quenching they observed a restoration of $M_{4MA/m}$ to 85 kA/m, nearly identical to the original bulk, but a reduction of the improved H_c to 173 kA/m. They also found that the c/a ratio increased to greater than the original bulk value, $c/a = 0.9574$, showing that the annealing relaxed the tetragonal distortion caused by milling. They concluded that the reduced H_c was evidence that the annealing had relieved the crystal of a significant portion of the defects introduced by milling.

Mix *et al.* then explored the effects of hot compacting the $L1_0$ phase powder into a bulk form under 300 MPa of uniaxial compression at 673 K to an 83% packing density for the $Mn_{55}Ga_{45}$ alloy, and at 973 K to a 99% packing density for a $Mn_{60}Ga_{40}$ alloy [15]. They observed no significant change in magnetization per unit mass from the powder to the hot compacted sample when normalized by the density. However, the hot compaction process decreased the H_c of the $Mn_{55}Ga_{45}$ alloy from 173 to 127 kA/m and the $Mn_{60}Ga_{40}$ from 299 to 218 kA/m. These data suggest that the hot compaction further removed the defects serving as domain wall pins just as it had during the annealing of the powder in the preceding paragraph. Therefore, it is possible to greatly improve the H_c of the bulk $L1_0$ Mn-Ga through milling and hot compaction with a minimized loss of magnetization, but the anneal and hot compaction required to retain magnetization cannot prevent a H_c reduction compared to the milled powder.

Lu *et al.* examined the effects of uniaxial hot compression under 500 MPa at 873 K of a bulk $Mn_{64}Ga_{36}$ ingot without an intermediate milling step [12]. Unlike Mix *et al.* [15], this study showed that the c/a ratio before and after hot compression was the same, suggesting that the hot compaction process without milling does not significantly affect the tetragonal structure compared to milling. They observed that $M_{2.4MA/m}$ was fairly constant, but that H_c, remanent magnetization (M_r), and $(\mathbf{BH})_{max}$ all increased with increased hot compression, up to their maxima at 92% strain. Their observation of relatively constant M_s after various degrees of deformation concurs with their observation of the relatively constant c/a ratio, i.e. the tetragonal structure was not significantly changed and, thus, M_s remained unchanged.

Preparation of bulk $D0_{22}$ ingots generally consisted of the arc-melting procedure under Ar stated above for $L1_0$ ingots, followed by long anneals at 623–723 K for 7–14 days [9,18,7]. For $Mn_{75}Ga_{25}$ ingots, Balke *et al.* performed a 673 K anneal for 7 days, while Winterlik *et al.* performed a 623 K anneal for 14 days followed by an ice water quench. The longer anneal at 623 K and quench yielded a much higher H_c of 383 kA/m than the shorter 673 K anneal without quench, 289 kA/m. Additionally, Balke *et al.* reported a c lattice parameter of 0.7088 nm and M_s per Mn atom of 0.25 μ_B, while Winterlik *et al.* reported a slightly larger c lattice parameter of 0.7098 nm and M_s per Mn atom of 0.26 μ_B. Winterlik *et al.* also observed that decreasing the Mn content increased the c lattice parameter, the c/a ratio, and the M_s per Mn atom to 0.47 μ_B for $Mn_{65}Ga_{35}$. They attributed this increase in M_s to a reduction of the Mn atoms in the Mn_I position rather than in the Mn_{II} position of the $D0_{22}$ unit cell with decreasing Mn content, see Fig. 2(a). This decreased the ferrimagnetic mismatch between atomic Mn dipoles and improved the net M_s overall. Therefore, the method of Winterlik is shown to improve the magnetization of the $D0_{22}$ phase while also slightly improving the H_c. The improvement in H_c may be due to the quenching process, which prevents excessive grain growth that may be detrimental to H_c [20].

Table 1
Composition, phase, method, and magnetic properties for selected Mn-Ga bulk magnets.

Reference	Composition	Phase	Processing Technique	H_c *kA/m*	M_r *Am^2/kg*	M_s *Am^2/kg* (Saturating Field *kA/m*)	BH_{max} *kJ/m^3*	T_{curie} *K*
Lu *et al.* 2019 [12]	$Mn_{64}Ga_{36}$	$L1_0$	873 K anneal for 5 days then hot deformation at 873 K to 92%	376	32 *		11.3	
Mix *et al.* 2015 [15]	$Mn_{55}Ga_{45}$	$L1_0$	923 K anneal for 7 days then furnace cooled	16.7		87.97 (11141) and 85.03 (3979) *		610
"	"	$L1_0$	Hot compacted at 623 K	127		72.06 (3979) *		
"	$Mn_{60}Ga_{40}$	$L1_0$	723 K anneal for 7 days and furnace cooled	58.1		75.00 (11141) and 68.90 (3979) *		653
"	"	$L1_0$	Hot compacted at 923 K	218		68.24 (3979) *		
"	$Mn_{65}Ga_{35}$	$L1_0$	723 K anneal for 7 days and furnace cooled	93.9		58.10 (11141) *		704
Balke *et al.* 2007 [18]	$Mn_{75}Ga_{25}$	$D0_{22}$	673 K anneal for 7 days	289	0.145 T (Br)			>730
Ener *et al.* 2015 [21]	$Mn_{70}Ga_{30}$	$D0_{22}$	Cold-rolled then magnetic field-assisted 730 K anneal for 1 day under 796 kA/m field	987 (‖)	26.5 (‖) *			
Kren and Kadar 1970 [9]	$Mn_{71}Ga_{29}$	$D0_{22}$	750 K anneal for 7 days					>770
Wei *et al.* 2014 [8]	$Mn_{75}Ga_{25}$	$D0_{22}$	Pulverized sample pressed under 1.14 GPa into 1 mm thick 11.5 mm diameter discs then 673 K anneal for 14 days	1448		22.3 (5570)		
"	$Mn_{65}Ga_{35}$	$D0_{22}$	"	429		55.5 (5570)		
Winterlik *et al.* 2008 [7]	$Mn_{75}Ga_{25}$	$D0_{22}$	623 K anneal for 14 days then ice water quench	383 (453 at 5 K)	0.133 T (B_r) (0.137 T at 5 K)		14.4 (18.3 at 5 K)	>779
"	$Mn_{67}Ga_{33}$	$D0_{22}$	"	102 at 5 K	0.099 T at 5 K (B_r)		2.4 (at 5 K)	>723

Note: Magnetic properties are for room temperature and isotropic unless otherwise noted.
* Moment is converted from emu/cm^3 or kA/m using a density of 7300 kg/m^3 for the $L1_0$ phase and 7180 kg/m^3 for the $D0_{22}$ phase.
(⊥) Indicates measurement indicates perpendicular to direction of magnetic alignment during annealing or bonding.
(‖) Indicates measurement parallel to direction of magnetic alignment during annealing or bonding.

Ener et al. prepared bulk $D0_{22}$ $Mn_{70}Ga_{30}$ by cold rolling an ingot followed by magnetic field-assisted annealing at 650–750 K for 2 or 24 h under a field of 0 or 796 kA/m [21]. They observed that cold rolling and annealing at 700 K under 0 applied field for 2 h improved both the H_c and M_r (462 kA/m and 21 Am^2/kg) compared with un-rolled and similarly annealed samples (~260 kA/m and ~8 Am^2/kg). The H_c and M_r of the cold-rolled samples was significantly improved by the magnetic field-assisted annealing (an improvement of ~200kA/m and ~4 Am^2/kg with some variation depending on annealing temperature), whereas the un-rolled samples did not show a significant improvement with the addition of the magnetic field during annealing. The high temperature $D0_{19}$ phase dominated their as-cast ingots, thus they required nucleation and growth of the $D0_{22}$ phase within this existing matrix through an annealing treatment. By examining the microstructure with magneto-optical Kerr microscopy, they concluded that the external magnetic field increased the nucleation rate of the $D0_{22}$ phase. This was shown by refinement of the magnetic grains compared to the sample annealed without an applied field. This allowed the phase to form concurrently throughout the bulk in a more uniform fashion and resulted in a decreased average grain size and improved phase fraction. Cold rolling also introduced a high number of defects which likely served as nucleation sites for the $D0_{22}$ phase, further improving the nucleation rate and explaining why both H_c and M_r were improved concurrently compared to the cast ingot. Optimal H_c and M_r (987 kA/m and 26.5 Am^2/kg), were observed in the cold rolled sample annealed at 730 K for 24 h under a 796 kA/m field.

Wei *et al.* pulverized an arc-melted ingot consisting of the cubic $L2_1$ phase into a powder, compressed it into a pellet under a uniaxial stress of 1.14 GPa, and then subjected it to the same 623 K 14 day anneal as Winterlik *et al.,* but without the ice-water quench. This resulted in a H_c of 1448 kA/m, i.e. roughly 3.8 times the value observed by Winterlik [8]. However, the increased H_c came at the expense of M_s, at 22 Am^2/kg, i.e. well below the theoretical limit of 116 Am^2/kg. This combined with evidence of retained cubic phase present in their XRD analysis suggests that only a small fraction of $D0_{22}$ phase was produced by this method, and the retained cubic phase prevented a high M_s. It is also likely that the pulverization process used to turn the ingot into a powder imparted defects into the structure that increased H_c. (see Table 1).

2.3. Mn-Ga particulate processing

The melt-spinning approach allows for a thin ribbon of material to be produced and gas quenched at a high rate of cooling in one simultaneous step. Gong *et al.* produced melt-spun ribbons by dispensing the molten compound onto a copper wheel rotating at 30 m.

s^{-1} in an Ar environment. The as-spun ribbons were then annealed at 723 K for 1 h and ice water quenched [22]. They produced ribbons of both $Mn_{65}Ga_{35}$ ($L1_0$ phase) and $Mn_{75}Ga_{25}$ ($D0_{22}$ phase) and observed that the $D0_{22}$ phase exhibited much higher H_c and lower M_s than the $L1_0$ phase (see Table 2). A Henkel plot analysis of the two different magnetic phase responses revealed that the $L1_0$ phase had strong intergranular coupling, whereby the nucleation of magnetic domains can spread easily from grain to grain. In contrast, the $D0_{22}$ phase exhibited resistance to cooperative magnetization throughout the grains, indicating that the domain walls were being pinned. XRD and transmission electron microscopy (TEM) analysis of the $D0_{22}$ phase revealed secondary Ga-rich phase regions at the grain boundaries, which they determined was likely the cause of the domain wall pinning and, hence, the increased H_c. Similar work by Saito and Nishimura on $Mn_{50+x}Ga_{50-x}$ (x = 0–30) examined the effect of subjecting 50 $m.s^{-1}$ melt-spun ribbons to a higher temperature at 973 K anneal for 1 h and demonstrated that the magnetic performance is highly sensitive to the composition [23]. The as-cast $Mn_{50}Ga_{50}$ ribbon consisted of $L1_0$ and off-stoichiometric Mn_8Ga_5 phases in roughly equal proportion. However, after the 973 K anneal the ribbon consisted of very poorly-ordered $L1_0$ phase, with remanence <5 Am^2/kg, but no Mn_8Ga_5 phase was retained. This suggested that the material had transformed into a homogeneous high temperature phase but did not have sufficient time to reorder into the $L1_0$ phase upon cooling, concurring with the DSC analysis mentioned earlier about the instability of the $L1_0$ phase above 928 K [15]. The as-cast $Mn_{60}Ga_{40}$ ribbon consisted of only Mn_8Ga_5 phase and was unchanged by the anneal. Likewise, the $Mn_{80}Ga_{20}$ ribbon was composed of the γ-Mn phase and transformed into a mix of γ-Mn and β-Mn after the anneal. The $Mn_{70}Ga_{30}$ ribbon, by contrast, consisted of the $D0_{19}$ phase in the as-cast ribbon. After annealing this transformed into a majority of $D0_{22}$ phase and a minority fraction of β-Mn. However, the low M_r of this ribbon, 9 Am^2/kg, and high H_c, 454 kA/m, demonstrate the poor ordering of the $D0_{22}$ phase by this method. Liu *et al.* performed a very similar experiment on $Mn_{70}Ga_{30}$ ribbons spun at 50 $m.s^{-1}$ [24]. In this experiment, the ribbon was annealed at 873 K for 1 h, 100 K lower than Saito and Nishimura, resulting in H_c = 535 kA/m and M_r = 6.15 Am^2/kg. The slight improvement in H_c at the expense of M_r may be due to reduced grain growth of the $D0_{22}$ phase by annealing at lower temperature or by the formation of Ga-rich phase regions at the grain boundaries as observed by Gong *et al.*, but Liu *et al.* presented insufficient phase and microstructural data to conclusively determine the cause. The aforementioned observations by Kharel *et al.* indicate that a more suitable heat treatment below 800 K would produce a better ordered $D0_{22}$ phase and prevent decomposition into the β-Mn phase [17].

Cui *et al.* analyzed $Mn_{56}Ga_{44}$ powder high-energy ball milled for 6 h under Ar [20]. The as-milled powders displayed a mix of $L1_0$ phase as well as an undesirable Mn_8Ga_5 secondary phase by XRD analysis. Annealing at 675–923 K for 2 min was sufficient to fully transform the secondary phase into the $L1_0$ phase but annealing above this temperature retained a fraction of the secondary phase upon cooling. They observed that as the annealing temperature was increased from 675 to 923 K, the *c* lattice parameter increased, and this was suggested to be evidence of improved long-range ordering of the $L1_0$ phase. The average grain size also increased with increasing temperature and a grain size above 50 nm at 923 K was linked to a distinct decrease in the H_c of the sample while M_s remained fairly unchanged. Optimum magnetic properties were achieved by annealing at 873 K for 20 min (H_c = 493 kA/m, M_s = 61 Am^2/kg).

Table 2
Composition, phase, method, and magnetic properties for selected Mn-Ga particulate magnets.

Reference	Composition	Phase	Processing Technique	H_c *kA/m*	M_r *Am^2/kg*	M_s *Am^2/kg* (Saturating Field *kA/m*)	BH_{max} *kJ/m^3*	T_{curie} *K*
Cui *et al.* 2013 [20]	$Mn_{56}Ga_{44}$	$L1_0$	HEBM for 6 h in Ar then 873 K anneal for 20 min	493	42	61	20	629
Gong *et al.* 2015 [22]	$Mn_{65}Ga_{35}$	$L1_0$	Melt-spun ribbon then 723 K anneal for 1 h and ice water quench	215		61.3 (3979)	16.7	705
Mix *et al.* 2015 [15]	$Mn_{55}Ga_{45}$	$L1_0$	1 h vibration-milled into powder and 623 K anneal and quench	173		84.9 (3979)		
"	$Mn_{60}Ga_{40}$	$L1_0$	1 h vibration-milled into powder and 623 K anneal and quench	299		67.8 (3979) *		
Gong *et al.* 2015 [22]	$Mn_{75}Ga_{25}$	$D0_{22}$	Melt-spun ribbon then 723 K anneal for 1 h and ice water quench	549		18.2 (3979)		>700
Huh *et al.* 2013 [17]	$Mn_{75}Ga_{25}$	$D0_{22}$	Melt-spun ribbon then 723 K anneal for 50 h under vacuum	517		28.0 *		>799
"	$Mn_{72}Ga_{28}$	$D0_{22}$	"	318		34.45 *		>796
"	$Mn_{68}Ga_{32}$	$D0_{22}$	"	279		37.74 *		>735
"	$Mn_{66}Ga_{34}$	$D0_{22}$	"	199		41.78 *		>702
Liu *et al.* 2015 [24]	$Mn_{70}Ga_{30}$	$D0_{22}$	Melt-spun ribbon at 50 $m.s^{-1}$ then 873 K anneal for 1 h under vacuum	535	6.15	~9 (1989)		
Niida *et al.* 1996 [6]	$Mn_{70}Ga_{30}$	$D0_{22}$	1173 K anneal for 1 day then water quench followed by filing into powder then 573 K anneal for several days	1074	25	50 (11937)		>770
Saito and Nishimura 2012 [23]	$Mn_{70}Ga_{30}$	$D0_{22}$	Melt-spun ribbon at 50 $m.s^{-1}$ then 973 K anneal for 1 h	454	8.4			>730

Note: Magnetic properties are for room temperature and isotropic unless otherwise noted.
* Moment is converted from emu/cm^3 or kA/m using a density of 7300 kg/m^3 for the $L1_0$ phase and 7180 kg/m^3 for the $D0_{22}$ phase.
~ Indicates a value determined from a graph rather than taken in text.

Niida *et al.* produced particulate $Mn_{70}Ga_{30}$ $D0_{22}$ samples by filing a quenched alloy containing the high temperature γ-Mn phase into a powder and annealing at 573 K for several days [6]. They attempted to produce an anisotropic powder by annealing under a 796 kA/m applied field. However, since the starting phase was the γ-Mn phase, the material had to proceed through the $D0_{19}$ hexagonal structure during the magnetic field-assisted anneal before transforming to the tetragonal $D0_{22}$ phase. They concluded that this non-magnetic intermediate phase prevented the magnet from developing significant anisotropy. Despite this, they observed a complete transformation to single-phase $D0_{22}$ powder with an exceptionally high H_c of 1074 kA/m and M_r of 25 Am^2/kg. This low temperature anneal prevented the $D0_{22}$ phase decomposition seen during higher temperature anneals. They also investigated alloying with a small amount of Fe. However, this showed no significant impact on the magnetic properties.

2.4. Mn-Ga thin film processing

Thin film processing of both the $L1_0$ and $D0_{22}$ phases in the Mn-Ga system has been studied in some depth [19,25-30]. Generally, sputtering is used to deposit the alloy onto a crystalline substrate which is held at temperatures from 573 to 723 K. Then a capping layer is often added to prevent oxidation, and subsequent annealing may be performed. The magnetic properties depend strongly on the anisotropy of the thin film structure (see Table 3). Generally, the direction perpendicular to the thin film provided the best magnetic properties for a hard magnet, due to the alignment of the magnetically easy *c*-axis perpendicular to the film surface. However, this isotropy is dependent on the substrate used. For example, anisotropic $L1_0$ films have been successfully deposited onto both MgO with a Cr buffer layer and Si-GaAs with a GaAs buffer, while the Si/SiO_2 crystalline/amorphous substrate used by Feng *et al.* achieved only partial anisotropy for either $Mn_{60}Ga_{40}$ $L1_0$ or $Mn_{70}Ga_{30}$ $D0_{22}$ thin films. [19,25-27]. Furthermore, Feng *et al.* observed that the magnetic behavior of the thin film deposited onto a Si substrate without an amorphous SiO_2 buffer layer was worse than with the buffer layer. Rode *et al.* compared the impact of MgO and $SrTiO_3$ substrates without a buffer layer, both with (0 0 1) orientations, on the saturation magnetization of $D0_{22}$ thin films [26]. The film grown on MgO had a higher M_s of 30 Am^2/kg, and a higher order parameter, S, of 0.68 than the film grown under the same conditions on $SrTiO_3$ at 22 Am^2/kg and 0.56, respectively. This suggests that the MgO substrate has the better crystal lattice match of the two for improving the isotropic texture of the $D0_{22}$ thin film. Zhu *et al.* [27] demonstrated the ability to tune M_s and H_c of a $Mn_{60}Ga_{40}$ $L1_0$ film by varying the substrate temperature from 373 to 573 K; substrate temperatures above 573 K were shown to produce undesirable secondary phases. A H_c of 3406 kA/m was observed for a substrate temperature of 373 K, which decreased to 859 kA/m at 573 K. They observed that as the substrate temperature was increased, S and M_s both increased (S = ~0.2 and M_s = 4 Am^2/kg at 373 K; S = ~0.4 and 37 Am^2/kg at 573 K), while the broadening of the (0 0 2) MnGa peak (FWHM) in the XRD spectra decreased. The latter suggests that the density of defects in the crystal lattice is decreased by increasing the temperature, which in turn improves the overall magnetization perpendicular to the film. However, this decreases the available defects for pinning of magnetic domain walls and leads to the decrease in H_c.

Table 3
Composition, phase, method, and magnetic properties for selected Mn-Ga thin film magnets.

Reference	Composition	Phase	Processing Technique	H_c *kA/m*	M_r *Am^2/kg*	M_s *Am^2/kg* (Saturating Field *kA/m*)	BH_{max} *kJ/m^3*	T_{curie} *K*
Feng *et al.* 2017 [25]	$Mn_{60}Ga_{40}$	$L1_0$	30 nm thick sputter deposition at 723 K onto (1 0 0)/amorphous Si/SiO_2 and capped with Ta	692 (‖)		48.40 (⊥) *		
Mizukami *et al.* 2012 [19]	$Mn_{54}Ga_{46}$	$L1_0$	30 nm thick sputter deposition at 673 K onto (1 0 0) MgO/Cr buffer and capped with Ta	119 (⊥)		82.19 (⊥) *		
Zhu *et al.* 2012 [27]	$Mn_{60}Ga_{40}$	$L1_0$	48 nm thick molecular-beam epitaxy at 573 K onto (0 0 1) Si-GaAs/GaAs buffer and capped with Al	859 (⊥)	34.84 (⊥) *	37.06 (⊥) *	20.7 (⊥)	
Feng *et al.* 2017 [25]	$Mn_{70}Ga_{30}$	$D0_{22}$	30 nm thick sputter deposition at 723 K onto (1 0 0)/amorphous Si/SiO_2 and capped with Ta	947 (‖)		44.11 (⊥) *		
Mizukami *et al.* 2012 [19]	$Mn_{75}Ga_{25}$	$D0_{22}$	30 nm thick sputter deposition at 673 K onto (1 0 0) MgO/Cr buffer and capped with Ta	1154 (⊥)		27.86 (⊥) *		
Rode *et al.* 2013 [26]	$Mn_{75}Ga_{25}$	$D0_{22}$	60 nm thick sputter deposition at 623 K onto (0 0 1) $SrTiO_3$ or MgO and capped with MgO	955 (⊥)		21.59 ($SrTiO_3$) 30.22 (MgO) (⊥) *		
"	$Mn_{67}Ga_{33}$	$D0_{22}$	"			59.89 ($SrTiO_3$) 61.28 (MgO) (⊥) *		

Note: Magnetic properties are at room temperature and isotropic unless otherwise noted.
* Moment is converted from emu/cm^3 or kA/m using a density of 7300 kg/m^3 for the $L1_0$ phase and 7180 kg/m^3 for the $D0_{22}$ phase.
(⊥) Indicates measurement perpendicular to thin film surface, or out-of-plane.
(‖) Indicates measurement parallel to thin film surface, or in-plane.
~ Indicates a value determined from a graph rather than taken in text.

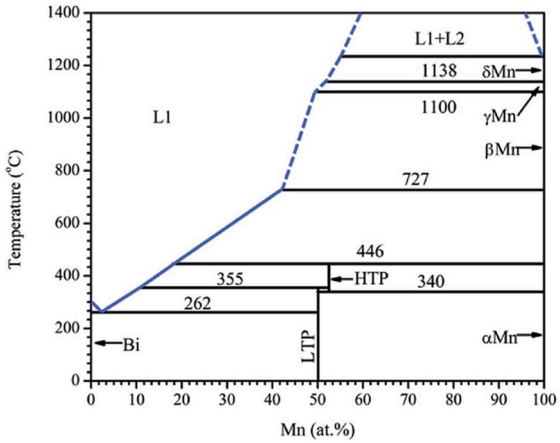

Fig. 6. The binary phase diagram of the Mn-Bi system showing the low-temperature phase (LTP) and high temperature phase (HTP). Both are line phases of slightly different compositions. From [38].

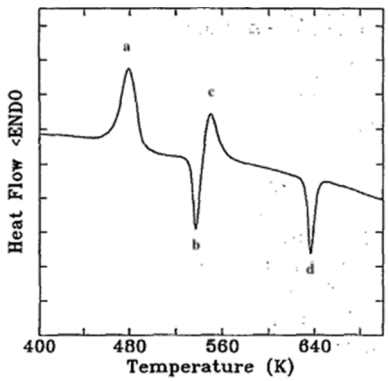

Fig. 7. DSC curve (80 K/min) of the formation of LTP at the second endotherm (c) at 543 K then subsequent transition to HTP at the final endotherm (d) at 640 K as described in [40]. Reprinted from [40] with the permission of AIP publishing.

3. Manganese-Bismuth based magnetic materials

3.1. Mn-Bi crystal structure and phase equilibria

Two ferromagnetic phases in the Mn-Bi system have been the focus of research: the ferromagnetic hexagonal $B8_1$ NiAs structure low-temperature phase (LTP) (see Fig. 5(a)), and a metastable orthorhombic ferromagnetic quenched high-temperature phase (QHTP) (see Fig. 5(b)). The LTP has received more interest in energy applications due to its stability at higher temperatures. QHTP transforms rapidly into LTP at roughly 440 K, whereas LTP remains stable up to its transformation into the high temperature phase (HTP) around 628 K. The QHTP has been researched for its potential in magneto-optical and data storage applications [31]. The $Mn_{52}Bi_{48}$ HTP phase has a $B8_2$ structure, with the excess Mn sitting on the (1/3, 2/3, 3/4) lattice site: the unit cell is distorted from hexagonal symmetry to orthorhombic upon quenching into the QHTP phase, see Fig. 5(b) [32]. Mn-Bi stands apart from Mn-Ga and Mn-Al in that the LTP has a positive temperature coefficient for H_c, i.e. H_c increases upon heating. Chen *et al.* conducted an in-depth analysis of the formation of single-crystal LTP and QHTP phases [33]. They observed that the hexagonal LTP structure had lattice parameters of $a = b = 0.429$ nm and $c = 0.6126$ nm and formed from equi-atomic MnBi as shown in the phase diagram, see Fig. 6.

The magneto-crystalline anisotropy energy of the LTP has been found to be 1.3 MJ/m^3 at 300 K, which was found to increase to 2.2 MJ/m^3 at 490 K [33]. Each Mn atom in the unit cell possessed a magnetic moment of 3.84 μ_B at 4 K. Subsequent research and modeling has shown a theoretical magnetic moment of ~3.6 μ_B per Mn atom and magneto-crystalline anisotropy constant of ~1.5 MJ/m^3 at room temperature [34-36]. Comparing this to the QHTP phase, which forms at $Mn_{52}Bi_{48}$, as shown in Fig. 5, Chen observed a magnetic moment of 3.07 μ_B per atom at 4 K as well as a magneto-crystalline anisotropy energy of 3 MJ/m^3 at 300 K [37]. This value decreased with increasing temperature, i.e. an opposite trend to the behavior of the LTP, which increased. The theoretical $(\mathbf{BH})_{max}$ for LTP at 300 K is ~141 kJ/m^3 at a density of 8900 kg/m^3 and a predicted M_s of 79 Am^2/kg [34,35].

One difficulty with forming the LTP is that it forms via a peritectic reaction between the HTP phase and the Bi-rich liquid, see Fig. 5 [37]. DSC and XRD analyses by Guo *et al.,* shown in Fig. 7, demonstrate the formation of the LTP from amorphous $Mn_{51}Bi_{49}$ melt-spun

Table 4
Composition, phase, method, and magnetic properties for selected LTP Mn-Bi bulk magnets.

Reference	Composition	Processing Technique	H_c *kA/m*	M_r *Am^2/kg*	M_s *Am^2/kg* (Saturating Field *kA/m*)	BH_{max} *kJ/m^3*	T_{curie} *K*
Cao *et al.* 2018 [47]	$Mn_{60}Bi_{40}$	Melt-spun ribbons at 35 m.s^{-1} in Ar, 673 K anneal for 30 min in vacuum, ball milled for 30 min, then spark-plasma-sintered at 593 K under 50 MPa for 5 min	566	26		12.2	
Chen *et al.* 2015 [41]	$Mn_{45}Bi_{55}$	Anneal at 573 K for 24 h under vac then crushed and ball-milled for 7 h. Sintered into bulk at 593 K, 50 K/min, for 5 min under 90 MPa into 1.5 mm thick and 10 mm diameter disk	294 (2308 at 600 K)	34	64 (4775)	29.4	
Gabay *et al.* [42]	$Mn_{50}Bi_{46.5}Mg_3Sb_{0.5}$	Melt-spun ribbons at 15 m.s^{-1} in Ar, then hot-compacted under 340 MPa at 423 K for 1 h. Magnetic field annealed under 2387 kA/m field at >573 K for 10 min	342 (‖)	0.7 T (B_r) (‖)		92 (‖)	
Kim *et al.* 2017 [52]	$Mn_{55}Bi_{45}$	Melt-spun at 55 m.s^{-1} under Ar. Then crushed and compressed under 40 MPa into 10 mm diameter cylinder. Then 573 K anneal for 20 h in vac, magnetically separated, 1 h ball milling, compacted under 650 MPa and in 1592 kA/m, sintered at 553 K for 15 min under 350 MPa and vac	446	53.7		58.1	
"		" But 2 h ball milling	533	50.3		55	
"		" But 2.5 h ball milling	581	49.2		52	
"		" But Jet milled at 0.34 MPa under N_2	684	47.1		49	
Mitsui *et al.* 2018 [49]	$Mn_{50}Bi_{50}$	Powder pressed at 20 MPa and sintered into a pellet at 523 K for 3 h	~1.95 (‖)		~1.5 (955) (‖)		
"		" But sintered for 48 h	~0.56 (‖)		~18 (955) (‖)		
"		Powder pressed at 20 MPa and sintered into a pellet at 523 K for 3 h under 11.9 MA/m	~0.56 (‖)		~12 (955) (‖)		
"		" But sintered for 48 h under 11.9 MA/m	~0.02 (‖)		~40 (955) (‖)		
Nguyen and Nguyen 2018 [46]	$Mn_{50}Bi_{50}$	Powder compacted under 12.4 MPa and 1432 kA/m then sintered at 573 K for 30 min under Ar	~240		~70 (1035)	67	
Poudyal *et al.* 2016 [44]	$Mn_{50}Bi_{50}$	528 K anneal for 8 h then 625 K anneal for 5 h and furnace cool. Crushed, ground, and sieved then annealed at 563 K for 24 h under vac. Then ball milled in liq. N_2 for 15 min. Then aligned under 1592 kA/m and warm compacted under 200 MPa at 518 K for 30 min	493 (1289 at 400 K) (‖) and 318 (⊥)	0.6 T (B_r) (‖) and 0.19 T (B_r) (⊥)	64 (7162) And 56 at 400 K (7162) *	67 (62 at 350 K and 54 at 400 K)	
Qian *et al.* 2019 [50]	$Mn_{50}Bi_{50}$	Mn and Bi powder mixed together in shaker for 1 h. Then compacted under 110 MPa and sintered at 538 K for 3 h and at 623 K for 72 h. Then crushed and LEBM for 4 h and vacuum sintered at 593 K under 450 MPa	499.1	24	49 (3183)		
"	$(Mn_{50}Bi_{50})_{95}C_5$	" But after LEBM mixed with HEBM C powder and vacuum sintered at 593 K under 450 MPa	561.3	21	41 (3183)		
"	$(Mn_{50}Bi_{50})_{95}(NaCl)_5$	" But after LEBM mixed with HEBM NaCl powder and vacuum sintered at 593 K under 450 MPa	719.5	17	33 (3183)		
Si *et al.* 2019 [43]	$Mn_{55}Bi_{45}$	Mn nano-powder mixed with Bi powder then vac sealed anneal at 606 K for 8 days. Then pressed into 2 mm diameter pellet under 3 GPa and sintered at 546 K for 90 min under 4 MA/m	135	37	47 (3979)		
Zhang *et al.* 2011 [45]	$Mn_{48}Bi_{52}$	Anneal at 573 K for 10 h then crushed and high-energy ball-milled for 4 h. Sintered into bulk at 593 K, 50 K/min, for 5 min under 90 MPa into 1.5 mm thick and 10 mm diameter disk	627	30			

Note: Magnetic properties are at room temperature and isotropic unless otherwise noted.
* Moment is converted from emu/cm^3 or kA/m using a density of 8900 kg/m^3 for LTP.
(⊥) Indicates measurement perpendicular to direction of magnetic alignment during annealing or bonding.
(||) Indicates measurement parallel to direction of magnetic alignment during annealing or bonding.
~ Indicates a value determined from a graph rather than taken in text.

ribbons. The first DSC exotherm (a) is the crystallization of non-magnetic Bi-rich and Mn-rich phases. The first endotherm (b) is the melting of the Bi-rich phase, followed by the formation of LTP at the second exotherm (c) at ~543 K. The last endotherm (d) corresponds to the LTP to HTP transition at ~640 K. Cooling from the LTP formation to room temperature retains a high percentage of LTP but some peritectic decomposition commonly occurs. The metastable QHTP by contrast requires a rapid cooling rate to remain at room temperature after heating [39].

3.2. Mn-Bi bulk processing

LTP MnBi is stable at room temperature but only at the equi-atomic composition. Therefore, a key factor in bulk processing of LTP is mitigating variations in composition of the alloy that could produce a significant percentage of non-magnetic phases. Various methods have been tried to produce high phase-fraction LTP, such as melt-spinning, arc-discharge melting, or more conventional arc-casting combined with annealing and milling at room or cryogenic temperatures in a powder state [41-44]. However, unlike Mn-Ga and Mn-Al (see later), which can form over a range of compositions, the equi-atomic composition of a bulk MnBi magnet is difficult to maintain. For this reason, bulk MnBi is generally consolidated from a high phase-fraction powder LTP precursor formed by the aforementioned methods. The processing of these powders is presented in the subsequent section.

Multiple techniques have been explored for transforming a powder LTP precursor into a bulk magnet [41,45]. Poudyal *et al.* transformed a high phase-fraction LTP precursor to a bulk magnet using a low-temperature sintering approach [44]. They created anisotropic alignment of the 7 μm or greater diameter, 96 wt.% LTP powder by applying a magnetic field of 1592 kA/m and then compacting it in a mold at 518 K at a uniaxial compressive stress of 200 MPa for 30 min under flowing Ar. They observed that at higher pressures than 200 MPa the grain size increased beyond 50 nm and the anisotropy of the bulk magnet was deteriorated. This method produced a sintered bulk magnet with density of nearly 8700 kg/m^3 and a $(\mathbf{BH})_{max}$ of 67 kJ/m^3. In a similar experiment, Nguyen and Nguyen produced a bulk sintered magnet of equal maximum energy product but lower density of 8400 kg/m^3 [46]. Starting with a 94 wt.% LTP precursor, the powder was anisotropically aligned under a 1432 kA/m magnetic field then sintered under an applied pressure of 12.4 MPa, oriented perpendicularly to the applied field, at 573 K for 30 min. The lower applied pressure explains the lower density achieved by this process. Additionally, the M_s value reported for this method is slightly greater than that reported by Poudyal *et al.* but H_c is far less (see Table 4). Unfortunately, not enough data is reported on the magnetic and microstructural characteristics of the precursor powders or the bulk magnets to draw definitive conclusions as to why the two methods produced magnets with the same $(\mathbf{BH})_{max}$ but with differing M_s and H_c.

Spark plasma sintering (SPS) has the advantage over conventional sintering of a very high heating rate and short dwell time at the sintering temperature. This has been suggested as a way to prevent the peritectic LTP decomposition, maintain a fine-grained and homogenous microstructure, and improve the stability of the magnet at elevated temperatures [41,47,45]. Chen *et al.* performed SPS to consolidate a ball-milled $Mn_{45}Bi_{55}$ powder (0.5–5 μm in diameter) of ~61 wt.% LTP [41]. After sintering at 593 K, at a rate of 50 K/min, for 5 min under a uniaxial pressure of 90 MPa in a graphite die, they observed that the LTP fraction of the resulting bulk magnet increased to ~80 wt.%. This suggests that in this case SPS formed additional LTP rather than causing decomposition of that phase. They also observed that the grain size was unchanged when compared to the powder precursor, implying that the SPS technique did not cause coarsening of the grains. Having excess Bi in the binary alloy may also improve the stability of the LTP due to the fact that by this method the LTP grains tended to be surrounded by single-phase Bi regions. Their magnetic measurements showed that at temperatures as high as 650 K, which should be above the decomposition temperature, the magnet formed by SPS demonstrated decreased but still significant hard-magnetic behavior with a M_s of ~60% of the room-temperature M_s. They noted that previous studies have shown that composite MnBi in single-phase Bi under an applied magnetic field has a higher LTP decomposition temperature than binary MnBi by as much as 20 K under a 8 MA/m applied field [48], and that this microstructure of fine MnBi regions surrounded by Bi is likely the cause of the improved thermal stability.

Cao *et al.* performed SPS at the same temperature, 593 K, and time, 5 min, as Chen *et al.* but under a lower pressure of 50 MPa and with a different composition powder $Mn_{60}Bi_{40}$ precursor with ~71 wt.% LTP present [47]. A comparison of the $M_{5MA/m}$ values between the two studies demonstrates that the phase fraction of LTP in this $Mn_{60}Bi_{40}$ bulk magnet is less than that of the previously described $Mn_{45}Bi_{55}$ magnet despite having a precursor of higher percentage LTP. This corroborates the theory that the excess Bi stabilizes the LTP from decomposing during the SPS process and demonstrates that the SPS technique on its own does not promote increased formation of LTP in the case of the $Mn_{60}Bi_{40}$ alloy. The decrease in LTP may be also in part due to the formation of a significant MnO phase in the $Mn_{60}Bi_{40}$ magnet that was not observed in the $Mn_{45}Bi_{55}$ magnet. The abundance of Mn in the $Mn_{60}Bi_{40}$ magnet, combined with the absence of reporting by Cao *et al.* that the precursor milling and SPS were performed in an atmosphere other than air, suggests that a lack of atmospheric control during SPS can cause excess MnO formation at the expense of LTP. Zhang *et al.* observed this phenomenon by comparing the $M_{1.8MA/m}$ of two Mn-Bi magnets prepared by identical SPS methods at two different compositions [45]. They observed that M_s increased from 27.87 Am^2/kg to 45.31 Am^2/kg when the Bi concentration was increased from 40 at.% to 52 at.%, further demonstrating that the increased Bi concentration promotes the formation of magnetic LTP, and excess Mn promotes the formation of non-magnetic phases.

Solid-state reactive sintering is another method by which Mn-Bi bulk magnets have been formed from a powder precursor. However, rather than the precursor being the homogeneous powdered LTP Mn-Bi alloy, the reactive sintering method uses high-purity Mn and Bi powders as the precursor and forms the Mn-Bi alloy during the sintering process [43,49]. Yet, combining the steps of forming LTP and sintering into a bulk shape poses a challenge for forming high volume fraction LTP bulk magnets. As noted earlier, LTP decomposes at temperatures above 628 K, i.e. sintering temperature has to occur below 628 K. According to Mitsui *et al.,* the reactive sintering process is diffusion controlled and therefore is observed to follow an Arrhenius reaction relationship where the diffusion coefficient and atomic jump frequency increase exponentially with increasing temperature [49]. In their experiment they used reactive sintering to form $Mn_{50}Bi_{50}$ LTP from Mn and Bi micro-powder precursors. They observed that the reacted LTP fraction and the M_s increased with sintering time as shown in Fig. 7, but after 48 h only ~50 wt.% LTP had formed. In addition, H_c for the magnet decreased with annealing time, likely due to the coarsening of the average grain size, making it difficult to form a permanent magnet with both high M_s and high H_c. In similar work, Si *et al.* used the reactive sintering approach with Mn nanoparticles and Bi powder as the precursors [43]. While they achieved a much higher LTP fraction of ~64 wt.%, the experiment once again demonstrated that the higher LTP phase fraction came with a decrease in H_c. For two equi-atomic MnBi samples sintered under an applied field of 3979 kA/m, one at 546 K for 90 min and the other at 583 K for 90 min, the higher temperature sample had higher M_s but a lower H_c; for an increase in M_s from 47 to 51 Am^2/kg, the H_c decreased from 135 to 96 kA/m. It was observed in both of these studies that the addition of the magnetic field during sintering improved the fraction of LTP and produced anisotropy in the grain orientations. It was suggested that the application of the magnetic field decreased the activation energy barrier for the reaction between Mn and Bi and that the magnetic field preferentially assisted the growth and coarsening of nuclei oriented with the *c*-axis parallel to the applied field. Therefore, in comparison to the melt-spinning methods of forming Mn-Bi alloys, the reactive sintering process requires a much longer time to form a high volume-fraction of LTP. Furthermore, this method does not permit improved control of the microstructure when compared to the conventional sintering techniques discussed earlier.

The addition of alloying elements to Mn-Bi has been researched as a method to improve bulk magnetic performance. The alloyants NaCl and C were explored by Qian *et al.* [50] as a means of increasing H_c. Milled $Mn_{50}Bi_{50}$ micro-powder was mixed with either NaCl or C nano-powder at 2 or 5 wt.%. The powders were compacted into a bulk magnet under a uniaxial pressure of 450 MPa at 593 K under vacuum. They suggested that by this method the NaCl and C nano-powders were concentrated at the small gaps between the MnBi micro-powder particulates and, upon hot compaction, remained concentrated in the MnBi grain boundary region. This could suggest that the NaCl and C impurities serve as pinning sites for the MnBi magnetic domain walls near the edges of grains, thus explaining the increase in observed H_c. However, these regions of impurities decrease the overall density and may also magnetically insulate the magnetic domains from one another, explaining a decrease in M_s in alloyed samples compared to unalloyed MnBi bulk prepared by the same method. ($M_s = 49$ Am^2/kg for unalloyed, 41 Am^2/kg for 5 wt.% C, and 33 Am^2/kg for 5 wt.% NaCl). Co-alloying with Mg and Sb in place of Bi by Gabay *et al.* to form $Mn_{50}Bi_{46.5}Mg_3Sb_{0.5}$ produced the highest reported $(\mathbf{BH})_{max}$ for bulk Mn-Bi of 92 kJ/m^3 [42]. Starting with melt-spun ribbons of 44.5 wt.% QHTP, they transformed the material into 51 wt.% LTP using hot compaction under a uniaxial pressure 340 MPa at 423 K for 1 h. To complete the transformation to 98 wt.% LTP and develop strong anisotropy in the bulk, they performed pulsed magnetic field annealing at <573 K under a 2387 kA/m applied field for 10 min. The addition of either Mg or Sb was shown to lower the LTP phase formation temperature as well as decreasing the melting point of the Bi phase. They concluded that the presence of a liquid phase during magnetic annealing encouraged alignment of the LTP grains and improved texture. Co-alloying with Mg and Sb also lowered the HTP formation temperature and raised the decomposition temperature of the HTP, thereby greatly improving the thermal stability of this phase during annealing.

3.3. Mn-Bi particulate processing

Saito *et al.* investigated a straightforward method for producing LTP ribbons through melt-spinning followed by annealing [51]. Cast ingots of Mn_xBi_{100-x} ($x = 60$–40 at.%) were induction melted then ejected using argon onto a copper wheel rotating at 50 $m.s^{-1}$. The rapid quench prevented the peritectic decomposition and produced the LTP. However, XRD analysis of the as-spun ribbons revealed a significant Bi phase fraction had formed despite the rapid cooling rate. Additionally, by increasing the relative Mn concentration in the alloy, the Bi diffraction peaks became stronger and some α-Mn phase was also observed in alloys containing 50–60 at.% Mn. To increase the fraction of the LTP in the ribbons they performed a 1 h anneal under an argon atmosphere at various temperatures. M_r was observed to increase with increasing annealing temperature from 373 K to 673 K. They observed an optimum combination of M_r and H_c for equiatomic MnBi annealed for 1 h at 673 K. This suggests that this temperature and time caused the Bi phase regions to preferentially melt, due to its lower melting point, and nucleate as LTP while maintaining the existing fraction of LTP. At 773 K M_r significantly diminished, suggesting that such a high temperature actually decomposes the LTP.

Kim *et al.* employed both melt-spinning as well as magnetic separation to improve the volume fraction of the LTP [52]. This technique uses a magnetic field to separate the powdered LTP fraction from any undesired non-magnetic phases present. It was previously reported by Yang *et al.* that an LTP fraction of approximately 60 wt.% was possible by conventional sintering, which could be enhanced to 90 wt.% LTP by subsequent magnetic separation [53]. The combination of melt-spinning and magnetic separation employed by Kim *et al.* demonstrated the benefit of rapid quenching on preserving a high LTP fraction. By melt spinning they produced $Mn_{55}Bi_{45}$ ribbons with 95 wt.% LTP fraction. The magnetic separation technique then improved the LTP fraction to 98 wt.%.

One key property of MnBi in powdered form is its high affinity for oxidation in air. The room temperature change in Gibbs free energy for the oxidation of MnBi is −653 kJ/mol, making it significantly more likely to oxidize than another easily oxidized material, Cu, which has a Gibbs free energy change of oxidation of −544 kJ/mol [37]. Therefore, controlling the atmosphere in which particulate processing is carried out on MnBi is critical to preventing oxidation. Generally, the milling process is used to improve the H_c of

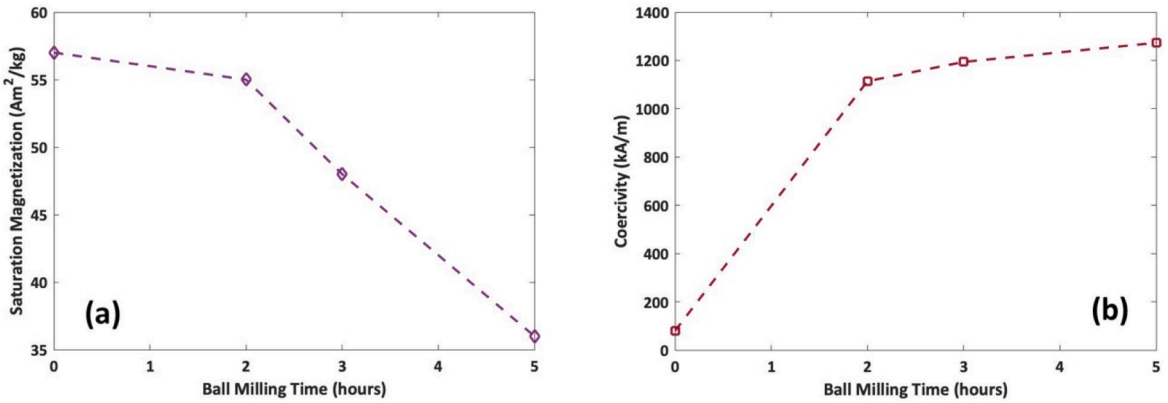

Fig. 8. The effect of ball milling on $Mn_{50}Bi_{50}$ LTP powder. Increasing ball milling time decomposes the LTP, reducing M_s shown in (a) but improving H_c shown in (b). Redrawn with permission from [55].

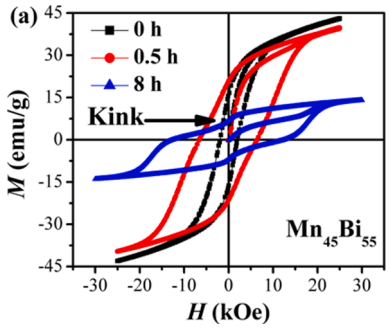

Fig. 9. VSM hysteresis curve for $Mn_{45}Bi_{55}$ powder after 0 (unmilled), 0.5, and 8 h of milling. Note the kink in the 8 h VSM curve showing non-uniform domain reversal behavior. From [56].

the material by introducing crystal defects. However, this can decompose the LTP, so a balance must be struck between milling and preserving the LTP.

The simplest preparation of particulates is to manually crush and grind a bulk sample then sieve the resulting powder to control the particulate size. This technique was used by Cui *et al.* on an as-cast $Mn_{55}Bi_{45}$ ingot containing ~82 wt.% LTP ($M_{1.8MA/m} = 56$ Am^2/kg), forming particulates that they sieved to obtain particles of ~37–44 μm [37]. They then subjected the particulates to a heat treatment under vacuum of 563 K for 24 h. The LTP fraction was improved to 93 wt.% through this vacuum heating process, and correspondingly they observed the M_s increased to $M_{1.8MA/m} = 63$ Am^2/kg ($M_{6.4MA/m} = 74$ Am^2/kg, i.e. ~93% of the theoretical maximum of 79 Am^2/kg). However, annealing milled powder does not necessarily recover LTP lost during milling. Zhang *et al.* observed that high-energy ball milling of melt-spun and annealed $Mn_{55}Bi_{45}$ ribbons for 4 h was the optimal time for maximizing H_c for the material, at the expense of both M_s and M_r [54]. They performed a subsequent vacuum anneal at 673 K for 30 min. XRD analysis showed an increase in LTP peak intensity but also evidence of grain coarsening and an increased fraction of MnO present. Consequently, magnetic measurements showed that post-milling annealing actually decreased both M_s and H_c in this case. Li *et al.* observed the same tradeoff of magnetization for H_c in the case of low-energy ball milling [55]. Beginning with an 89 wt.% LTP $Mn_{50}Bi_{50}$ bulk precursor, they performed low-energy ball milling for 2–5 h at a 10:1 ball to powder ratio. H_c showed a significant increase after 2 h of milling but with diminishing returns at longer milling times, as shown in Fig. 8(b). Similarly, the LTP fraction and M_s decreased slightly at 2 h then dramatically decreased at longer milling times. This demonstrates that by decreasing the particle size and imparting mechanical defects into the crystal structure H_c can be increased through milling for a longer duration, but M_s and the LTP fraction will also be diminished by such a procedure. It has also been proposed that as the LTP decomposes into Mn, Bi, and MnO phases, all of which are only weakly magnetic, the LTP regions become magnetically isolated from one another, further enhancing H_c but diminishing M_s [56].

One technique to prevent the decomposition of LTP during milling is to lower the processing temperature to cryogenic levels, performing what is termed "cryo-milling" [44,57]. Poudyal *et al.* performed cryo-milling on 98 wt.% LTP $Mn_{50}Bi_{50}$ by low-energy ball milling (LEBM) in liquid nitrogen [44]. This technique demonstrated that even after 150 min of LEBM they had retained 96 wt.% LTP, but at longer durations the LTP was observed to further decompose just as in room temperature LEBM. Xie *et al.* directly compared room temperature and cryogenic LEBM in liquid nitrogen [57]. After 8 h of LEBM, M_s of the room temperature milled powder was 63.2 Am^2/kg compared to 65.4 Am^2/kg for the cryo-milled powder. The same trend was also observed for 24 h of LEBM: the M_s of the room temperature powder was 47.8 Am^2/kg and 55.5 Am^2/kg for the cryo-milled powder. They also obtained the highest M_s of 71 Am^2/kg

Table 5
Composition, method, and magnetic properties for selected LTP Mn-Bi particulate magnets.

Reference	Composition	Processing Technique	H_c *kA/m*	M_r *Am^2/kg*	M_s *Am^2/kg* (Saturating Field *kA/m*)	BH_{max} *kJ/m^3*	T_{curie} *K*
Cao *et al.* 2019 [56]	$Mn_{60}Bi_{40}$	Melt-spun at 35 m.s^{-1} under Ar then 673 K anneal for 30 min under vac. SABM for 0.5 h	467.12	35.3			
"		Bonded in epoxy resin at 300 K under 1432 kA/m	1105.33 (‖)	54.7 (‖)		72.1 (‖)	
"		Bonded in epoxy resin at 380 K under 1432 kA/m	1461.04 (‖)			56.1 (‖)	
"	$Mn_{55}Bi_{45}$	Same powder process as $Mn_{60}Bi_{40.}$ Bonded in epoxy resin at 300 K under 1432 kA/m	954.93 (‖)				
"		Bonded in epoxy resin at 380 K under 1432 kA/m	1374 (‖)				
Cui *et al.* 2014 [37]	$Mn_{55}Bi_{45}$	528 K anneal for 8 h then 625 K anneal for 5 h and furnace cool. Crushed, ground, and sieved then annealed at 563 K for 24 h under vac	< 239	~40	74 (7162)		
Gabay *et al.* 2019 [32]	$Mn_{55}Bi_{43.5}Sb_{1.5}$	Melt spun ribbons then 30 min anneal at 573 K. Ribbons were crushed to 0.1 mm and bonded in paraffin wax under 1273 kA/m	716 (‖)	32.9			
Guo *et al.* 1991 [40]	$Mn_{51}Bi_{49}$	Melt-spun ribbons at 50 m.s^{-1} under Ar	55 (853 at 455 K)			11.3 (at 455 K)	> 630
"	$Mn_{51}Bi_{49}$ (QHTP)	LTP ribbons wrapped in Al foil annealed at >630 K then quenched in water	184			4.4	450
Kanari *et al.* 2017 [60]	$Mn_{50}Bi_{50}$	563 K anneal for 24 h under vac then crushed into powder	111 (135 after 2 months in air)		61 (41.1 after 2 months in air)		
"		Additional low-energy SABM for 35 min	907		< 33		
Li *et al.* 2018 [55]	$Mn_{50}Bi_{50}$	573 K anneal for 25 h then crushed and sieved, ball mill for 2 h, then bonded in epoxy under 1432 kA/m	1117.0		55.1 (2387)		
"		" But 3 h ball milling	1196.9		48.27 (2387)		
"		" But 5 h ball milling	1276.7		35.59 (2387)		
Nguyen and Nguyen 2018 [46]	$Mn_{50}Bi_{50}$	573 K anneal for 8 h under Ar then ball milled in liq. N_2 for 15 min into powder	350		48 (1035)		
Rama Rao *et al.* 2014 [197]	$Mn_{50}Bi_{50}$	High energy ball milling for 4 h under Ar then one anneal at 1075 K and quench then 575 K for 15 h then aligned under pulsed 6366 kA/m	1297		22 (2387)		
Rama Rao *et al.* 2015 [64]	$Mn_{50}Bi_{50}$	573 K anneal for 24 h then crushed into powder	91.5		64 (2387)		
"		" Then jet milled at 0.28 MPa	1424		47 (2387)		
"		" But jet milled at 0.55 MPa	1432		41 (2387)		
Saito *et al.* 2014 [51]	$Mn_{50}Bi_{50}$	Melt-spun ribbons at 50 m.s^{-1} then 1 h anneal at 673 K and magnetized at pulsed 3979 kA/m	294 (979 at 473 K and 852 at 573 K)	42			
Si *et al.* 2019 [43]	$Mn_{55}Bi_{45}$	Arc discharge then 12 h passivation. Vac sealed anneal at 606 K for 8 days	637	44.5	54.9 (3979)		
Xie *et al.* 2016 [57]	$Mn_{55}Bi_{45}$	Anneal to form LTP in H_2 , crushed and sieved, 563 K anneal for 48 h, then 8 h ball milling			63.2 (65.4 cryo-milled) (1830)		
"		" But replaced by 24 h ball milling			47.8 (55.5 cryo-milled) (1830)		
"		" Additional 563 K anneal for 24 h then another 30 min ball milling			71.2 (1830)		
Zhang *et al.* 2012 [54]	$Mn_{48}Bi_{52}$	653 K anneal for 7 h then melt spun at 45 m.s^{-1} in Ar. Then 673 anneal for 30 min in vac and ball milled for 4 h	905.6	33.57	49.98 (1751)		
"	$Mn_{55}Bi_{45}$	"	1180	~13	~22.5 (1751)		

Note: Magnetic properties are at room temperature and isotropic unless otherwise noted.
(⊥) Indicates measurement perpendicular to thin film surface, or out-of-plane.
(‖) Indicates measurement parallel to thin film surface, or in-plane.
~ Indicates a value determined from a graph rather than taken in text.

by annealing the 8 h cryo-milled powder for 48 h at 563 K followed by 30 min of additional cryo-milling.

Another modification of the conventional milling technique is to perform surfactant-assisted ball milling (SABM) wherein a surfactant and solvent is used to help decrease the average particle size by keeping the particles dispersed from one another and preventing agglomeration [58]. By carefully evaporating the solvent, the particles can also be more easily removed from solution. Cao *et al.* used surfactants oleylamine and oleic acid as well as the solvent heptane to perform SABM on $Mn_{55}Bi_{45}$ melt-spun ribbons with

milling times from 0.5 to 25 h [56]. They found that SABM H_c increased with milling time, to a maximum after 10 h then decreased for longer times, and that LTP and M_s decreased with increasing milling time similar to the aforementioned trend for ball milling in general. However, they observed strong evidence for inhomogeneous demagnetization behavior in the form of kinks in the VSM curve (see Fig. 9). They tested the thermally-activated strong-pinning model proposed by Gaunt by examining the relationship between intrinsic H_c and temperature, T, given as [59]

$$H_c^{1/2} = H_0^{1/2} - H_0^{\frac{1}{2}} * \left(\frac{75k_B}{4bf}\right)^{\frac{2}{3}} * T^{2/3}$$

where H_0 is the critical field to free a domain wall area from its pin at zero thermal activation energy, k_B is Boltzmann's constant, 4b is the range of domain wall pin interaction, and f is the maximum restoring force of each pin. They observed a linear relationship between $H_c^{1/2}$ and $T^{2/3}$ in the range of 300–380 K for both $Mn_{55}Bi_{45}$ and $Mn_{60}Bi_{40}$ magnets, thereby demonstrating that the strong pinning model is sufficient to describe the H_c in this narrow temperature range. Kanari *et al.* used SABM on $Mn_{50}Bi_{50}$ with the goal of understanding if this technique could prevent oxidization and corrosion of the particles [60]. They first explored high-energy SABM but observed that this technique resulted in significant decomposition of the LTP despite the benefits of the surfactants. They also observed that the average particle composition changed during milling to become Bi-rich, but they could not explain the exact cause of the loss of Mn. The results of low-energy SABM were more promising. They observed that though during the initial min of milling (10–25 min) agglomerates were still formed, after 35 min the agglomeration had been suppressed, and after 170 min they reached an average particle size <1 μm. Similar to Cao *et al.,* they observed kinks in their VSM curves, suggesting an inhomogeneous demagnetization along with increasing H_c with milling time up to 35 min. This may be evidence of irregularly distributed non-magnetic phases, such as Bi and Mn oxides, magnetically isolating the magnetic LTP domains from one another [61]. For times greater than 35 min H_c and M_s both decreased dramatically. They suggested that this could be a combination of several factors: the decomposition of LTP, the milled particles being smaller than the single domain size of 500 nm, and milling defects on their surfaces serving as sites for the nucleation of reverse domains in greater proportion than those serving as pinning sites within the particles. It is worth noting that they observed that the maximum weight percentage of absorbed surfactant molecules after 35 min was 11.2 wt.%, but after 170 min this decreased to 3.9 wt.%. They also observed that for times greater than 35 min the amount of agglomeration increased, indicating that for excessively long SABM durations the surfactants are no longer likely to be absorbed on the particles' surfaces, diminishing the effectiveness of this technique. They left ground but un-milled LTP precursor powder exposed to ambient air for two months and observed a decrease in M_s as well as an increase in H_c. This is similar to the observation by Ly *et al.* on $Mn_{52.5}Bi_{47.5}$ powder in epoxy that was exposed to air for 80 days [62], who found a significant decrease in M_s after 7 days due to the decomposition of MnBi LTP into Bi and manganese oxide.

Jet milling is another alternative technique to conventional ball milling to form fine particulates [63]. In jet milling, high velocity gas jets accelerate ground bulk material in a round grinding chamber. The force of the particles interacting with one another and with the walls of the chamber reduce the average particle size over time. Rama Rao *et al.* investigated the effect of changing the pressure of the air ejected into the grinding chamber by the jets on the morphology of 81 wt.% LTP $Mn_{50}Bi_{50}$ powder [64]. They observed that increasing the pressure from 0.14 MPa to 0.55 MPa decreased the average particle size from 1.7 μm to 1 μm. They suggested that at low pressures (e.g. 0.28–0.41 MPa) the particle morphology displayed a greater contribution from abrasive grinding than from collision-induced breakage, producing smooth plate-like particles. At higher pressures (e.g. >0.41 MPa) the morphology displayed more contribution from collision-induced breakage, producing jagged sharp flakes. They also observed that the fraction of LTP decreased from 81 wt.% before milling to 59 wt.% at 0.14 MPa and 43 wt.% at 0.55 MPa. The LTP content at 0.14 to 0.28, 0.41, and 0.55 MPa was observed to decrease linearly with increasing pressure. Kim *et al.* performed both LEBM and jet milling on $Mn_{55}Bi_{45}$ [52]. The ball milling was carried out for 1–2.5 h with the jet milling being performed under N_2 at a pressure of 0.34 MPa. As expected, M_r was observed to decrease with increasing LEBM time while H_c was observed to increase, with $M_r = 53.7$ Am^2/kg and $H_c = 446$ kA/m for 1 h while $M_r = 49.2$ Am^2/kg and $H_c = 581$ kA/m at 2.5 h. Jet milling produced the lowest remanent magnetization, 47.1 Am^2/kg, and highest H_c, 684 kA/m. They observed that the highest $(\mathbf{BH})_{max}$ value corresponded to LEBM for 1 h and that increases to H_c did not offset the decreases of M_r for longer milling times. Consequently, jet milling produced the Mn-Bi magnet with the lowest reported $(\mathbf{BH})_{max}$ in this study. This result makes sense considering the significant decomposition of LTP observed by Rama Rao *et al.* at similar jet pressures (see Table 5).

Si *et al.* formed $Mn_{55}Bi_{45}$ nanoparticles by preparing Mn and Bi precursor powders and reactively sintering them under vacuum for 8 days at 606 K [43]. They noted that the Mn precursor nanoparticles had an oxide layer roughly 5 nm thick, and that this oxide layer likely inhibited the sintering of the Mn and Bi particulates together. They also observed the agglomeration of Mn-Bi particulates after sintering, which was attributed to the formation of a small fraction of liquid phase during the process. They were able to separate particulate aggregations by ultrasonic processing, but the resulting particulates had a very rough surface and irregular range of sizes compared to the precursors. From VSM and XRD data, they estimated the resulting LTP content of the Mn-Bi particulates to be roughly 69 wt.% LTP with $H_c = 637$ kA/m and $M_r = 44.5$ Am^2/kg, compared to $H_c = 135$ kA/m and $M_r = 37$ Am^2/kg for the consolidated bulk pellets prepared from these particulates as noted earlier.

Gabay *et al.* investigated melt-spun then subsequently annealed Mn-Bi magnets alloyed with 0–5 at.% Sb [32]. The addition of Sb allowed them to achieve significantly higher coercivities in the bulk magnets without working with a milled powder precursor. They attributed this increase in H_c to the ~200 nm grain size of the LTP phase formed after annealing. They observed that melt spinning the Sb-alloyed material at speeds of 15–65 $m.s^{-1}$ formed a high phase content of a unique "new phase" with a $B8_1$ structure and an average grain size of 30–110 nm, which transformed to LTP upon annealing at 473–573 K. The short 30 min annealing time at 573 K to transform this "new phase" into LTP did not allow much time for crystal coarsening, thus preserving a fine microstructure in the final

Table 6
Composition, method, and magnetic properties for selected LTP Mn-Bi thin film magnets.

Reference	Composition	Processing Technique	H_c *kA/m*	M_r *Am^2/kg*	M_s *Am^2/kg* (Saturating Field *kA/m*)	BH_{max} *kJ/m^3*	T_{curie} *K*
Cespedes *et al.* 2017 [67]	$Mn_{58}Bi_{42}$	60 nm thick sputter deposition alternating Mn and Bi layers on 375 K glass substrate then 575 K anneal for 1 h and capped with Ta	1273 (1767 at 350 K and 2308 at 500 K) (⊥)		~47.8 (3979) * (⊥)	55	
"		" but onto 450 K glass substrate then 575 K anneal for 1 h	318 (716 at 350 K) (⊥)		70.8 (3979) * (⊥)	115	
Qin *et al.* 2019 [68]	$Mn_{54}Bi_{46}$	Electrodeposited thin film onto Cu using an electrolyte and −1.36 V then 653 K anneal for 3 h under vac	115.4 (⊥)				
Zhang *et al.* 2015 [36]	$Mn_{50}Bi_{50}$	100 nm thick *e*-beam evaporation deposition alternating Mn and Bi layers on 398 K glass substrate and capped with Ti. Then 563 K anneal for 1 h and 673 K anneal for 1 h	~1550 (⊥)			130 (⊥)	
"		2.0 μm thick *e*-beam evaporation deposition alternating Mn and Bi layers on 398 K glass substrate and capped with Ti. Then 563 K anneal for 1 h and 673 K anneal for 1 h. Then 540 K anneal for 30 min under 5570 kA/m parallel to surface	~320 (‖)			109 (‖)	

Note: Magnetic properties are at room temperature and isotropic unless otherwise noted.
* Moment is converted from emu/cm^3 or kA/m using a density of 8900 kg/m^3 for LTP.
(⊥) Indicates measurement perpendicular to thin film surface, or out-of-plane.
(‖) Indicates measurement parallel to thin film surface, or in-plane.
~ Indicates a value determined from a graph rather than taken in text.

LTP of the magnet. However, this improved H_c (from ~190 kA/m to 716 kA/m from unalloyed to 1.5 at.% Sb) was accompanied by a lack of texture development in the bulk and reduced M_r (from 45.7 Am^2/kg to 32.9 Am^2/kg from unalloyed to 1.5 at.% Sb). Finally, Wu *et al.* explored substituting some of the Bi in $Mn_{55}Bi_{45}$ with Zr in melt-spun ribbons [65]. They reported that the addition of Zr from 0 to 5 at.% resulted in increased LTP formation in the as-spun ribbons, as determined by XRD analysis, increasing the LTP fraction from ~8% to >21%. As expected, they also saw a correlated increase in the M_s of the as spun ribbons with the increasing concentration of Zr. Notably, however, they also saw that H_c increased with increasing Zr content as well, but this trend did not hold at higher LTP contents. For example, upon annealing the as-spun ribbons at 523 K to increase the LTP content further, they observed that for >1 at.% Zr both M_s and the LTP fraction decreased while H_c increased. SEM observation of the resulting microstructure revealed that the average grain size of the annealed ribbons with 5 at.% Zr was roughly ten times smaller than that of the 0 at.% Zr annealed ribbons, explaining the increase in H_c. However, they also observed the formation of a Mn_2Zr phase accompanying the decrease in LTP, which resulted in a decrease in M_s with increasing Zr concentration above 1 at.%.

3.4. Mn-Bi thin film processing

The thin film processing technique is most desirable for intricate small-scale applications such as spin electronics or memory storage because it is possible to produce magnetic anisotropy relatively uniformly across the Mn-Bi film. In 1970, Chen observed that by producing alternating layers of Bi then Mn through vacuum deposition, the *c*-axis of the $B8_1$ structure developed preferentially perpendicular to the thin film surface on substrates of glass, quartz, rocksalt, and Teflon, while the *a*-axis was oriented randomly in the thin film plane [66]. More recently, Zhang *et al.* performed electron beam deposition of alternating Bi and Mn layers onto a glass substrate at 398 K and then capped this with a layer of Ti [36]. This 100 nm thin film, which was annealed for 1 h at 563 K and then 1 h at 673 K, had the *c*-axis perpendicular to the thin film surface, in accordance with Chen's observations. They also prepared a 2 μm thick film that showed randomly-orientated *c*-axes. They were able to align the *c*-axis parallel to an applied magnetic field during subsequent annealing for 30 min at 540 K. Due to the highly anisotropic nature of these thin films, they achieved a $(\mathbf{BH})_{max}$ of 130 kJ/m^3 for the 100 nm thin film, and a $(\mathbf{BH})_{max}$ of 24 and 109 kJ/m^3 for the 2 μm thick magnetically aligned thin films, respectively. Cespedes *et al.* used DC magnetron sputtering of alternating Bi and Mn layers on a glass substrate held at 375–450 K to form 60 nm thick $Mn_{58}Bi_{42}$ thin films [67]. They were subsequently annealed at 575 K for 1 h and capped with Ta to prevent oxidation. The sample sputtered onto the 450 K substrate had a $(\mathbf{BH})_{max}$ of 115 kJ/m^3 compared to 55 kJ/m^3 for the 375 K substrate, i.e. roughly double this value (see Table 6). The 450 K substrate sample displayed a much stronger *c*-axis alignment perpendicular to the thin film than the 375 K sample, indicating that the texture of the thin film is strongly influenced by the substrate temperature during deposition. The 375 K sample however exhibited roughly four times the H_c measured in the 450 K sample. This was explained as being a result of polycrystalline LTP grains of roughly 1–2 μm that developed in the 375 K sample whereas the 450 K sample developed much larger textured regions. These polycrystalline grains approach the single magnetic domain size for LTP MnBi, ~0.5 μm in an ideal domain, compared to the textured regions in the 450 K sample that were tens of microns

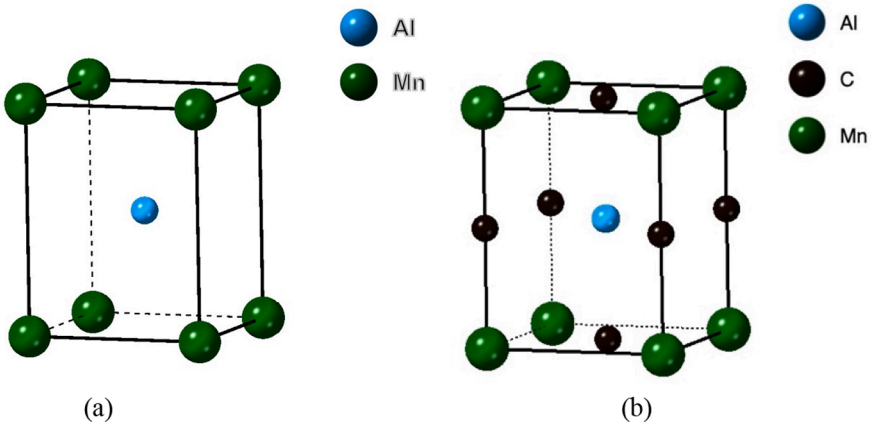

Fig. 10. The unit cell of the CuAu-type $L1_0$ τ phase shown without (a) and with interstitial carbon sites occupied (b).

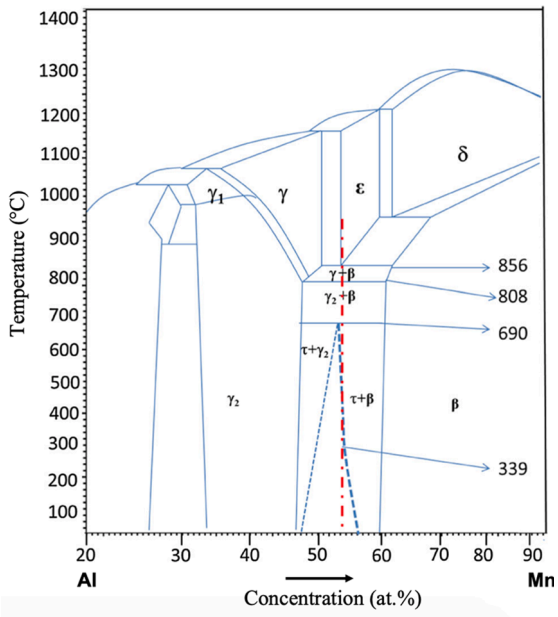

Fig. 11. The binary Mn-Al phase diagram with proposed boundaries of the τ phase region. From [74].

Qin *et al.* used a unique method of electrodeposition using an electrolytic solution of 1 M $MnSO_4$, 1 M $(MH_4)_2SO_4$, 5 mM Bi $(NO_3)_3$*$5H_2O$ and varying concentrations of Na_2EDTA [68]. Using a deposition potential of −1.36 V, they electrodeposited a $Mn_{54}Bi_{46}$ film onto a Cu substrate and vacuum annealed the film at 653 K for 3 h. Unfortunately, the resulting film was of very low LTP fraction, with a H_c of just 116 kA/m. XRD analysis showed that Bi was the primary phase present with exceptionally weak MnBi LTP peak intensity.

4. Manganese-Aluminum based magnetic materials

4.1. Mn-Al crystal structure and phase equilibria

The hard ferromagnetic $L1_0$ τ phase of the Mn-Al system has drawn particular interest due to the relative abundance of Al and low cost compared to Ga and Bi. This metastable phase possesses a CuAu-type tetragonal structure, shown in Fig. 10, with lattice parameters of $a = 0.273–0.277$ nm and $c = 0.354–0.358$ nm, which depend on composition [69-71]. This results in a magnetic moment per Mn atom of 2.3 μ_B, a magneto-crystalline anisotropy energy of 1.525 MJ/m^3, a theoretical saturation magnetization of 161 Am^2/kg, a density of 5200 kg/m^3, and a predicted $(\mathbf{BH})_{max}$ of ~101 kJ/m^3 [72,73]. The phase diagram shown in Fig. 11 shows the metastable τ phase exists only on the Mn rich side of the stoichiometric composition, i.e over the range in 50–60 at.% Mn, with the equilibrium γ_2 and β phases at lower and higher Mn contents, respectively. The exact boundaries of the τ phase region with the

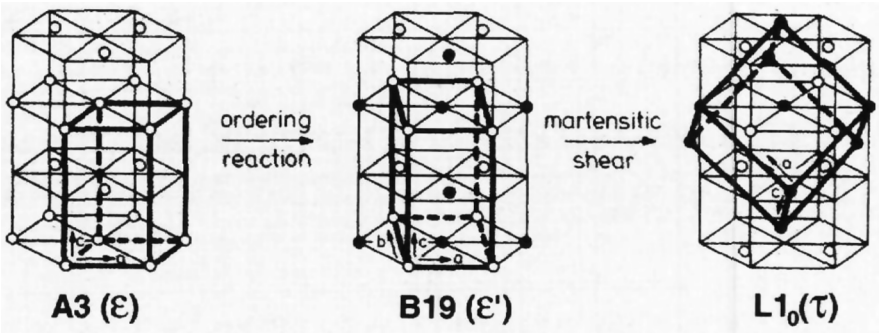

Fig. 12. The crystal structure transformation from the parent ε phase to the magnetic $L1_0$ τ phase through an intermediate ε' phase and via a martensitic shear transformation. The most recent research suggests that the ε to τ transition is not one single mechanism but a combination of martensitic and massive transformations. From [95].

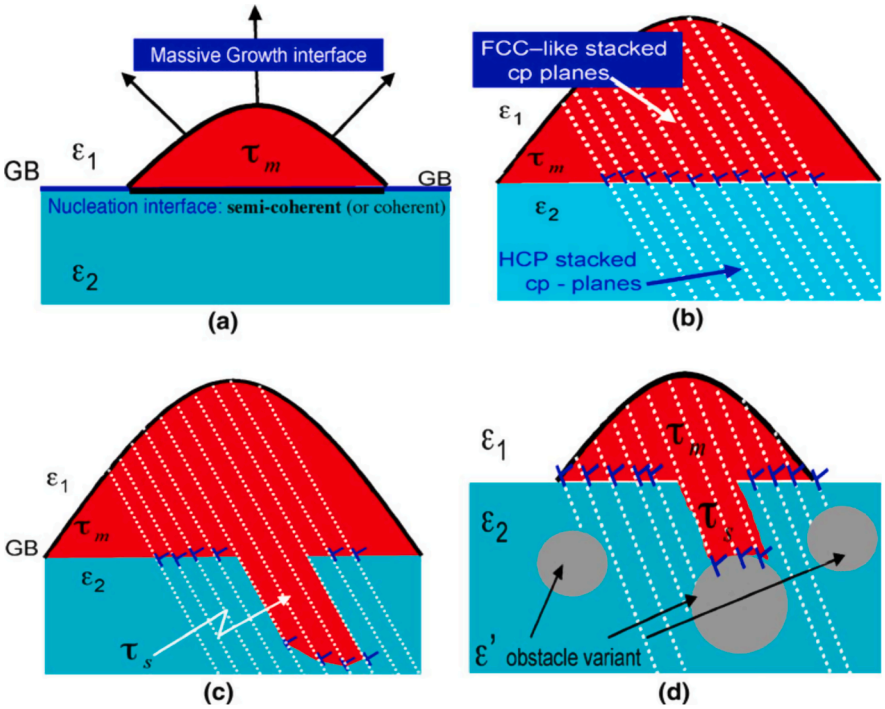

Fig. 13. The proposed model by Wiezorek et al. for the hybrid massive-martensitic transformation of ε phase to τ phase Mn-Al showing: a) nucleation of τ phase by massive mode along a parent ε phase grain boundary, b) the formation of partial dislocations along the grain boundary between the $L1_0$ and A3 structures, c) growth of the τ phase through martensitic mode by the propagation of the partial dislocations along the glissile close-packed planes, and d) ε' phase of an orientation that cannot be sheared along the glissile plane acts as an obstacle to dislocation motion and thus slows τ phase formation by martensitic mode. From [105].

surrounding equilibrium phases is still unclear [74,75]. τ phase decomposes easily into these two surrounding phases, presenting a major challenge to the formation and stable preparation of the τ phase in permanent magnets [76]. Alloying with carbon has been shown to stabilize the ε and τ phases and slow decomposition into the γ_2 and β phases without significantly diminishing the magnetic properties, yet, carbon decreases T_C, e.g. from 640 K to 560 K with the addition of 2 at.% C [77-83]. Carbon increases the *c*-axis, decreases the *a*-axis, and increases the unit cell volume at concentrations from 0 to 4 at.%, which indicates that the carbon atom likely occupies the (1/2, 1/2, 0) or (0, 0, 1/2) interstitial sites in the unit cell although substitutional site occupancy has also been suggested, but is less likely [81,84-88].

Research on Mn-Al has led to methods for producing the τ phase from the high-temperature hexagonal close-packed (HCP) ε phase, see Fig. 11. The most-established method begins with a high-temperature homogenization anneal (>1143 K) of the material and then a rapid quench to retain the ε, thereby avoiding formation of the equilibrium γ_2 and β phases[89]. This is followed by a lower temperature anneal at 623–923 K to allow the transformation from ε to τ [90]. The ε to τ formation has been the subject of significant

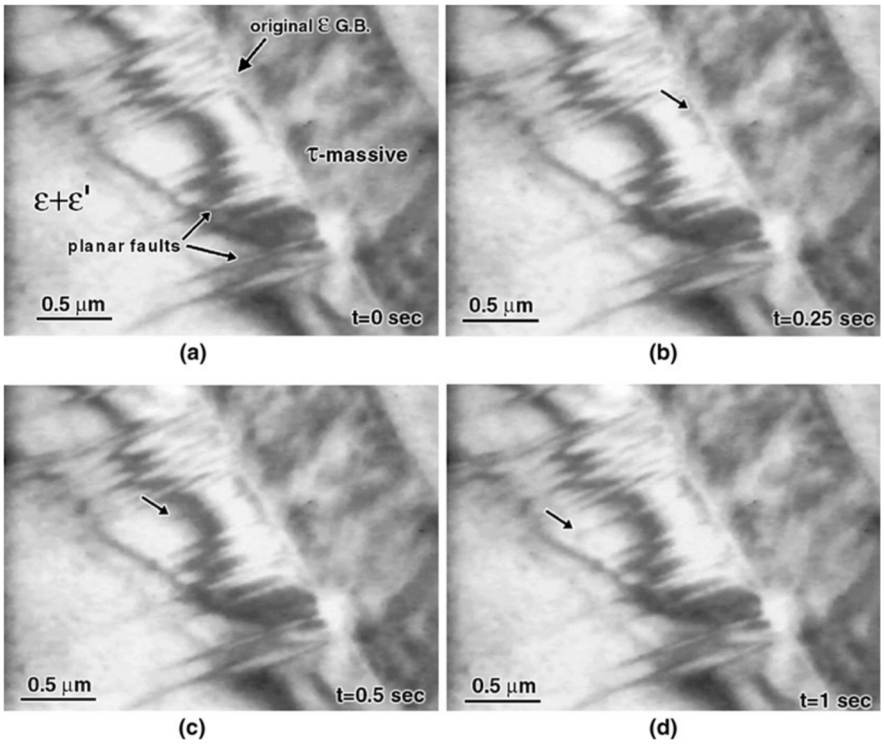

Fig. 14. In-situ TEM images of the growth of the τ phase through martensitic mode along planar faults at the grain boundary between the ε + ε' mixed phase region and the massive mode τ phase region. The growth of one τ phase shear plane into the ε + ε' mixed phase region is shown by the arrow at 0 s (a), 0.25 s (b), 0.5 s (c), and 1 s (d). From [105].

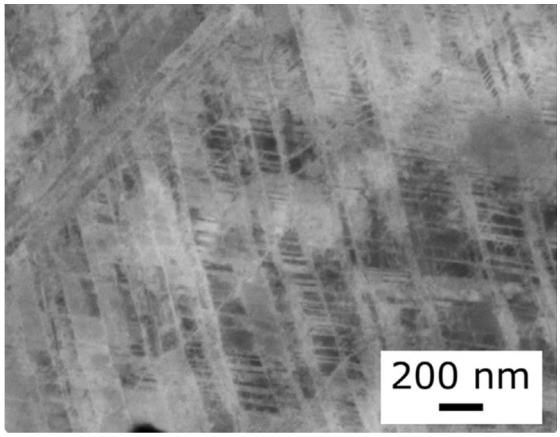

Fig 15. The poly-twinned microstructure of $Mn_{54}Al_{46}$ after cold-swaging by Bittner et al. The "macro-twins" are roughly 200 nm apart (oriented primarily vertically in this image) whereas the "micro-twins" are 20–30 nm apart arranged within the macro-twins. From [117].

research effort [91-99]. One generally accepted explanation is that when the ε phase is cooled at a moderate rate (10–20 K/min) the ε phase reorders into the intermediate orthorhombic B19 ε' phase through a diffusional process [91,94,95,100]. The process by which this intermediate phase transforms into τ phase is not yet fully clear. Early research suggested the sole mechanism was a compositionally invariant shear driven martensitic transformation, as shown in Fig. 12. τ phase grains have been observed to form with a crystallographic coherence to the parent ε phase grain following the martensitic model. Starting with a parent ε phase grain, three possible ε' crystal variants have been observed to nucleate and grow into the parent ε phase before forming periodically-spaced stacking faults that transform into a twinned τ phase, implying that the microstructure of the parent phase has an impact on the τ phase produced and must be taken into consideration when producing τ phase magnets [101–103].

Hoydick *et al.* have suggested that the process is a massive transformation, whereby the elemental composition remains unchanged and a diffusion-driven, rather than shear, process nucleates heterogeneously on the grain boundaries of the ε phase [104]. Mullner *et al.* found sufficient evidence that both a shear and nucleation process occurred in the τ phase formation, as later corroborated by Wiezorek *et al.* and Si *et al.* [105,106]. In these studies, it was suggested that neither the massive nor the martensitic transformation alone could completely describe the formation and resulting microstructure of the τ phase. Therefore, they concluded that the formation of the τ phase occurs via a combination of the two transformation modes [107]. The model put forth by Wiezoreck *et al.* suggests that at temperatures from 773 to 973 K, the τ phase nucleates via a massive transformation on the existing ε phase, nucleating dislocations along the grain boundary. The martensitic shear transformation then takes place along the planes of these dislocations, forming the τ phase in "plates" that move into the parent ε phase as shown in Figs. 13 and 14. In this way the overall transformation to τ phase is described as a simultaneous hybrid massive-martensitic transformation. Genc *et al.* suggested using high-energy XRD that the formation of ε' may be dependent on the composition [108]. They showed that upon heating the quenched-in ε phase from 300 to 724 K at 10 K/min, ε' formed in Mn_xAl_{1-x} for the compositions $50.5 < x < 55.2$ at.% but did not form at higher Mn concentrations. They also observed that during this heating from 300 to 724 K in the absence of ε' phase, ε phase decomposed into the equilibrium γ_2 and β phases without forming τ phase. Yet, other work has shown that it is possible to form τ phase at Mn concentrations above 55 at.% [109-111]. Therefore, it is still not fully clear what impact the two modes or the intermediate ε' phase have on the microstructure and what the implications are for processing techniques. For example, Si *et al.* and Sologubenko *et al.* have suggested that over a larger temperature range, from room temperature to 900 K, the relative contributions of the two transformation modes may show a temperature dependence, with the diffusion-driven massive transformation dominating at high temperatures and becoming insignificant compared to the martensitic contribution at temperatures below 650 K [106,112]. Solobenko *et al.* also identified that in the Mn-Al-C system the martensitic mode is more dominant at higher concentrations of Mn and C, whereas the massive mode is encouraged by higher concentrations of Al [112]. The hybrid massive-martensitic transformation to τ phase has been shown to produce twins, antiphase boundaries (APB), and dislocations [107,113-115]. Twins and APBs have both been suggested to decrease M_r, H_c, and $(\mathbf{BH})_{max}$, whereas dislocations may have a positive effect on H_c [116]. Therefore, a careful control of defect structures is necessary to optimize the magnetic performance of the τ phase.

4.2. Mn-Al bulk processing

4.2.1. Mn-Al bulk processing from melt

Similar to Mn-Ga and Mn-Bi, the most straightforward approach for bulk processing of Mn-Al is by arc-melting. However, unlike MnGa, Mn_3Ga, and MnBi, which are equilibrium phases, the magnetic $L1_0$ τ phase is metastable at room temperature and the heating and cooling rates during processing of Mn-Al are critical to forming the τ phase. Generally, bulk processing techniques begin with a homogenization anneal above the ε phase transition temperature of 1143 K for durations ranging from 1 h to many days depending on the homogeneity of the as-cast starting material [117,92,80]. The simplest technique is to then cool the ε phase bulk material at a moderate rate to allow it to transform into the ferromagnetic τ phase. Fang *et al.* demonstrated this by heating and cooling small 10 g $(Mn_{55}Al_{45})_{98}C_2$ specimens sealed in crystal sapphire tubes under vacuum [91]. The samples were heated to 1173 K then cooled at 600 K/min, 10 K/min, or 2 K/min while performing *in-situ* XRD. They observed that at the rapid cooling rate of 600 K/min the resulting ingot consists of roughly equal parts by wt.% of the τ and ε phase. At the moderate cooling rate of 10 K/min the sample consisted of >95 wt.% τ phase, while at the slowest rate of 2 K/min the sample initially transformed into the τ phase but then decomposed into the γ_2 and β phases. Hence, a moderate cooling rate is optimum to allow adequate time for the τ phase transformation to occur without decomposition into the γ_2 and β phases.

Palanisamy *et al.* demonstrated that it was even possible to directly cast a τ phase $Mn_{55}Al_{45}$ bulk alloy from melt [73]. They modified the cooling rate by suction casting from melt into copper crucibles of different inner diameter, from 2 to 12 mm, forming cylinders roughly 5 mm in height. They used a finite element simulation to model the cooling rate at the center of each cast cylinder and correlated these to the phases present in the actual samples. They saw a mixture of ε and τ phases present in the 6 mm diameter sample, which had a cooling rate of ~140 K/min, only the τ phase present in the 10 mm diameter sample, which had a cooling rate of ~60 K/min, while partial decomposition into the β phase was observed in the 12 mm diameter sample, which had a cooling rate of ~20 K/min. Shafeie *et al.* performed a similar experiment to directly cast τ phase from melt without an annealing step [79]. They synthesized 20 g $(Mn_{55}Al_{45})_{98}C_2$ ingots from the molten state in two ways. First, they held the melt at 1673 K for 10 min before simply furnace cooling. Second, they held the melt at 1673 K for 10 min, then cooled to 1473 K, where it was held for 30 min before furnace cooling. They did not provide an estimation of the cooling rate. However, they demonstrated that the second method of dwelling at 1473 K for 30 min increased the amount of the τ phase and decreased the fractions of γ_2 and β phases when compared to the first method of simply cooling from 1673 K. SEM analysis showed that the first method produced an inhomogeneous distribution of Mn and Al, forming Mn-rich regions within an Al-rich matrix. The second method displayed a much more homogeneous elemental distribution and grain structure, suggesting that the dwell was successful in homogenizing the ingot and forming a higher concentration of ε phase. It should be noted that in the case of the second method, the amount of τ phase was 99.5 wt.% at the top of the ingot but only 95.1 wt.% at the middle, suggesting that for larger scale ingots than 20 g this method may not form uniform τ phase due to the size-dependence of the cooling rate, as shown by Palanisamy *et al.*

Shao *et al.* have demonstrated that the conventional industrial process of strip casting can be used to form a high τ phase volume fraction in 2.5 × 0.5 mm strips of $Mn_{54}Al_{46}$ resulting in a $M_{6.4MA/m}$ of 114 Am^2/kg and but a very low H_c of <80 kA/m [109]. However, they did not present any details of the thermal conditions used to produce the strip cast in this case, making it difficult to evaluate the usefulness of this technique.

Table 7
Composition, phase, method, and magnetic properties for selected τ phase Mn-Al bulk magnets.

Reference	Composition	Processing Technique	H_c kA/m	M_r Am^2/kg	M_s Am^2/kg (Saturating Field kA/m)	BH_{max} kJ/m^3	T_{curie} K
Bittner *et al.* 2017 [117]	$Mn_{53}Al_{45}C_2$	1373 K homogenization for 2 days in Ar then water quench	15.9		119 (3820)		
	$Mn_{53}Al_{45}C_2$	" Then 1373 anneal for 30 min and quench, then 773 K anneal for 1 h and quench	95.5		116 (3820)		
	$Mn_{54}Al_{46}$	1373 K homogenization for 2 days in Ar then water quench. Then cold swage deformed to a log strain of 1.1	226.8	71.5		24	
	$Mn_{54}Al_{46}$	" Then 773 K anneal for 1 h	64.5				
Chraplyvy *et al.* 1980 [198]	$Mn_{53.2}Al_{44.5}C_{1.7}Ni_{0.6}$	1373 K homogenization then water quench a 3.5 mm diameter and 0.1 mm thick disk. Laser irradiation heated on one side to 813 K for 5 min	80		85 (1194)		
Chaturvedi *et al.* 2014 [130]	$Mn_{54}Al_{46}$	Ball milled for 20 h then ECAE at 698 K for 15 min	334		24.5 (796)		
	$Mn_{54}Al_{46}$	Ball milled for 20 h then ECAE at 698 K for 30 min	334				
	$Mn_{54}Al_{46}$	Ball milled for 20 h then ECAE at 698 K for 45 min	334	26.3	39.8 (796)		
Dehghan and Ebrahimi 2019 [127]	$Mn_{51}Al_{47}C_2$	1373 K homogenization for 12 h into 1173 K anneal for 30 min under vac quartz encapsulation and water quench	34.6	18.2	78.9 (1194)		
		" Then hot compression of 6 mm diameter and 9 mm high ingot to 50% of starting height at 923 K and 0.001 s^{-1} strain rate	105.0	30.8	73.8 (1194)		
Feng *et al.* 2021 [138]	$(Mn_{53}Al_{45}C_2)_{99.4}Ni_{0.6}$	1373 K homogenization for 2 days in Ar, quenched in water, then 773 K anneal for 1 h. Then hot uniaxial compression at 973 K for 10 min to a 75% height reduction	139		122 (11141)		543
Gavrea *et al.* 2017 [137]	$Mn_{52}Al_{46}T_2$	As-Cast	70	21.05	93.50 (5570)		654
		As-Cast wrapped in Ta foil and 743 K anneal for 6 h under Ar then water quench	55	14.60	87.60 (5570)		668
		As-Cast wrapped in Ta foil and 1323 K anneal for 1 h under Ar then water quench	43	17.45	98.54 (5570)		651
	$Mn_{50}Al_{46}T_4$	As-Cast	34	11.02	81.21 (5570)		664
		As-Cast wrapped in Ta foil and 743 K anneal for 6 h under Ar then water quench	27	11.02	75.54 (5570)		668
		As-Cast wrapped in Ta foil and 1323 K anneal for 1 h under Ar then water quench	27	8.52	83.10 (5570)		664
Jia *et al.* 2018 [119]	$(Mn_{54}Al_{46})_{98}C_2$	Optical floating zone single crystal cast at 1.1 $\mu m.s^{-1}$ then ramp to ~848 K at 20 K/min	~16		~90 (1592)		
		Bridgeman furnace drawn at 200 $\mu m.s^{-1}$ to form columnar grains	~80		~85 (1592)		
		Bridgeman furnace drawn at 800 $\mu m.s^{-1}$ to form dendritic grains then ramp to ~823 K at 20 K/min	~96		~90 (1592)		
		Melt-spun ribbons at 25 $m.s^{-1}$ to form ultrafine columnar grains	117		~90 (1592)		
Kinemuchi *et al.* 2016 [99]	$Mn_{47}Al_{53}$	Coarse powder pelletized into gold capsule and high-pressure synthesized at 9 GPa and 1273 K for 1 h	~170		~45 (7958)		
	$Mn_{50}Al_{50}$	"	~181		~78 (7958)		
	$Mn_{52}Al_{48}$	"	~155		~115 (7958)		
	$Mn_{53}Al_{47}$	"	~133		~108 (7958)		
Kontos *et al.* 2019 [134]	$(Mn_{55}Al_{45})_{99.98}B_{0.02}$	Drop-synthesized at 1673 K for 10 min in Ar then 1273 K anneal for 10 min and water quench.	~245		~43 (1440)		646–664
Madugundo *et al.* 2016 [128]	$Mn_{53.5}Al_{44.5}C_2$	1373 K homogenization anneal then quench, 823 K anneal for 20 min, crushed before high energy ball milling for 2 h, then again 823 K anneal for 20 min. Then hot compacted under 275 MPa at 973 K into 10 mm diameter 5 mm long cylinder	263	28	50 (2387)	4.8	
		" But compacted under 1.2 GPa into 5x5x4 mm and microwave sintered at 973 K for 10 min under Ar, then 873 K anneal for 10 min	88	39	94 (2387)	4.0	
		1373 K homogenization anneal then quench, 823 K anneal for 20 min, then hot deformed to 75% height at 973 K under uniaxial pressure	175 (⊥)	50 (⊥)	82 (2387) (⊥)	14.3 (⊥)	
Mican *et al.* 2016 [136]	$Mn_{54}Al_{46}$	Wrapped in Ta foil, 743 K anneal for 6 h then quench			112 (7958)		645
	$Mn_{50}Al_{46}Ni_4$	Wrapped in Ta foil, 743 K anneal for 6 h then quench			106 (7958)		634
	$(Mn_{57}Al_{43})_{98.9}C_{1.1}$		228	44.3	78.4 (1592)	12.4	

(*continued on next page*)

Table 7 (*continued*)

Reference	Composition	Processing Technique	H_c *kA/m*	M_r Am^2/kg	M_s Am^2/kg (Saturating Field *kA/m*)	BH_{max} kJ/m^3	T_{curie} *K*
Munoz-Rodriguez *et al.* 2020 [111]		Gas-atomized powder. Hot compacted at 873 K under 300 MPa for 30 min (15 min unloaded 15 loaded)					
		" But HEBM for 60 s before hot compaction	257	39.2	67.6 (1592)	9.5	
		Gas atomized powder. Annealed at 873 K for 30 min. Hot compacted at 873 K under 300 MPa for 5 min (2 min unloaded 3 loaded)	229	44.2	77.0 (1592)	11.0	
		" But HEBM for 60 s and annealed at 698 K for 10 min before hot compaction	242	42.3	73.0 (1592)	10.7	
Ohtani *et al.* 1977 [80,121,122]	$Mn_{53}Al_{45}C_2$	1373 K homogenization anneal for 1 h, quench to 773 K, 873 K anneal for 30 min, hot extruded at 973 K under 785 MPa, all in air	215 (‖)	0.61 T (B_r) (‖)		49 (‖)	
		" Then 973 K anneal for 10 min	239 (‖)	0.61 T (B_r) (‖)		55.7 (‖)	
Oygarden *et al.* 2019 [164]	$(Mn_{55}Al_{45})_{98}C_2$	Ball milled for 10 h, compressed into 7 mm dia. pellet under 260 MPa, 1323 K anneal for 20 min and air quench	119	41*	85 (1592)*		
Palanisamy *et al.* 2016 [73]	$Mn_{55}Al_{45}$	Melted and suction cast into 10 mm diameter rod	78.0		111 (11141)		668
		1273 K homogenization anneal for 5 h then water quench, 673 K anneal for 5 h then water quench	91.9		128 (11141)		668
Park *et al.* 2010 [72]	$Mn_{54}Al_{46}$	1423 homogenization anneal for 24 h then deoxygenated and deionized water quench, then 723 K anneal for 1 h in vac			98.3	37.4	661
Qian *et al.* 2019 [199]	$Mn_{54}Al_{46}$	Start as powder, 1373 K homogenization anneal for 10 h, then 873 K anneal for 5 min under Ar and H. Then compacted under 12.5 GPa	310		~40		
	$Mn_{53}Al_{45}C_2$	"	175		88		
Radulov *et al.* 2019 [191]	$Mn_{53}Al_{47}$	Ball milled, then electron beam melted on a preheated platform at 1103 K in 100 μm layers, 1373 K anneal for 60 h then 773 K anneal for 30 min	47.8	0.18 T (B_r)	100 (1592)	1.85	
Sakamoto *et al.* 1980 [125,126]	$Mn_{52.6}Al_{45.2}C_{1.7}Ni_{0.5}$	Cast ingot homogenized at 1373 K for 2 h then air-blower quench to 773 K, 873 K anneal for 20 min, then hot extruded at 973 K, then axially strained at 933 K at 7 $mm.s^{-1}$ to log strain of −1.21. 953 K anneal for 5 min to finish	326	0.46 T (B_r)		33	
Saravanan *et al.* 2015 [110]	$Mn_{56}Al_{44}$	Tungsten-C ball milling for 25 h, spark plasma sintered under vac, 75 MPa, 973 K for 5 min, then 1100 K anneal for 20 min under vac	194		28 (3000)		
Shafeie *et al.* 2019 [79]	$(Mn_{55}Al_{45})_{98}C_2$	Drop synthesized at 1673 K	56	20.4	108 (7162)		560
		" Then 1473 anneal for 30 min before cooling	19	11.5	120 (7162)		550
Shao *et al.* 2017 [109]	$Mn_{54}Al_{46}$	Strip cast into 2.5 × 0.5 mm strip	< 80		114 (5570)		
Si *et al.* 2019 [131]	$(Mn_{54}Al_{46})_{97.56}C_{2.44}$	Gas-atomized powder, 60 K anneal for 20 min. Then compacted under 3.1 GPa	271	39	90 (3183)		
Si *et al.* 2019 [118]	$Mn_{54}Al_{46}$	Melt spun ribbons at 52 $m.s^{-1}$ then 758 K anneal for 5 min	151	25	78 (6366)		
	$(Mn_{54}Al_{46})_{97.56}C_{2.44}$	"	104	30	122 (6366)		
	$(Mn_{54}Al_{46})_{97.56}C_{2.44}$	" Crushed, compacted into bulk pellet under 6 GPa for 20 min	302		~60 (6366)		
Si *et al.* 2020 [135]	$Mn_{52.9}Al_{45}B_{1.2}N_{0.9}$	1323 K homogenization anneal for 40 h in vac and water quench, 700 K anneal for 15 min, then severe plastic deformation under 6 GPa and 10 turns of torsion	430	19	45 (1592)		620
		" Then 623 K anneal for 40 min	406	33	77 (1592)		
Thielsch *et al.* 2017 [123]	$Mn_{53}Al_{45}C_2$	1373 K homogenization anneal for 2 days and water quench, then hot extruded at 953 K reducing area ratio by 4	159 (⊥) 127 (‖)	0.47 T (‖) 0.26 T (⊥) (B_r)			533
Tyrman *et al.* [132]	$Mn_{54}Al_{44}C_2$	Melt spun ribbons, cryo-milled, then SPS at 823 K under 400 MPa	~150 (‖) ~137 (⊥)	~40 (⊥)	~79 (1512) (‖) ~83 (1512) (⊥)		
Wang *et al.* 2011	$Mn_{54}Al_{44.4}Zn_{1.6}$	Induction melted in Ar, water quench, then 693 K anneal for 1 h in vacuum	125		~70 (1194)		645
Zhang *et al.* 2018 [120]	$(Mn_{54}Al_{46})_{97}C_3$	Optical float zone furnace pulled at 4 mm/h, then 903 K anneal for 3 min under 320 MPa uniaxial compression			113		

Note: Magnetic properties are at room temperature and isotropic unless otherwise noted.
* Moment is converted from emu/cm^3 or kA/m using a density of 5200 kg/m^3 for τ phase.
(⊥) Indicates measurement perpendicular to direction of magnetic alignment during annealing or bonding.
(||) Indicates measurement parallel to direction of magnetic alignment during annealing or bonding.
~ Indicates a value determined from a graph rather than taken in text.

To circumvent the challenge of controlling the cooling rate throughout a sample, the more common experimental procedure has been to rapidly quench-in the ε phase, such that there is inadequate time for transformation to the τ phase, then perform a subsequent low-temperature anneal. For a direct comparison, Palanisamy *et al.* compared the aforementioned suction cast magnets with a $Mn_{55}Al_{45}$ magnet produced by homogenizing at 1273 K for 5 h, quenching into water to retain the ε phase, and subsequently annealing at 673 K for 5 h followed by a water quench [73]. Comparing the two bulk magnets, the quenched and annealed magnet had a higher H_c and M_s, at 91.9 kA/m and 128 Am^2/kg respectively, compared to the direct cast magnet, at 78.0 kA/m and 111 Am^2/kg. This suggests that the annealing step allowed for a more complete transformation to the τ phase compared to directly casting from melt. Si *et al.* melt spun ribbons of both $Mn_{54}Al_{46}$ and $(Mn_{54}Al_{46})_{97.56}C_{2.44}$ at a wheel speed of 52 m.s^{-1} to form ε phase ribbons [118]. They then annealed the unalloyed and carbon-alloyed ribbons at 739 K and 758 K, respectively, for 5 min followed by furnace cooling. A longer annealing time was necessary for the carbon alloyed sample to transform to the τ phase because the addition of carbon has been shown to increase the temperature of the transformation to the τ phase [77]. Annealing the carbon-alloyed ribbon at 733 K for 20 min and furnace cooling did not fully transform the ε phase into τ despite the longer duration. They observed that the Mn-Al ribbons were composed of ε phase and a small unquantified fraction of γ_2 phase. This γ_2 phase fraction was retained after annealing while the ε phase was fully transformed into τ. The resulting ribbon had a $M_{6.4MA/m}$ of 78 Am^2/kg and a H_c of 151 kA/m. In contrast, the carbon-alloyed ribbons did not show any γ_2 phase, only the ε phase, suggesting that the carbon addition suppressed the formation of the γ_2 phase at this wheel speed. As a result of the higher amount of the τ phase and lack of secondary phases for pinning sites, the carbon-alloyed ribbons had a higher $M_{6.4MA/m}$ of 122 Am^2/kg but a lower H_c of 104 kA/m. They crushed the carbon-alloyed ribbons and compacted them into a bulk pellet under a pressure of 6 GPa for 20 min. However, while this refined the grain size and increased H_c to 203 kA/m, pelletizing came at the expense of reducing the $M_{6.4MA/m}$ by half to ~60 Am^2/kg.

Jia *et al.* compared the microstructure and magnetic properties of melt-spun $(Mn_{54}Al_{46})_{98}C_2$ ribbons to those of the same composition magnets formed using either an optical floating zone or a Bridgman furnace [119]. In all cases, roughly the same M_s values of ~90 Am^2/kg were achieved. The primary difference between the magnets was in the resulting H_c. The ribbons were spun from melt at 25 m.s^{-1} forming ultrafine columnar grains with a H_c of 117 kA/m. Using a Bridgman furnace, where the furnace hot zone was moved along the length of the specimen at a rate of 200–800 μm.s^{-1}, they were able to observe a shift from columnar to dendritic grains as the moving speed of the furnace was increased. The 800 μm.s^{-1} sample was composed of primarily ε phase, requiring an additional anneal (ramp to ~823 K at 20 K/min) to form the magnetic phase without significantly affecting the grain size. The dendritic-grained material tended to be finer than the columnar-grained material and consequently showed higher coercivities (H_c = ~80 kA/m at 200 μm.s^{-1} and H_c = ~96 kA/m at 800 μm.s^{-1}). The sample prepared in the optical floating zone furnace at moving velocity of 1.1 μm.s^{-1} was composed of a 3 mm long single crystal of the ε phase, which is orders of magnitude larger than the grains formed by the other methods. After annealing to form the τ phase (ramp to ~848 K at 20 K/min), this sample had the lowest H_c of ~16 kA/m, demonstrating that refining the grain size plays a key role in improving the H_c in bulk Mn-Al magnets.

Zhang *et al.* also produced a carbon-alloyed ε phase single crystal, $(Mn_{54}Al_{46})_{97}C_3$, using an optical floating zone furnace at the same drawing rate of 1.1 μm.s^{-1} [120]. However, to form τ phase they used a 903 K anneal for 3 min while the specimen was under uniaxial compression. In the absence of compression during annealing, the ε phase single crystal transformed through an observed martensitic transformation into a polycrystalline magnetically isotropic τ phase magnet with a high density of twins. However, by using compression along the [1 -1 1] direction of the ε phase during annealing, the martensitic transformation was constrained to just one variant of τ phase, the magnetic easy axis [0 0 1] (which is parallel to the [1 -1 1] direction of the ε phase), formation of twins was suppressed, and consequently the resulting single crystal magnet displayed high magnetic anisotropy along the axis of compression and a high M_s of 113 Am^2/kg. Kojima *et al.* demonstrated that it was also possible to form a single crystal τ phase magnet by applying uniaxial stress during the phase transformation from a single crystal of ε phase [103]. Starting with a $Mn_{54.8}Al_{41.6}C_{3.6}$ ε phase single crystal cast in a Bridgman furnace, they sectioned the single crystal and annealed multiple samples at 833 K under 294 Pa at various uniaxial compressive stress orientations. They achieved a τ phase single crystal when compression was applied along a direction tilted ~50° away from the [0 0 0 1] of the ε single crystal towards the [1 -1 0 0] direction, resulting in a τ single crystal of M_s = 106 Am^2/kg. They observed coherence of the orientation of the τ crystal to that of the parent ε such that (1 1 1) and (-1 1 0) of the τ was parallel to (0 0 0 1) and (1 1 -2 0) of the ε, respectively. The [0 0 1] τ easy axis developed at a direction tilted ~84° away from the axis of compression. Notably, they confirmed that when the compression was applied along the [0 0 0 1] or [2 -1 -1 0] axes of the ε parent, the resulting τ phase was polycrystalline and lacked a preferred orientation. Mechanical stress, thus, has a strong effect on the resulting τ phase microstructure, particularly in developing crystalline and magnetic anisotropy. However, the single crystals prepared by Zhang *et al.* and Kojima *et al.* achieved no greater than ~70% the theoretical maximum M_s of ~161 Am^2/kg, and had lower M_s than other Mn-Al-C bulk polycrystalline magnets in this review (see Table 7) [79,117,118]. This demonstrates that controlling the martensitic mode of the τ phase transformation to a single crystal without consideration of the massive mode is not sufficient to maximize M_s. Additionally, even in single crystal τ, the presence of excess Mn (above 50 at.%) in the $L1_0$ structure is likely to cause defects in the ordered lattice and lead to AFM coupling between Mn atoms, preventing the M_s from reaching its theoretical maximum [114].

Seminal work by Ohtani *et al.* in 1977 produced what still remains today as the highest $(\mathbf{BH})_{max}$ for a Mn-Al-C magnet ever

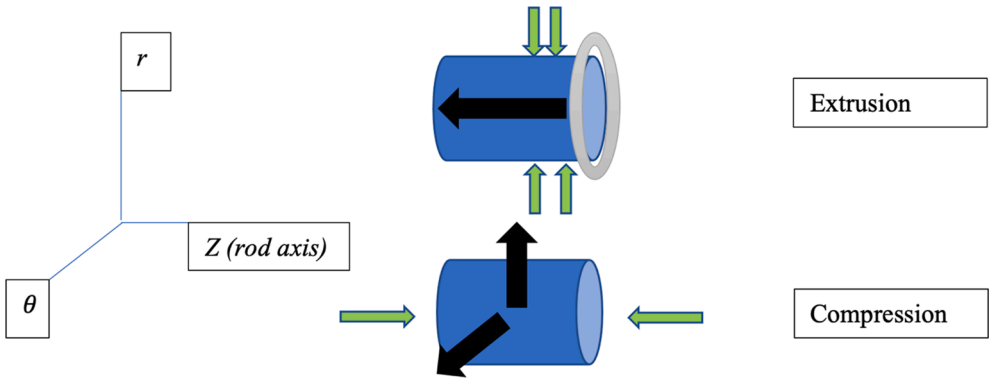

Fig. 16. Schematic of the effects of mechanical stress (green arrows) on magnetic anisotropy. The magnetic easy-axis (black arrows) is aligned with the rod extrusion direction (Z) during hot extrusion but can be reoriented perpendicularly through compression to align with the radial (r) and tangential (θ).

produced, at 55.7 kJ/m^3, for the composition $Mn_{53}Al_{45}C_2$ [80,121,122]. To achieve this, they performed a 1373 K homogenization anneal for 1 h, quenched the $Mn_{53}Al_{45}C_2$ to 773 K, tempered it at 873 K for 30 min, and finally hot extruded it at 973 K at a stress of 785 MPa, with an area reduction ratio of 7.4:1. A post-extrusion anneal at 973 K for 10 min improved H_c from 215 to 239 kA/m but did not affect M_r. The hot extrusion led to a decrease in the grain size and the development of strong magnetic anisotropy aligned with the extruded rod axis. The magnetic anisotropy is due to the formation of a τ phase *c*-axis crystal texture along the rod axis during extrusion. More recently, Thielsch *et al.* also showed that hot extrusion developed magnetic anisotropy along the rod extrusion direction [123]. Investigating the same $Mn_{53}Al_{45}C_2$ composition sample, they performed a homogenization anneal at 1373 K for 2 days, quenched the alloy into water, and then hot extruded at 953 K with an area reduction ratio of 4:1. They found magnetic anisotropy of degree 0.45 along the rod extrusion direction and a microstructure of very fine recrystallized grains amongst retained large grains that did not undergo recrystallization. They quantified the anisotropy as a degree from 0 (magnetically isotropic) to 1 (uniaxial magnetic anisotropy) using the formula:

$$\text{Degree of anisotropy} = (M_r\| - M_r^{\perp})/M_r\|$$

where $M_r\|$ is the remanence parallel to the magnetically easy axis (along the rod extrusion direction) and $M_r^{\perp}$ is the remanence perpendicular to the magnetically easy axis [115]. The large retained grains, up to 50 μm, showed a high density of twins. In contrast, the 700 nm recrystallized grains were roughly the size of a single magnetic domain, ~770 nm in this material, and, thus, were highly resistant to magnetic reversal. They suggested that if the material was fully recrystallized, thereby eliminating the large grains, the H_c of the material would be greatly improved. The magnet produced by Ohtani *et al.* showed a much higher H_c (239 kA/m) compared to that in the latter study (159 kA/m), and subsequent SEM analysis of Ohtani *et al.*'s magnet revealed that there were no grains larger than 5 μm retained after the hot extrusion and heat treatments [124]. In 1980, Sakamoto *et al.* further refined the hot extrusion processing technique developed by Ohtani *et al.* by demonstrating that it was possible to change the magnetic anisotropy from parallel to the rod extrusion direction to perpendicular for a $Mn_{52.6}Al_{45.2}C_{1.7}Ni_{0.5}$ bulk magnet, see Fig. 16 [125,126]. They performed a 1373 K homogenization anneal for 2 h, air-blower quenched to 773 K, then tempered at 873 K for 20 min. This ingot was hot extruded at 973 K, imparting a logarithmic strain of 1.4 in the extrusion direction. Finally, the extruded billet was compressed along the rod extrusion direction at 933 K, to a logarithmic strain of −1.2, and annealed for 5 min at 953 K. They observed that the sample without compression showed anisotropic magnetic behavior with its easy axis along the rod extrusion direction, as observed by Ohtani *et al.* [80] and Thielsch *et al.* [123]. For increasing hot compressive strains, they observed a swap in *c*-axis orientation from parallel to the rod axis to perpendicular. This was shown by the decreasing M_r in the rod axis direction and the increasing M_r in the radial direction, resulting in a $(\mathbf{BH})_{max}$ of 33 kJ/m^3. They observed the same swap in *c*-axis orientation in a magnet processed under the same conditions without Ni alloying as well. Therefore, even small amounts of compressive strain are sufficient to reorient the *c*-axis in this material from parallel to the rod extrusion axis to perpendicular so that the c-axis is uniformly distributed in the plane perpendicular to the extrusion axis. Subsequent investigations have shown that for an Mn-Al-C ingot without any initial anisotropy, compressive strains up to 50% develop magnetic anisotropy parallel to the axis of compression, while increasing to 75% strain brings about the perpendicular change to magnetic anisotropy [127]. For example, Madugundo *et al.* fabricated a bulk rod using arc-melting without any initial anisotropy [128]. They performed a 1373 K homogenization anneal and quench, followed by an 823 K anneal for 20 min, and then performed hot uniaxial compression along the rod length axis at 973 K, reducing the length of the bulk ingot by 75%. This process did not include a hot extrusion step to develop any anisotropy parallel to the deformation direction. The magnet showed a magnetic texture of degree 0.26 in the plane perpendicular to the axis of hot compression and a $(\mathbf{BH})_{max}$ of 14.3 kJ/m^3 in this plane. It also exhibited the same small recrystallized grain structure as other hot-deformed magnets with grains less than 500 nm. However, this magnet only achieved roughly half the $(\mathbf{BH})_{max}$ of that obtained by Sakamoto *et al.* due in part to its lower H_c of 175 kA/m compared to 326 kA/m. Additionally, this magnet displayed significant decomposition into the γ_2 and β phases after hot deformation, which also diminished M_s.

Bittner *et al.* demonstrated that the dislocation density has a strong effect on the H_c in bulk Mn-Al magnets [117]. They cooled a $Mn_{54}Al_{46}$ ingot encapsulated in a quartz tube from 1373 K by quenching into water to form the τ phase. Using cold swaging while encased in a stainless-steel tube to a logarithmic strain of 1.1 (area reduction ratio of 3:1), they formed a poly-twinned microstructure with a H_c of 226.8 kA/m, shown in Fig. 15. Upon annealing at 773 K for 1 h, the poly-twinned microstructure was left intact but H decreased to 64.5 kA/m. They observed that subsequent annealing increased the initial susceptibility, which suggests that domain wall pinning mechanisms dominated over nucleation. They also estimated the overall lattice distortion by determining the sharpness and number of observable Kickuchi bands (i.e. the quality of the pattern) using Fast Fourier Transformations of a large sample of 2,500 EBSD patterns and determined that the primary sources for the lattice distortions were dislocations. They observed that the Kickuchi band blurring, and thus, the overall lattice distortion, increased with increasing H_c Therefore, they concluded that the strain fields of dislocations, rather than twins or grain boundaries, were the primary source of pinning sites in this material. Si *et al.* performed cold-rolling on a $Mn_{54}Al_{46}$ τ phase ingot to an engineering strain of 0.15 [77]. H_c was increased by a factor of 4 and M_r by a factor of 3, but M_s decreased from ~130 to 100 Am^2/kg. Adding up to 3 at.% carbon to this ingot diminished the effect of cold rolling and decreased T_C. Carbon additions exceeding this concentration did not show a significant impact on the magnetic properties. Rial *et al.* performed cold-rolling on planar-cast $Mn_{55}Al_{45}$ ε phase ribbons for 10–50 passes through the cold-roller [129]. The initial ribbon showed a grain size of 106 nm and microstrain of 0.1% determined by the Scherrer method. The grain size was refined to 36 nm and 24 nm, while microstrain was increased to 0.28% and 0.42% for 10 and 50 passes, respectfully. After cold-rolling, the ribbons were annealed at 698 K for 10 min to transform into the τ phase. The annealed un-rolled ribbon formed 81 wt.% τ phase and 16 wt.% β phase ($M_r = 38$ Am^2/kg, $H_c = 119$ kA/m). After 10 passes the τ phase fraction decreased to 69 wt.% and β phase fraction increased to 31 wt.%, while after 50 passes the τ phase fraction was just 50 wt.% compared to 50 wt.% β phase. However, despite the phase decomposition, M_r only slightly diminished and remained constant at 35 Am^2/kg for 10–50 passes, while H_c increased to 175 kA/m after 10 passes and 279 kA/m after 50 passes. They concluded that the defects introduced into the microstructure of the ε phase ribbons during cold rolling provided nucleation sites for the β phase to form during the heat treatment. The combination of defects and β phase regions introduced by repeated cold-rolling therefore was shown to more than double coercivity with only minimal loss of M_r. $M_{1.6MA/m}$ was more strongly affected by cold-rolling, dropping from 76 Am^2/kg in the un-rolled sample to ~58 Am^2/kg in the 50 pass sample, more directly corresponding to the decomposition of the τ phase.

4.2.2. Mn-Al bulk consolidation from powder

Bulk Mn-Al samples have also been produced by powder consolidation. Chaturvedi *et al.* used an $Mn_{54}Al_{46}$ nano-crystalline ε phase powder precursor formed by gas-atomization followed by mechanical milling for 20 h [130]. The precursor powder was ~66% ε phase with the remaining fraction composed of γ_2 and β phases with an average grain size of 12 nm. Using equal-channel angular extrusion (ECAE), the powder was compacted under high pressure at 698 K and extruded through an angled die to impart a high shear strain. The duration of ECAE processing was varied from 15 to 45 min, which showed no significant change in $H_c = 334$ kA/m. However, M_s under an applied 796 kA/m field was shown to increase from 24.5 Am^2/kg to 39.8 Am^2/kg for 15 and 45 min extrusions, respectively. They concluded that even at the longest ECAE duration the transformation from ε to τ phase was incomplete by this method and the magnetic properties could be improved by performing ECAE at 648 K for 30 min and then annealing at 673 K for 30 min to maximize the τ phase fraction. They also demonstrated the high-temperature stability of magnets produced by this method by aging an ingot at 473 K in air for up to 40 days. After 20 days, the H_c and M_s were not only retained, but M_s actually slightly improved while H_c did not show significant change. After 40 days M_s was observed to decrease from the maximum at 20 days but was still significantly higher than the M_s in the original ingot.

It is also possible to consolidate from a τ phase powder precursor; however, consideration must be undertaken while avoiding decomposition of the magnetic phase into the γ_2 and β phases. One technique employed for this by Si *et al.* involved cold-compaction to preserve the τ phase in gas-atomized $(Mn_{54}Al_{46})_{97.56}C_{2.44}$ powder (1–7 μm) annealed at 760 K for 20 min [131]. The powder was then compacted into a cylinder at room temperature under a uniaxial compressive pressure of 3.1 GPa, which reduced the τ phase grain size to 10–100 nm. From the precursor powder to the bulk magnet M_s decreased by ~9%, from 99 to 90 Am^2/kg, while H_c increased from 135 to 271 kA/m. Therefore, cold compaction has been shown to be a suitable technique for increasing $(\mathbf{BH})_{max}$ by roughly doubling the H_c while minimizing the decomposition of the τ phase. Qian *et al.* also employed cold compaction as a way of increasing H_c, but at much higher pressure. Starting with pure Mn, Al, and C micropowders, they performed a solid-state reaction (SSR) at 1373 K for 10 h to alloy the pure powders into $Mn_{54}Al_{46}$ and $Mn_{53}Al_{45}C_2$ powders [199]. They then annealed the powders at 873 K for 5 min to form the τ phase. The powder had an average particle size of 50–100 μm and the grain size was refined by an undisclosed amount. Uniaxial compression under 12.5 GPa was shown to greatly improve the H_c of both the unalloyed (from ~40 to 310 kA/m) and carbon alloyed (from 54 to 175 kA/m) magnets while also greatly decreasing M_s for the unalloyed magnet (from ~88 to ~40 Am^2/kg) and slightly decreasing M_s for the carbon alloyed magnet (from 95 to 88 Am^2/kg). Therefore, like the results of Si *et al.*, this cold compaction technique greatly improved the H_c of the bulk compared to the powder while only reducing M_s by ~7% for the carbon-alloyed magnet. In fact, compared to Si *et al.* where H_c roughly doubled, this technique showed an improvement in H_c by more than a factor of 3. Yet, the H_c of the both the powder and the bulk produced by Si *et al.* were higher than the carbon alloyed powder and bulk synthesized by Qian *et al.* This suggests that the powder produced by Si *et al.*, whether due to the higher carbon concentration, or lower particle size, presents better magnetic characteristics than the powder produced by Qian by SSR. However, it also appears that increasing the cold compaction pressure results in improved H_c in the bulk compared to the powder by increasing the dislocation density and decreasing grain size. Interestingly, increasing the cold compaction pressure does not decrease M_s but actually appears to improve it compared to lower pressures. This is evidenced by the fact that under a pressure of 12.5 GPa, M_s decreased by 7 Am^2/kg (~7%), while under 3.1 GPa it decreased by 9 Am^2/kg (~9%). Si *et al.* also noted that given the same powder and preparation methods as the powder compacted

under 3.1 GPa, compaction under 1.6 GPa decreased M_s by 11 Am^2/kg (~11%). Therefore, increased pressure appears to stabilize the τ phase when compacting at room temperature.

Kinemuchi *et al.* demonstrated that using very high pressure also stabilizes the τ phase during hot compaction [99]. They heated a $Mn_{52}Al_{48}$ powder precursor of roughly equal γ_2 and β phases to 1273 K then held it under a uniaxial compression pressure of 5, 7, or 9 GPa for 1 h before furnace cooling -still under pressure- back to room temperature. 9 GPa produced a bulk magnet of roughly 90% τ phase with the remainder being γ_2 phase. Utilizing this technique at the lower pressure of 5 GPa retained the γ_2 and β phases and did not form any τ phase. They also tested different Mn-Al compositions and found that the τ phase formation was highly sensitive to the composition; under 9 GPa, the bulk magnet formed 100 wt.% β phase at $Mn_{62}Al_{48}$ and 100 wt.% γ_2 phase at $Mn_{41}Al_{59}$. Therefore, this provides evidence that at high applied pressures (7–9 GPa) the τ phase becomes energetically more favorable than the γ_2 and β phases for Mn_xAl_{1-x}, $47 < x < 55$.

Munoz-Rodriguez *et al.* directly compared hot pressing consolidation from a τ phase versus a ε phase powder precursor [111]. They prepared $(Mn_{57}Al_{43})_{98.9}C_{1.1}$ gas-atomized powder that was ~98% ε phase, and treated a portion of the ε phase powder to high energy ball milling (HEBM) for 60 s. Another portion of the gas-atomized powder was transformed into τ phase by annealing at 873 K for 30 min and a portion of the transformed powder was also subjected to HEBM for 60 s and then annealed at 698 K for 10 min. Each of these portions was then hot compacted at 873 K under 300 MPa. The ε phase powders were heat treated for 15 min without pressure to allow the phase transformation to occur then hot compacted for another 15 min. The τ phase powders were heat treated for 2 min then hot compacted for another 3 min to prevent phase decomposition. Comparing the bulk magnets produced by these methods, the $(\mathbf{BH})_{max}$ of the bulk magnet hot-compacted from gas-atomized ε phase powder was best, with a $(\mathbf{BH})_{max}$ of 12.4 kJ/m^3, $H_c = 228$ kA/m and $M_r = 44.3$ Am^2/kg. The other magnets produced each had slightly higher H_c, as high as 257 kA/m for the HEBM ε phase powder precursor ($M_r = 39.3$ Am^2/kg and $(\mathbf{BH})_{max} = 9.5$ kJ/m^3), but in each case this increase was accompanied by large phase fractions of the β phase and an Mn_3AlC carbide phase. As neither of these phases are ferromagnetic, they increased H_c by magnetically insulating the τ phase and serving as pinning sites, but they also lowered the M_r and decreased $(\mathbf{BH})_{max}$ for the other magnets to between 9.5 and 11 kJ/m^3. Therefore, this study demonstrated that for this Mn-Al-C composition the best bulk magnet is produced by the simultaneous phase transformation and hot compaction rather than performing the phase transformation step independently. The brief HEBM treatment was shown to increase H_c for each type of precursor, but in spite of its short duration did not retain adequate τ phase.

As in the case of Mn-Bi, SPS has the advantage over conventional sintering methods by preventing decomposition of the τ phase and avoiding excessive grain coarsening. Saravanan *et al.* performed SPS on a mixture of ball milled Mn and Al powders, in the atomic ratio Mn:Al 56:44, with a mean crystallite size of 40 nm [110]. The SPS was performed at 973 K, at a pressure of 75 MPa, for 5 min under vacuum. Since the precursor powder was an inhomogeneous mixture of Mn and Al phases there was no τ phase present prior to SPS. Due to the rapid nature of SPS, Al-rich γ_2 and Mn-rich β phases were the majority of the sintered magnet; there was inadequate time to homogenize the composition and thus only a small fraction of τ phase was able to form during the 5 min of sintering. The τ phase fraction was increased by annealing at 1100 K for 20 min to enter the ε phase region and thereby form a greater fraction of τ phase upon cooling. Unfortunately, even after annealing, the amount of τ phase present was still low, as indicated by a $M_{3MA/m}$ of only 28 Am^2/kg, although a large H_c of 194 kA/m was obtained. The SPS plus short annealing method was shown to prevent excessive grain coarsening but not to maximize the energy product. Therefore, improvements must be made to increase the τ phase fraction for Mn-Al magnets fabricated by SPS, perhaps by starting with a τ or ε phase powder precursor rather than elemental constituents. Such an improvement was made by Tyrman *et al.* by performing SPS on ε phase melt-spun ribbons that were cryo-milled to form a flake powder precursor [132]. The $Mn_{54}Al_{44}C_2$ alloys were sintered at 823 K under 400 MPa uniaxial compression to form 95 wt.% τ phase and 5 wt.% β phase. This demonstrates a significant improvement in τ phase fraction compared to Saravanan *et al.* mentioned above, likely due to a combination of the high ε phase fraction precursor powder and the C addition to minimize secondary phase formation. They observed anisotropic magnetization where M_s was greatest perpendicular to the axis of compression and H_c was greatest parallel to this axis. This was attributed to the flakes preferentially stacking with their long directions perpendicular to the axis of compression, shown in Fig. 17.

4.2.3. Mn-Al bulk processing with alloyants

Other alloyants than carbon have shown improvements in the magnetic properties of Mn-Al bulk magnets. Substituting 1.6 at.% Zn for Al in a $Mn_{54}Al_{44.4}Zn_{1.6}$ bulk magnet was shown by Wang *et al.* to stabilize the τ phase when annealing quenched-in ε phase at 693 K for 1 h [133]. A $Mn_{54}Al_{46}$ bulk magnet produced by the same method formed primarily β phase from quenched-in ε phase after the same 1 h heat treatment ($M_{1194\ kA/m} = <5$ Am^2/kg and $H_c = 119$ kA/m), therefore the addition of Zn was shown to greatly improve the τ phase fraction, increase M_s to ~70 Am^2/kg, and marginally improve H_c to 125 kA/m. It is possible that the fraction of larger Zn atoms sitting on the Al sites in the unit cell may have added some internal strain to the material, promoting the martensitic mode of the ε to τ phase transformation. However, at 1.6–5 at.% Zn concentrations, primarily β phase was formed during the quenching process, meaning that little τ phase was formed after heat treatment and the β phase was retained. The authors did not provide enough thermodynamic or microstructural analysis to determine why Zn improved the τ phase fraction. In concentrations up to 1 at.%, boron has been shown to increase both M_s and H_c of $Mn_{55}Al_{45}$ melt-spun ribbons [71]. This required annealing the as-spun ribbons to transform the quenched-in ε phase to τ. After annealing, the $M_{1.3MA/m}$ increased from 106 Am^2/kg to 117 Am^2/kg and H_c increased from 133 kA/m to 198 kA/m with the addition of 1 at.% boron. Boron concentrations above 1 at.% showed an increased presence of secondary phases in the as-spun ribbons, which decreased the amount of τ phase after annealing and therefore lowered M_s. The addition of boron was observed to lower the ε phase to τ transition temperature as well as the activation energy of the τ phase transformation from 188 kJ/mol to 181 kJ/mol. The *c*-axis lattice parameter was observed to decrease with the addition of boron, whereas the *c*/*a* ratio increased with additions up to 1 at.% B, but then decreased for higher concentrations. Increasing the *c*/*a* ratio has

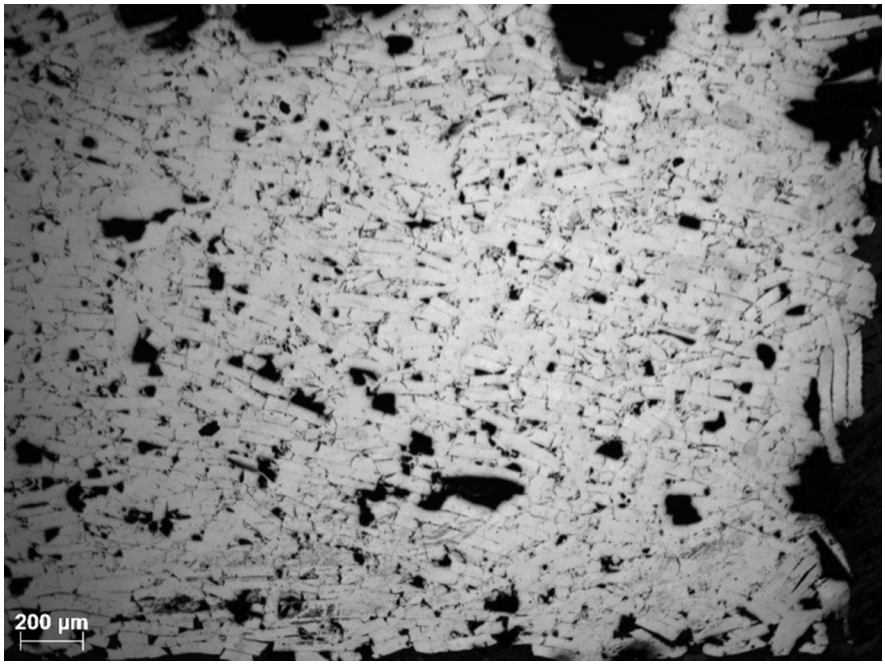

Fig. 17. SEM image of the preferential stacking of $Mn_{54}Al_{44}C_2$ flakes processed by SPS under 400 MPa. The flakes preferentially align perpendicularly to the vertical axis of compression. Redrawn and licensed under a Creative Commons Attribution (CC BY) license from [132].

been demonstrated to increase the magnetic moment of the Mn atom in Mn-Al. Therefore, by maximizing c/a at 1 at.% B, M_s was also maximized [72].

The drop-synthesis method of making a $(Mn_{55}Al_{45})_{99.98}B_{0.02}$ bulk magnet was less successful at forming large volume fractions of the τ phase. Unlike carbon, the addition of boron was observed to destabilize the τ phase at high temperatures, resulting in secondary phase formation during slow cooling from the melt [134]. These secondary phases increased H_c but at considerable expense to M_s. Boron-nitride (BN) has also been tested as a alloyant. Using arc-melting to prepare a $Mn_{52.9}Al_{45}B_{1.2}N_{0.9}$ ingot, Si *et al.* observed a slight increase in the ε phase to τ transition temperature, an opposite trend to what was observed for pure boron alloying noted earlier [135]. It also lowered T_C to 620 K, lower than unalloyed Mn-Al but higher than alloying with carbon. Subjecting the sample to severe plastic deformation under pressure, 10 high-pressure torsion turns under 6 GPa, increased H_c in the ingot from 64 kA/m to 430 kA/m but lowered $M_{1.6MA/m}$ from 116 Am^2/kg to 45 Am^2/kg from the as-cast material to the deformed, respectively. The plastic deformation produced a very fine grain size in the ingot but severely decomposed the τ phase. Subsequent aging at 623 K for 40 min recovered $M_{1.6MA/m}$ back to 77 Am^2/kg with a slight reduction in H_c to 406 kA/m.

Other metals have been tested as alloyants, such as Ni, Ti, V, Zr, and Tb. Ni alloying in a $Mn_{50}Al_{46}Ni_4$ bulk alloy, annealed at 743 K for 6 h before quenching, was shown by Mican *et al.* to slightly decrease T_C of the τ phase, from 645 to 634 K, compared to a $Mn_{54}Al_{46}$ alloy produced by the same method [136]. In this ingot, 20 wt.% of κ phase was observed. The soft magnetic κ phase has a CsCl structure and a lower Curie point than τ phase at 437 K. They reported that the Ni atoms are most likely to substitutionally occupy the Mn sites in the unit cell and in turn increase the occupancy by Mn on the Al site due to the excess Mn. In this configuration the magnetic moment contribution from the Ni atoms is relatively negligible. However, the Mn atoms in the Mn plane couple antiferromagnetically (AFM) with the Mn atom on the Al site, reducing the net magnetic moment. Therefore, alloying with Ni was observed to decrease M_s from 112 Am^2/kg ($Mn_{54}Al_{46}$) to 106 Am^2/kg ($Mn_{50}Al_{46}Ni_4$). Alloying with Ti was also carried out by the same procedure as for Ni, substituting atomic Mn for Ti [137]. Similar to Ni, alloying with 4 at.% Ti formed 19 wt.% κ phase which reduced H_c and M_r compared to the binary alloy. However, unlike Ni, the Ti atoms were shown to preferentially occupy the Al site and reduce the occupancy of this site by Mn atoms, reducing AFM coupling and actually improving the net magnetic moment per unit cell over the binary alloy. Additionally, T_C of the τ phase was shown to increase to 668 K for $Mn_{52}Al_{46}Ti_2$ and $Mn_{50}Al_{46}Ti_4$. However, increasing the amount of Ti decreased the amount of τ phase. Unalloyed, this processing method produced 75 wt.% τ phase. At 2 at.% Ti this decreased to 62 wt.% with the remainder forming γ_2 phase. At 4 at.% Ti the τ phase accounted for just 52 wt.%, with 29 wt.% γ_2 phase and 19 wt.% κ phase. Therefore, although Ti increased the net magnetic moment it suppressed formation of τ phase in favor of these other phases. Therefore, the addition of Ti was shown to decrease the AFM coupling due to excess Mn atoms but did not improve the overall magnetic performance other than T_C due to the formation of phases other than τ. Co-alloying with C and a small amount of Ni was shown by Feng *et al.* to increase the ε to τ phase transformation onset temperature from ~726 K in $Mn_{53}Al_{45}C_2$ to ~743 K in $(Mn_{53}Al_{45}C_2)_{99.4}Ni_{0.6}$ as well as improving the thermal stability of the τ phase [138]. They performed a stability test by holding the $Mn_{53}Al_{45}C_2$ and $(Mn_{53}Al_{45}C_2)_{99.4}Ni_{0.6}$ bulk magnets at 973 K for 7 days. Starting with approximately the same τ phase fraction ($M_{11MA/m}$ = ~120 $Am^2/$

kg), the $Mn_{53}Al_{45}C_2$ retained 35% its original τ phase volume fraction while $(Mn_{53}Al_{45}C_2)_{99.4}Ni_{0.6}$ retained 85%, clearly demonstrating that co-alloying with low levels of Ni can prevent τ phase thermal decomposition.

Geng *et al.* melt spun $Mn_{53}Al_{43}C_3Zr_1$ ribbons and annealed them at 773 K for 10 min before quenching [139]. The addition of 1 at.% Zr improved both H_c and M_s over the alloy $Mn_{54}Al_{43}C_3$ produced by the same method. M_s increased from 115 Am^2/kg to 128 Am^2/kg, despite the presence of a small fraction of ε and γ_2 phases, and H_c increased from 111 129 kA/m to 129 kA/m. However above 1.6 at.% the Zr was observed to prevent homogeneous τ phase formation and almost all the parent ε phase was retained after annealing. Thus, a small amount of Zr was shown to improve the magnetic properties of Mn-Al ribbons already alloyed with C but further research is needed to explain the exact mechanisms involved in the microstructure evolution. Alloying with V was shown by Xiang *et al.* to decrease the required cooling rate to directly synthesize τ phase in concentrations from 0 to 3 at.% V [140]. Consequently, melt spun $Mn_{55}Al_{45-x}V_x$ (x = 0–3) ribbons spun at 30 $m.s^{-1}$ were shown to form 100 wt.% ε phase in the x = 0–1 samples and the fraction of τ phase increased from 17.9 to 100 wt.% for x increasing from 1.5 to 3. The addition of V was also shown to increase the ε to τ phase transition temperature. Upon annealing the ribbons at 733 K for 30 min, M_s improved in all samples. However, only the 3 at.% V sample retained 100 wt.% τ phase; samples with a lower V concentration developed a lower τ phase fraction and more γ_2 and β phase fractions. Therefore, the addition of V was shown to improve the thermal stability of the τ phase. Additionally, the average grain size was decreased with the addition of V. However, the reduction in grain size did not offset the elimination of secondary phases, thus H_c was shown to decrease with added V while M_s was shown to increase. Alloying with Tb in $(Mn_{54}Al_{46})_{100-x}Tb_x$ (x = 0–1) melt-spun and annealed ribbons was observed to form Tb-rich nanoprecipitates along the grain boundary of the τ phase [141]. Increasing the Tb concentration increased the volume fraction of these precipitates, from ~3% to ~23%, as well as their size, from ~20 to ~140 nm as the Tb was increased from 0.2 to 1 at.%. The size of the τ phase grains was not affected by the Tb concentration. Optimum magnetic properties were observed at 0.2 at.% Tb. Comparing the unalloyed to the 0.2 at.% Tb sample, H_c increased from ~120 kA/m to ~160 kA/m while the (extrapolated) M_s decreased from 112 Am^2/kg to 111 Am^2/kg. This concentration maximized the magneto-crystalline anisotropy constant, from 1.5 in the binary alloy to 1.55 MJ/m^3, but the behavior of the Tb-rich precipitates indicates that the solubility of Tb in the τ phase matrix is limited above this value. Thus, 0.2 at.% Tb is able to significantly improve H_c of the bulk ribbons by forming Tb-rich nanoprecipitates but does not show any significant effect on the behavior of the τ phase.

Mix *et al.* demonstrated that substituting a small amount of Ga for Al can stabilize the alloy at high temperatures compared to binary MnAl [142]. They synthesized $Mn_{55}Al_{38.57}Ga_{6.34}$ and observed that both $L1_0$ MnAl and MnGa phases could coexist in the alloy. They first formed the MnAl $L1_0$ phase by heating for 48 h at 1373 K and then cooling at sufficient rate to form the τ phase. This however did not form the MnGa $L1_0$ phase. In order to achieve this, they further annealed for 24 h at 773 K to form the MnAl and MnGa phases. They compared the $Mn_{55}Al_{38.57}Ga_{6.43}$ sample to binary MnAl and MnGa samples produced through the same heat treatment. M_s of the ternary alloy (~125 Am^2/kg) was greater than those of either the MnAl (M_s = 113 Am^2/kg) or MnGa (M_s = 88 Am^2/kg) samples. They also tested the stability of the ternary alloy at high temperatures as compared to binary MnAl by annealing at 973 K for 14 days and observing the change in M_s from an initial value of 125 Am^2/kg to ~60 Am^2/kg after 7 days and to ~8 Am^2/kg after 14 days. They concluded that the ternary alloy displayed significantly better stability at this temperature than MnAl, and suggested that this ternary alloy may allow for higher temperature and time processing that is not possible in MnAl [143]. Comparing this with similar work undertaken by Zhao *et al.* [144], who examined substituting Al in $Mn_{55}Al_{45}$ with Ga as well as with Cu and Co, the following was observed. In terms of magneto-crystalline anisotropy constant, *K*, T_C, and M_s the addition of Cu and Co in place of Al was observed to decrease each of these key magnetic parameters. However, this was not the case for alloying with Ga in place of Al. For concentrations from 0 to 6 at.% Ga, they observed that T_C slightly increased from ~615 K to 627 K, M_s decreased slightly from 126 Am^2/kg to 117 Am^2/kg, and *K* increased from 1.76 MJ/m^3 to 1.88 MJ/m^3. This result was explained by the model shown in Fig. 18 where the Mn-Al alloy with excess Mn atoms is shown in the unit cell. The excess Mn atoms tend to occupy the Al site and couple antiferromagnetically with the atoms in the Mn plane. Due to their high number of valence electrons, the Cu and Co atoms sit in the Mn plane sites to allow them to hybridize with the Al atom. However, given the very similar density of states of Al and Ga, Ga tends to sit at the central site replacing an Al atom and forming $L1_0$ MnGa. Therefore, the alloying of Ga in turn manifests as $L1_0$ MnAl with a small transformed fraction of $L1_0$ MnGa. This prevents antiferromagnetic coupling due to Mn atoms in the central site and thus does not significantly diminish M_s in the same manner as Ni, Co, and Cu.

4.3. Mn-Al particulate processing

Particulate processing of Mn-Al is of considerable interest for improving the H_c of Mn-Al magnets and tuning the microstructure. The size of a single magnetic domain of Mn-Al has been reported as roughly 710 nm and 770 nm for Mn-Al-C, and H_c is improved when the grain size is reduced to this fine level [123,145]. As in the case of Mn-Ga and Mn-Bi, processes that reduce particle size such as milling must be carefully controlled to prevent excessive magnetic phase decomposition and oxidation.

Xiang *et al.* evaluated the effect of roller speed (from 0 to 10 $m.s^{-1}$) on the τ phase fraction of $Mn_{55}Al_{45}$ ribbons [146]. For 0 $m.s^{-1}$ (in water-cooled copper crucible rather than spun), 3 $m.s^{-1}$, and 5 $m.s^{-1}$ the wt.% of τ phase was 73, 83.4, and 100, respectively. The phase fractions of the γ_2 and β phases decreased proportionately. No γ_2 or β phase fractions were formed at higher roller speeds, but the ε phase was formed at the expense of τ phase due to the higher rate of cooling. For example, at 7 $m.s^{-1}$ the τ phase fraction was 66.2 wt.% (33.8 wt.% ε phase) and at 10 $m.s^{-1}$the τ phase fraction was 2.0 wt.% (98.0 wt.% ε phase). For roller speeds from 0 to 5 $m.s^{-1}$, both H_c and M_s increased with increasing wheel speed due to the increase in the amount of τ phase and decreasing grain size. However, at roller speeds >5 $m.s^{-1}$ less τ phase was formed, thus decreasing M_s, with the τ phase regions distributed in an untransformed ε phase matrix. This magnetically isolated the τ phase magnetic domains and increased H_c at wheel speeds from 5 to 10 $m.s^{-1}$. Higher wheel speeds, from 25 to 52 $m.s^{-1}$, have been used for either directly forming mixed phase ribbons of τ and ε [147], or for producing large volume

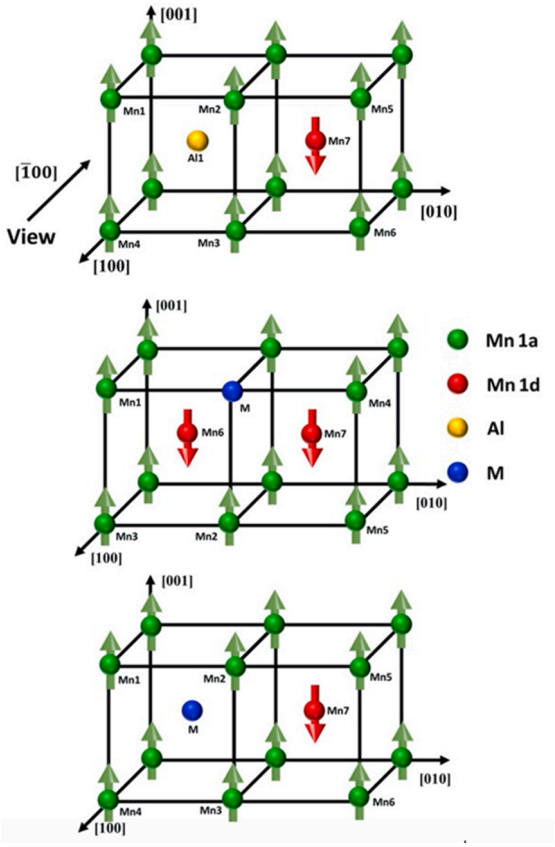

Fig. 18. The magnetic coupling effect of adding a substitutional alloyant atom, shown as M, to a manganese rich Mn-Al unit cell as detailed above. Mn atoms in the Al site couple antiferromagnetically with Mn atoms in the Mn-plane, reducing net magnetization. If the Co or Cu alloyant atom sits in the Mn plane (middle) then the AFM coupling is not improved. If the Ga atom (bottom) sits on the Al site, then AFM is mitigated. Reprinted figure with permission from [144]. Copyright 2021 by the American Physical Society.

fractions of the ε phase that could be subsequently annealed to transform to the τ phase [119,118].

Lu *et al.* investigated the effect of LEBM on melt-spun and annealed $Mn_{57}Al_{43}$ ribbons consisting of τ phase, with little to no secondary phases present [148]. To prevent oxidation, alcohol was introduced into the milling chamber. With milling durations from 0 (as-annealed) to 30 h, they observed the effect of milling duration on the average grain size, percent internal strain, long-range order parameter, H_c, and M_s (see Fig. 19). Any amount of LEBM was shown to diminish both M_s, indicating the decomposition of τ phase into secondary phases, and the order parameter, due to the mechanical introduction of defects in the crystalline structure. Similarly, LEBM was shown to decrease the grain size, with diminishing effectiveness at milling durations longer than 10 h. Milling times up to 23 h were shown to increase both the internal strain and H_c, as crystal defects served as domain wall pinning sites. However, at longer durations the strain and H_c were shown to then decrease, indicating that a strain relaxation process took place, but the cause of the relaxation was not investigated further. Simple mechanical grinding has also been shown to achieve similar results to ball milling, albeit with less control over the uniformity of particle size. For example, Wei *et al.* performed mechanical grinding on $Mn_{54}Al_{46}$ melt-spun ribbons, and Shao *et al.* did the same on $Mn_{54}Al_{46}$ strip-cast ribbons [86,109]. In the case of Wei, the as-cast ribbons were ground for 15 min then bonded in epoxy resin under a 796 kA/m applied field to form an anisotropic bonded powder composite: H_c increased to 294 kA/m while M_s was shown to decrease to ~111 Am^2/kg, although an exact comparison is difficult because the hysteresis curves reported use different maximum applied fields. Shao *et al.* mechanically ground the cast strips into a powder of <0.1 mm, but for an undisclosed amount of time and did not bond the powder in epoxy. The grinding process increased H_c from <80 kA/m to 223 kA/m, while reducing M_s substantially from 114 Am^2/kg to 64 Am^2/kg.

Trying to counteract the loss in magnetization observed during milling of the τ phase, other research has investigated milling the parent ε phase and then annealing to τ phase. Park *et al.* demonstrated the success of annealing milled powder on a $(Mn_{54}Al_{46})_{97.56}C_{2.44}$ alloy with LEBM for 96 h [149]. In this case they started with material consisting of ε phase that was retained during LEBM and then subsequently annealed at 753 to 873 K for 5 min in Ar. This technique thereby prevented the decomposition of the τ phase by waiting to perform the phase transformation anneal until after ball-milling. However, some decomposition of the ε phase into secondary phases was observed, preventing the formation of 100 wt.% τ phase and resulting in a low M_s. The sample annealed at 753 K had $H_c = 330.5$ kA/m and $M_{1.6MA/m} = \sim 28$ Am^2/kg, while the sample annealed at 873 K had $H_c = 372.0$ kA/m and $M_{1.6MA/m} = \sim 21$ Am^2/kg. As expected, the higher annealing temperature improved H_c but through the decomposition of τ phase into secondary phases. Compared

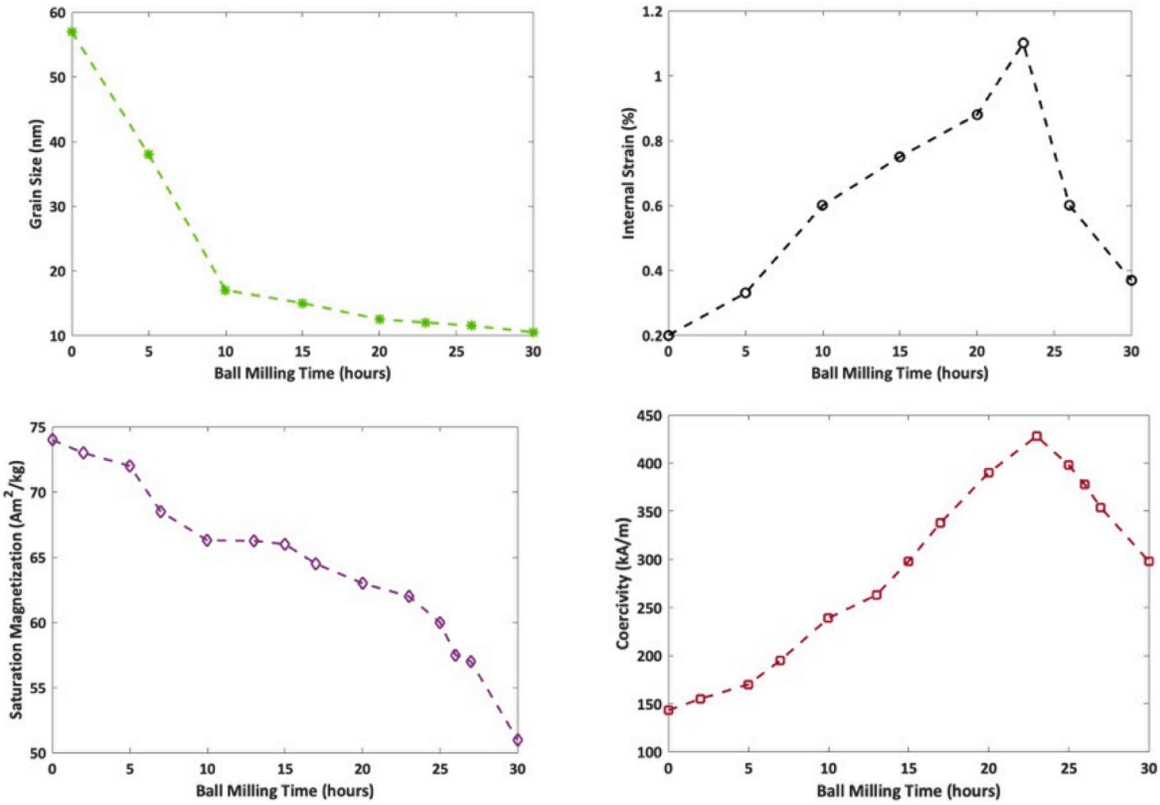

Fig. 19. The relationship between LEBM duration, grain size, internal strain, M_s, and H_c in $Mn_{57}Al_{43}$ melt-spun and annealed ribbons. Redrawn from [148].

to the aforementioned LEBM powder formed by Lu *et al.*, these powders showed worse H_c and less than half the saturation magnetization despite being annealed after milling. This is likely due to the decomposition of the ε phase during LEBM in the parent material, resulting in significant γ_2 and β fractions in the final annealed powder. Zeng *et al.* were more successful at milling the ε phase and transforming it into τ phase through a subsequent anneal [87,150,151]. Starting with a nano-grained ε phase powder precursor ($Mn_{50+x-y}Al_{50-x}C_y$, x = 0, 2, 4, 6, 8, y = 0, 1.7, 3), they ball milled the powder for 8 h then immediately performed heat treatment to transform the ε phase powder to τ phase. They observed that aging the as-milled ε phase powder at room temperature for five months caused it fully decompose into γ_2 and β phases, so immediate transformation into τ phase was necessary to achieve maximum magnetic properties. The best magnetic properties were achieved for a $Mn_{54}Al_{46}$ ball-milled powder that was then annealed at 673 K for 10 min (H_c = 382 kA/m, M_r = 45 Am^2/kg, $M_{4MA/m}$ = 89 Am^2/kg). The grain size of the as-milled ε phase powder at this composition was 8.2 nm, which increased to ~22 nm after annealing. They compared this to a bulk sample of identical composition and observed that the bulk magnet had a smaller ε to τ phase transformation enthalpy (ΔH = -11.7 J/g) and higher phase transformation peak temperature (783 K) compared to the powder magnet (ΔH = -87.2 J/g and 665 K). This explains why they observed partial decomposition of the annealed powder τ phase into γ_2 and β phases while the bulk sample annealed under identical conditions formed only τ phase: the milling process made the τ phase less stable at the annealing temperature, most likely due to the high defect density and small grain size of the powder. Adding carbon to the milled alloy was shown to improve the thermal stability of the τ phase but did not fully prevent the formation of secondary phases in the annealed magnet. They ball milled a $Mn_{51}Al_{46}C_3$ powder then annealed it at 773 K for 30 min, showing that the addition of carbon increased H_c but at the expense of magnetization (H_c = 414 kA/m, $M_{4MA/m}$ = ~49 Am^2/kg). Because the carbon concentration exceeded the reported solubility limit in this alloy (~1.7 at.%) [152], the increase in H_c was due to the formation of fine Mn_3AlC precipitates which served as pinning sites for domain wall motion.

Singh *et al.* showed that it is possible to combine multiple milling and annealing steps [153]. They compared an $Mn_{54}Al_{46}$ alloy produced by two different methods: route 1 (HEBM on the elemental powders, homogenizing, HEBM again, then annealing at 773 K for 50 min), and route 2 (arc-melted $Mn_{54}Al_{46}$, HEBM, homogenized, HEBM, and annealed at 773 K for 30 min). Route 1 produced close to 100 wt.% ε phase after homogenizing, while route 2 showed a significant portion of β phase. However, the final magnet produced by route 2 actually resulted in a higher τ phase content than route 1. In fact, the magnet formed by route 1 retained a large fraction of existing ε phase after annealing despite the longer annealing time. They concluded that the HEBM of the elemental powders prior to homogenizing in route 1 actually resulted in too high a defect density, which disrupted the ε to τ phase transformation and preferentially formed β phase. It is worth knowing therefore, whether it is best to mill the ε phase then anneal to τ phase or mill the already transformed τ phase and then recover the τ phase through a subsequent anneal. Lee *et al.* directly answered this question, starting with

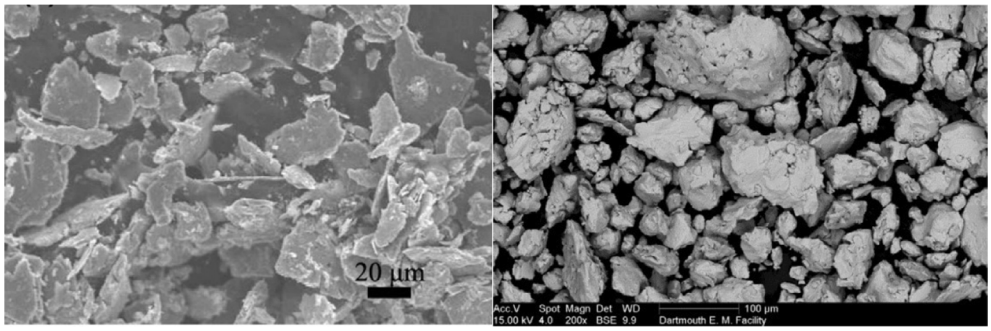

Fig. 20. SEM image of $Mn_{54}Al_{46}$ after SABM (left) and after conventional ball milling (right). Left from [156] right from [159]. Right image © IOP Publishing. Reproduced with permission. All rights reserved.

gas-atomized $Mn_{53}Al_{47}$ powder consisting of ε phase and processing it through two distinct procedures [154]. Procedure A took the ε phase powder and annealed it at 923 K for 20 min to form τ phase then ball milled the powder for from 5 to 26 h. Procedure B first ball milled the ε phase powder for 5–26 h then annealed it at 923 K for 20 min to transform into τ phase. In both cases the longer milling times resulted in higher H_c and decreased M_r. Comparing the two procedures, procedure B produced the higher H_c for all milling durations even though the internal strain and defect density due to milling was relatively equal between the two procedures. This is because procedure B showed much greater decomposition of the τ phase into the secondary phases as milling time was increased. Procedure A correspondingly always produced the higher M_r for all milling durations, thereby demonstrating that ball milling the τ phase preserves magnetization better than ball milling the ε phase and annealing. They then added an extra step to procedure A, an anneal at 553 K for 20 min to recover the magnetization lost during milling. Compared to procedure A, this recovery step was shown to increase M_r by roughly 10 Am^2/kg but slightly decrease H_c by 5–15 kA/m at all milling durations. A more detailed analysis of the microstructure is required to understand the mechanisms involved in the recovery process, but this study was sufficient to establish that the recovery in magnetization was greater than the loss in H_c Therefore, the magnet with the highest $(\mathbf{BH})_{max}$ in this study, 12.7 kJ/m^3 was produced by procedure A with a milling time of 5 h, followed by the recovery anneal. Jian *et al.* explored the effect of using a higher temperature recovery anneal after ball milling $Mn_{53.3}Al_{45}C_{1.7}$ τ phase powder for 1–12 h [155]. They saw the same general trend of decreasing magnetization and increasing H_c with increasing milling duration. However, they followed the ball milling with a recovery anneal at 773 K for 30 min. They observed that this heat treatment recovered the ordered structure of the τ phase, as evidenced by a higher M_s and M_r for the recovered samples compared to the milled samples for every duration. They saw some decomposition of the τ phase into γ_2 and β phases after recovery but not during milling, yet the recovered samples had lower H_c than the milled samples for every milling duration. Therefore, defects in the microstructure appear to be the dominant cause of domain-wall pinning in this case rather than pinning at regions of secondary phases. In concurrence with the conclusion of Lee *et al.*, the magnetization recovered through the post-milling anneal outweighed the loss in H_c in this study. The best $(\mathbf{BH})_{max}$ formed by milling the τ phase was 8.7 kJ/m^3, which was greatly improved to 16.3 kJ/m^3 after the recovery anneal.

Su *et al.* explored using SABM on Mn-Al with and without C alloying [61,156]. They reported that the surfactants used during SABM, oleic acid and oleylamine, chemically bonded to the surface of the milled particles and caused them to form flakes, a phenomenon that was not reported for conventional ball milling but is commonly observed in SABM (see Fig. 20) [157,158]. Like conventional milling, the average length and thickness of the flakes was shown to decrease with increasing milling time. They experimented with performing SABM on $Mn_{54}Al_{46}$ τ phase powder but observed that the magnetic phase was severely decomposed into secondary phases after just 2 h of SABM. Instead, they started with $Mn_{54}Al_{46}$ ε phase and performed SABM for 12 h followed by a 773 K recovery anneal for 30 min. This resulted in the best magnetic properties ($H_c = 234.9$ kA/m, $M_r = 32$ Am^2/kg, $M_s = 72$ Am^2/kg). Alloying with carbon was shown to greatly increase the stability of the τ phase during milling. Unlike the $Mn_{54}Al_{46}$ alloy, which decomposed from τ phase after just 2 h of SABM, the $Mn_{51}Al_{46}C_3$ alloy did not show significant decomposition after 12 h of SABM. The best magnetic properties for the alloyed material were found for $Mn_{51}Al_{46}C_3$ ε phase that was annealed at 773 K for 30 min then subjected to SABM for 4 h. This achieved a higher H_c than the unalloyed sample, at 266.2 kA/m, but at the expense of reduced magnetization, likely due to the formation of carbide precipitates similar to Zeng *et al.* They did not observe a correlation between the average flake size and the H_c but did observe kinks in the VSM curve, providing more evidence for inhomogeneous distribution of the magnetic τ phase and the presence of non-magnetic carbides. Interestingly, Liu *et al.* achieved nearly identical magnetic properties using 12 h of SABM on a $Mn_{51}Al_{46}C_3$ powder annealed at 823 K for 30 min ($H_c = 225$ kA/m, $M_r = 32$ Am^2/kg) as the $Mn_{54}Al_{46}$ powder reported by Su *et al.* above milled for the same 12 h duration but recovered at 773 K [24]. Therefore, because the carbon addition stabilizes the τ phase, higher temperature recovery anneals can be used to maximize M_r after milling.

Nguyen *et al.* investigated the effect of carbon concentration in Mn-Al-C magnetic powders [81]. They ball milled elemental Mn, Al, and C together for 10 h, then annealed at 1323 K for 1 h and quenched to form ε phase before a final 808 K anneal for 45 min to transform into the τ phase. This technique was used on four different compositions: $Mn_{55}Al_{45}$, $Mn_{55}Al_{44}C_1$, $Mn_{52.2}Al_{45.8}C_2$, and $Mn_{54.2}Al_{43.8}C_2$. For all compositions, increasing the carbon concentration improved H_c: from $H_c = 46$ kA/m for $Mn_{55}Al_{45}$ to 60 kA/m, 113 kA/m, and 143 kA/m for $Mn_{55}Al_{44}C_1$, $Mn_{52.2}Al_{45.8}C_2$, and $Mn_{54.2}Al_{43.8}C_2$, respectively. The addition of carbon was shown to decrease the average grain size, from 159 nm in the unalloyed powder to 79 nm in $Mn_{54.2}Al_{43.8}C_2$, and H_c was shown to increase

Table 8
Composition, method, and magnetic properties for selected τ phase Mn-Al particulate magnets.

Reference	Composition	Processing Technique	H_c *kA/m*	M_r Am^2/kg	M_s Am^2/kg (Saturating Field *kA/m*)	BH_{max} kJ/m^3	T_{curie} *K*
Chaturvedi *et al.* 2014 [159]	$Mn_{54}Al_{46}$	Gas atomized under Ar, ball milled for 20 h then 773 K anneal for 30 min	288		59.8 (796)		
	$Mn_{53}Al_{47}$	RSR spin-cast at 30,000 rpm under Ar, ball milled for 20 h then 673 K anneal for 30 min	215		35.2 (796)		
Fang *et al.* 2016 [162]	$Mn_{54}Al_{46}$	1673 K drop-synthesis for 10 min under Ar then ground into powder	124	20.7	88.0 (7162)		615
		" Then ball milled for 4 h	398	18.6	52.5 (7162)		
		" Then 773 K relaxation anneal for 1 h	342	26.5	75.5 (7162)		
	$(Mn_{55}Al_{45})_{98}C_2$	1673 K drop-synthesis for 10 min under Ar then ground into powder	53.5	15.2	111.1 (7162)		
		" Then ball milled for 4 h	319	16.8	50.6 (7162)		
		" Then 773 K relaxation anneal for 1 h	219	34.0	83.0 (7162)	56.5	
Fang *et al.* 2018 [163]	$(Mn_{55}Al_{45})_{98}C_2$	1673 K drop-synthesis for 10 min under Ar then ground into powder	32	23.2 *	118.2 (7162) *		
		" Then ball milled in liquid N_2 for 2 h	302	7.2 *	20.1 (7162) *		
		" Then flash heated at 1173 K for 1 min	183	15.6 *	47.8 (7162) *		
		" But flash heated at 1173 K for 5 min	95	25.7 *	104.3 (7162) *		
		1673 K drop-synthesis for 10 min under Ar then ground into powder, then ball milled in liquid N_2 for 4 h	176	1.3 *	5.7 (7162) *		
		" Then flash heated at 1173 K for 1 min	270	8.1 *	22.6 (7162) *		
		" But flash heated at 1173 K for 5 min	127	28.5 *	99.2 (7162) *		
Geng *et al.* 2015 [139]	$Mn_{53}Al_{43}C_3Zr_1$	Melt spun ribbons at 40 $m.s^{-1}$ in Ar then 773 K anneal for 10 min and water quench	129		128.0 (5570)		
Janotova *et al.* 2017 [94]	$Mn_{55}Al_{45}$	Melt spun ribbons then 673 K anneal for 1 h in vac	130.5			5.60	
		Melt spun then 713 K anneal for 1 h in vac	124.7			7.94	635
Jia *et al.* 2021 [158]	$(Mn_{54}Al_{46})_{97}C_3$	Melt-spun at 25 $m.s^{-1}$ then 773 K anneal for 12 min. Then HEBM in ethanol for 2 h followed by 723 K anneal for 10 min. Bonded in epoxy under 1600 kA/m	249 (‖)		75.5 (1200) (‖)		
Jian *et al.* 2015 [155]	$Mn_{53.3}Al_{45}C_{1.7}$	1373 K anneal for 24 h then water quench, 873 K anneal for 30 min, ball milled for 5 h, then 773 K anneal for 30 min		43.8			
		" Then bonded in paraffin wax under 796 kA/m	222.8 (‖)	54.8 (‖)		16.3 (‖)	
Kontos *et al.* 2019 [134]	$(Mn_{55}Al_{45})_{99.98}B_{0.02}$	Drop-synthesized at 1673 K for 10 min in Ar then 1273 K anneal for 10 min and water quench. Then ball-milled for 2 h	~270		~58 (1440)		
		" Then 723 K anneal for 30 min	~345		~48 (1440)		
		Initial bulk treatment then ball milled for 10 h	~130		~68(1440)		
		" Then 723 K anneal for 30 min	~250		~60 (1440)		
Law *et al.* 2017 [200]	$Mn_{54}Al_{46}$	Gas atomized under Ar, then 628 K anneal for 10 min in N_2	143	0.3	1.9 (1592)		
		" But 648 K anneal for 10 min	139	~3	~7 (1592)		
		Gas atomized under Ar, ball milled for 3 min then 628 K anneal for 10 min in N	389.9	12.9	2.6 (1592)		
		" But 648 K anneal for 10 min	~374	~16	~27 (1592)		
Lee *et al.* 2011 [154]	$Mn_{53}Al_{47}$	Gas atomized under N, 923 K anneal for 20 min, ball milling for 5 h under Ar, then 553 K anneal for 20 min	247	41.2	~60 (796)	12.7	
Liu *et al.* [24]	$Mn_{53.3}Al_{45}C_{1.7}$	Melt-spun at 40 $m.s^{-1}$, 927 K anneal for 10 min	123	46 *	127 *	12.2	
Lu *et al.* 2016 [148]	$Mn_{57}Al_{43}$	Melt-spun under Ar, 683 K anneal for 30 min	~143		~74 (1552)		
		" Then low energy ball milling for 23 h	422		62 (1552)		
Madugundo *et al.* 2016 [128]	$Mn_{53.5}Al_{44.5}C_2$	1373 K homogenization anneal then quench, 823 K anneal for 20 min, crushed before high energy ball milling for 2 h, then again 823 K anneal for 20 min	310	28	53 (2387)		
Marshall *et al.* 2016 [147]	$Mn_{54}Al_{46}$	Melt-spun ribbons at 31 $m.s^{-1}$ in Ar	80	15.9	39.4 (1592)		
	$Mn_{54}Al_{46}$	Melt-spun ribbons at 31 $m.s^{-1}$ in Ar. Then cryo-milled for 8 h	218.8	24.0	50.8 (1592)		
		" Then cryo-milled for 10 h	231	18.4	38.9 (1592)		
Nguyen *et al.* 2018 [81]	$Mn_{55}Al_{45}$	Ball milled for 10 h, 1323 K anneal for 1 h under vas and water quench, then 773 K anneal for 45 min	46	44*	101 (5570)*	4.0	
	$Mn_{55}Al_{44}C_1$	" But 798 K anneal for 45 min	60	37*	85 (5570)*	2.8	
	$Mn_{52.2}Al_{45.8}C_2$	" But 798 K anneal for 45 min	113	42*	96 (5570)*	5.0	
	$Mn_{54.2}Al_{43.8}C_2$	" But 808 K anneal for 45 min	143	49*	110 (5570)*	7.8	
Obi *et al.* 2014 [82]	$Mn_{53}Al_{46}C_1$	Ball milling for 6 h, 1173 K anneal for 1 h under Ar	159	28	54 (796)	3.2	
		Ball milling for 6 h, 1173 K anneal for 1 h under N	199	11	20 (796)	0.8	
		Ball milling for 6 h, 1173 K anneal for 1 h under vac.	159	27	53 (796)	3.2	

(*continued on next page*)

Table 8 (*continued*)

Reference	Composition	Processing Technique	H_c *kA/m*	M_r Am^2/kg	M_s Am^2/kg (Saturating Field *kA/m*)	BH_{max} kJ/m^3	T_{curie} *K*
Oygarden *et al.* 2019 [164]	$(Mn_{55}Al_{45})_{98}C_2$	Ball milled for 10 h, compressed into 7 mm dia. pellet under 260 MPa, 1323 K anneal for 20 min and air quench. Then cryo-milled in liquid N_2 for 5 min	231	21.4 *	43 (1592) *		
		" Then 748 K anneal for 1 h	~239		47 (1592) *		
Park 2018 *et al.* [149]	$(Mn_{54}Al_{46})_{97.56}C_{2.44}$	1423 K anneal for 24 h then water quench, crushed, ball milled for 96 h, 753 K anneal for 5 min in Ar	330.5		~28 (1592)		
		" But 873 K anneal for 5 min in Ar	372.0		~21 (1592)		
Qian *et al.* 2018 [78]	$Mn_{54}Al_{46}$	1373 K anneal for 10 h in vac then water quench, crushed, 755 K anneal for 20 min, then NaCl-assisted ball milling for 100 min and magnetically separated	191	35	102 (5570)		635
	$(Mn_{54}Al_{46})_{99.5}Si_{0.5}$	'	358	33	70.3 (5570)		644
	$(Mn_{54}Al_{46})_{99}Si_1$	'	294	16	60.1 (5570)		673
	$(Mn_{54}Al_{46})_{99}Fe_1$	'	334	32.5	75.7 (5570)		680
Qian *et al.* 2019	$Mn_{54}Al_{46}$	Start as powder, 1373 K homogenization anneal for 10 h, then 873 K anneal for 5 min under Ar and H	~40		~88 (3183)		
	$Mn_{53}Al_{45}C_2$	"	64		95 (3183)		
Rial *et al.* 2018	$Mn_{54}Al_{46}$	Gas-atomized then 723 K anneal for 10 min under flowing N	127	28.4	63.7 (1592)		
		Gas-atomized, steel- ball milled for 90 s, 698 K anneal for 10 min under flowing N	167	29.1	58.7 (1592)		
		" But steel-ball milled for 270 s, 673 K anneal for 10 min under flowing N	223	28.6	53.2 (1592)		
		" But Tungsten-C ball milled for 90 s, 648 K anneal for 10 min under flowing N	342	20.2	34.2 (1592)		
		" But Tungsten-C ball milled for 270 s, 648 K anneal for 10 min under flowing N	382	17.8	30.3 (1592)		
Rial *et al.* 2020	$Mn_{54}Al_{46}$	Gas-atomized, then 628 K anneal for 10 min under flowing N	143	~1	~2 (1592)		
		Gas-atomized, Tungsten-C ball milled for 30 s, then 628 K anneal for 10 min under flowing N	334	~12	~22 (1592)		
Saito *et al.* 2005 [169]	$Mn_{53}Al_{44.8}C_{1.7}Ni_{0.5}$	Crushed, sieved, high energy ball milled for 100 h, then wrapped in Ta foil, 1173 K anneal for 1 h in Ar and water quench	155	60	104 (1194)	11.4	
		Gas-atomized and annealed at 873 K for 1 h in Ar	107	60		9.0	
Shao *et al.* 2017	$Mn_{54}Al_{46}$	Strip cast into 2.5 × 0.5 mm strip. Then ground into powder of <0.1 mm	223		63.9 (5570)		
Si *et al.* 2019 [118]	$Mn_{54}Al_{46}$	Melt spun ribbons at 52 $m.s^{-1}$ then 758 K anneal for 5 min	151	25	78 (6366)		
	$Mn_{54}Al_{46}C_{2.44}$	"	104	30	122 (6366)		
Si *et al.* 2019	$Mn_{54}Al_{46}C_{2.44}$	Gas-atomized powder, 60 K anneal for 20 min	135	33	91 (3183)		
Singh *et al.* 2015	$Mn_{54}Al_{46}$	HEBM for 5 h in Ar, 1423 K anneal for 5 h and water quench, then HEBM for 2 h and 773 K anneal for 30 min	143	~4.2			638
Su *et al.* 2016 [156]	$Mn_{54}Al_{46}$	1423 K anneal for 16 h and water quench, then SABM for 12 h and 773 K anneal for 30 min	234.9	32	72		
Su *et al.* 2019 [168]	$(Mn_{50}Al_{46}Cu_4)_{97}C_3$	1373 K anneal for 16 h in Ar, crushed, and SABM for 9 h, bonded in epoxy resin under 239 kA/m	207.6 (⊥)	23 (‖)			
Wei *et al.* 2014 [86]	$Mn_{54}Al_{46}$	Melt-spun ribbons at 15 $m.s^{-1}$ under Ar, 723 K anneal for 45 min in Ar, then mechanical grinding for 15 min, and bonded in epoxy under 796 kA/m	294	72.6 *	~111 (1592)*	24.7	648
Xiang *et al.* 2018 [71]	$Mn_{54.45}Al_{44.55}B_1$	Melt-spun ribbons under Ar, 733 K anneal for 30 min under vac	198		127 (3979)	44	
Xiang *et al.* 2019 [146]	$Mn_{55}Al_{45}$	Melt-spun ribbons at 3 $m.s^{-1}$ in Ar	86.7		87.6 (1353)		
		Melt-spun ribbons at 5 $m.s^{-1}$ in Ar	120.2		105.2 (1353) 118.2 (3979)		
		Melt-spun ribbons at 10 $m.s^{-1}$ in Ar	144.0		2.1 (1353)		
Xiang *et al.* 2020 [140]	$Mn_{53.35}Al_{43.65}V_3$	Melt-spun ribbons at 30 $m.s^{-1}$ in Ar, 733 K anneal for 30 min under vac	82.0		105.8 (1353) and 120.5 (3979)		
Zeng *et al.* 2007 [87,150,151]	$Mn_{54}Al_{46}$	1423 K homogenization anneal for 20 h and water quench, crushed, ball milled for 8 h under Ar, then 673 K anneal for 10 min, bonded in epoxy	382	45	89 (3979)		655
	$Mn_{51}Al_{46}C_3$	" But 773 K anneal for 30 min, bonded in epoxy	414		~49 (3979)		
Zhao *et al.* 2019 [141]	$(Mn_{54}Al_{46})_{98.8}Tb_{0.2}$	Melt-spun ribbons at 25 $m.s^{-1}$, 773 K anneal for 20 min, crushed, then high-energy ball milled for 2 h	432		~31 (3979)		

Note: Magnetic properties are at room temperature and isotropic unless otherwise noted.
* Moment is converted from emu/cm^3 or kA/m using a density of 5200 kg/m^3 for τ phase.
(⊥) Indicates measurement perpendicular to direction of magnetic alignment during annealing or bonding.
(‖) Indicates measurement parallel to direction of magnetic alignment during annealing or bonding.
~ Indicates a value determined from a graph rather than taken in text.

linearly with decreasing grain size. However, magnetization was only shown to improve for $Mn_{54.2}Al_{43.8}C_2$ ($M_s = 110$ Am^2/kg, 99 wt.% τ phase, $(\mathbf{BH})_{max} = 7.8$ kJ/m^3) compared to the unalloyed powder ($M_s = 101$ Am^2/kg, 92 wt.% τ phase, $(\mathbf{BH})_{max} = 4.0$ kJ/m^3). This is due to the competing effects of carbon alloying: increasing the stability of the τ phase, forming non-magnetic carbide precipitates, reducing T_C, and affecting the net magnetic moment of each Mn atom by changing the dimensions and occupancy of the unit cell [81,84-87]. All these factors must be taken into account to understand the effect of C alloying. The unalloyed powder showed 92 wt.% τ phase, roughly equal to the $Mn_{52.2}Al_{45.8}C_2$ powder at 91 wt.% τ, while the $Mn_{55}Al_{44}C_1$ powder was 88 wt.% τ. Therefore, the evidence shows that M_s did not vary proportionately with τ phase fraction, as shown in Table 8. Further experimentation is needed to elucidate the exact microstructural mechanisms causing magnetization to vary with carbon addition in this study. Curiously, Obi *et al.* saw no improvement of τ phase fraction or M_s with the addition of carbon from 0 to 1.5 at.%. However, this appears to be a result of their processing technique rather than the addition of carbon alone. They produced $Mn_{53}Al_{47-x}C_x$ (x = 0–1.5) powders by ball milling elemental powders for 6 h then annealing at 1173 K for 1 h and slowly cooling to form the τ phase. However, related research has shown while the addition of C prevents the decomposition of existing τ phase into secondary phases, it raises the ε to τ phase transition onset temperature [87,160,161]. The fraction of τ phase formed by cooling from ε phase is also highly sensitive to the cooling rate [91]. Therefore, the technique of slowly cooling ε to τ phase rather than quenching (as was performed by Nguyen *et al.*) likely requires an optimized cooling rate for each amount of C alloyant, rather than using the same cooling rate for each composition. For C concentrations from 0 to 1 at.% they observed that grain size was refined, H_c increased, and τ phase fraction decreased from 76 to 55 wt.%. However, at 1.5 at.% carbon alloying the τ phase content decreased to 20 wt.% and the majority phase fractions were ε and Mn_3AlC with γ_2 and β phases making up the remainder. This indicates that the addition of carbon combined with the cooling rate they used in this technique favored formation of non-magnetic phases rather than τ. Therefore, more experimentation is required to understand what cooling rates are required to maximize the τ phase produced by this method. They also demonstrated that the atmosphere in which $Mn_{53}Al_{46}C_1$ powders are annealed can greatly affect the magnetization. They tested annealing this powder at 1173 K for 1 h in argon gas, nitrogen gas, and vacuum environments. H_c was invariant between Ar and vacuum (159 kA/m), while in N_2 it was highest (199 kA/m). Annealing in Ar produced the highest M_s of 54 Am^2/kg, followed by vacuum and N, at 53 Am^2/kg and 20 Am^2/kg, respectively. The increased H_c and decreased M_s in the N_2 atmosphere was due to decreased grain size (25 nm), the formation of a significant fraction of γ_2 and β phases (57 wt.% combined), as well as the formation of non-magnetic nitride compounds (~20 wt.%), which served as pinning sites for magnetic domain walls. Interestingly, the formation of carbides was greatly suppressed in the N_2 atmosphere. No decisive difference between Ar and vacuum environments was shown except for a smaller average grain size (31 nm in Ar versus 46 nm in vacuum).

Chaturvedi *et al.* tested the effect of ball milling different types of precursor powders [159]. They tested $Mn_{54}Al_{46}$ precursors produced by gas-atomization (GA) and $Mn_{53}Al_{47}$ precursors produced rapid solidification rate processing (RSR). The GA powder was atomized from melt using Ar gas, then ball milled for 20 h and annealed at 773 K for 30 min. The RSR powder was formed by pouring molten $Mn_{53}Al_{47}$ onto the face of a disk rotating at 30,000 rpm, then the powder was ball milled for 20 h and annealed at 673 K for 30 min. The particle size of the GA powder was from <20–45 μm and consisted of ~66% ε phase with the remainder being γ_2 and β phases. The particle morphology was spherical and no τ phase was in the GA powder prior to ball milling. They sieved the ranges of particles and observed that the larger particles, 38–45 μm, had much higher ε phase fraction than smaller particles. This, they concluded, was due to the smaller particles moving away from the gas stream by Brownian motion, resulting in slower cooling of the finer particles in the thermally insulative argon atmosphere. Therefore, larger particles are preferred for improving the fraction of ε phase. The powder produced by RSR had >90% ε phase but a wide distribution of particle sizes, from <90–300 μm. Similar to the GA powder, the particles were spherical, no τ phase was observed in the RSR powder, and the amount of γ_2 and β phases (<10%) decreased for larger particle sizes. A wheel rate of<30,000 rpm would produce larger particles and therefore improve the ε phase fraction. Milling for 20 h reduced the average grain size to 12 nm for the GA powder and 45 nm for the RSR powder. The primary phase after milling was the ε phase in both cases. Annealing for 30 min was performed at the optimized temperatures of 773 K for GA and 673 K for RSR to transform into τ phase. Despite having a lower fraction of ε phase in the precursor, the resulting GA magnetic powder had better H_c (288 kA/m) and $M_{796kA/m}$ (59.8 Am^2/kg) than the RSR powder ($H_c = 215$ kA/m and $M_{796kA/m} = 35.2$ Am^2/kg). Therefore, the fraction of τ phase in the final GA powder was actually greater than the RSR. They were unable to determine the reason for this, but it is likely that the RSR ε phase powder was less resilient to decomposition during milling; conceivably the fraction of ε phase after milling was actually lower in the RSR powder than in the GA and a shorter milling time was necessary to preserve the RSR ε phase. Further analysis is needed to conclusively determine why the GA powder had worse magnetic properties. Both samples had significant secondary phase fractions, so the improved H_c is likely due to the finer grain size of the GA powder.

Milling at cryogenic temperatures (cryo-milling) offers one solution to preventing phase decomposition. In fact, Marshall *et al.* demonstrated that the strain imparted during cryo-milling can actually induce the ε to τ phase transformation without annealing and the low temperature prevents the diffusional decomposition into secondary phases [147]. Their precursor was pulverized melt-spun ribbons consisting of a mix of ε and τ phases. They performed cryo-milling on the ribbons at liquid nitrogen temperatures, using 0.25 wt.% oleic acid to assist the milling, for 6–10 h. They observed that compared to the as-cast ribbons, the M_s and H_c both increased with milling time. The increase in H_c from milling was due to the increase in τ phase, increased defect density, and refined grain size (reduced from ~140 nm to ~ 40 nm after 10 h). Unlike milling at room temperature however, no decomposition into secondary phases was observed. Rather, the strain induced by milling was shown to drive the displacive shear transformation from ε to τ phase, as evidenced by the increased M_s and τ phase fraction as the milling time increased from 6 to 8 h. However, after 10 h, the M_s and long-range ordering parameter were shown to decrease without decomposition of the τ phase into secondary phases. This suggests that the milling strain after 10 h caused widespread chemical disordering of the $L1_0$ structure, causing AFM coupling rather than FM between Mn atoms and reducing overall net magnetization. It is also worth noting that even after cryo-milling for 8 h to achieve the best

magnetic properties (H_c = 218.8 kA/m and $M_{1.6MA/m}$ = 50.8 Am^2/kg), a significant fraction of ε phase was retained and not transformed. This appears to align with the theory of a hybrid martensitic-massive ε to τ phase transformation. The diffusional massive transformation mechanism would be discouraged at low temperatures and so a complete transformation to τ phase would be impossible by cryo-milling alone. However, cryo-milling demonstrates a reliable way to prevent decomposition of either the ε or τ phases during milling and could perhaps be combined with a subsequent heat treatment to complete the transformation into the magnetic phase.

In the case of milling the already transformed τ phase, cryo-milling is shown to help prevent the decomposition of the τ phase into secondary phases while still imparting strain and defects into the structure. However, this does not necessarily mean that the magnetization of a cryo-milled sample will be greater than a sample milled for the same duration at room temperature. In fact, Fang *et al.* showed that this is not the case, by combining cryo-milling of the τ phase with subsequent annealing and comparing this to milling at room temperature and annealing [162,163]. The precursor ingot was formed from melt at 1673 K, held for 10 min, then cooled to room temperature in roughly 10 min. The ingot was ground into a powder to allow it to be milled. As shown in the Table 8, the process of cooling from the melt produced an as-cast ingot consisting of primarily τ phase, as shown by the high M_s value. Some secondary γ_2 and β phases were present but no ε phase was observed. Thus, milling was carried out on the magnetic τ phase of powder samples of composition $(Mn_{55}Al_{45})_{98}C_2$ at room and liquid nitrogen temperatures. The precursor for room-temperature milling had M_s = 111 Am^2/kg and H_c = 54 kA/m. The precursor for cryo-milling had M_s = 118 Am^2/kg and H_c = 32 kA/m. The variability between the two is due to the variability of the cooling rate when directly forming τ phase from melt. Ball milling for 4 h reduced M_s to 51 Am^2/kg and increased H_c to 319 kA/m whereas cryo-milling for 4 h reduced M_s to 6 Am^2/kg, a drastic reduction in magnetization, and increased H_c to 302 kA/m. In both cases the increase in H_c is roughly the same, but the cryo-milled sample clearly suffered from a greater loss in magnetization. This was caused by widespread chemical disordering of the $L1_0$ structure in the cryo-milled sample. A 773 K recovery anneal was performed on the ball-milled sample for 1 h, raising M_s to 83 Am^2/kg and lowering H_c to 219 kA/m, consisting of ~70 wt.% τ phase and ~30 wt.% β phase. This recovered M_s to ~75% of its original value before milling while improving H_c by ~400%. Similarly, a rapid 1173 K anneal for 5 min was undertaken on the cryo-milled sample. This recovered powder, which was ~90 wt.% τ phase and <10 wt.% γ_2 phase, displayed a M_s = 99 Am^2/kg and H_c = 127 kA/m. This represents a recovery of M_s to ~84% of its original value before milling while also improving H_c by ~400% and preventing the significant decomposition into secondary phases. Therefore, while cryo-milling actually showed greater disordering of the $L1_0$ structure than room temperature ball milling, it was ultimately shown that it was possible to recover more magnetization while improving H_c by the same factor using cryo-milling and rapid annealing above 1173 K to reorder the Mn and Al atoms sitting on incorrect sites within the lattice. Related research by Oygarden *et al.* tried cryo-milling on powder that had already undergone conventional ball milling and recovery annealing (referred to as "as-synthesized") as a way to further enhance H_c [164]. In this case, the as-synthesized material (M_s = 86 Am^2/kg and H_c = 119 kA/m) was greatly affected by just 1–7 min of cryo-milling, but no decomposition into secondary phases was observed. After 5 min of cryo-milling the H_c roughly doubled to 231 kA/m and M_s was reduced in half to 43 Am^2/kg. To recover some magnetization, they annealed at 748 K for 1 h, which gave M_s = 47 Am^2/kg and H_c = 239 kA/m. However, during this anneal they observed significant phase decomposition into γ_2 and β phases, primarily β phase (40 wt.%), and retention of only 55 wt.% τ phase. In this way, the magnetization recovered by reordering the τ phase was largely offset by the decomposition into secondary phases. These phases then can act as domain wall pinning sites, hence the slight improvement in H_c overall despite relaxing the strain induced by cryo-milling. Therefore, an optimized anneal technique must be developed for maximizing the benefits of cryo-milling, and this result shows that the rapid high temperature anneal by Fang *et al.* is more effective than the longer low-temperature anneal described here.

The type of milling media can affect the magnetic properties of the milled powder, as demonstrated by Rial *et al.*[165]. They compared using steel and tungsten carbide balls to perform SABM using oleic acid. The vials in which the milling took place were made of the same material as the balls. Using a gas atomized ε phase $Mn_{54}Al_{46}$ powder precursor, they performed short duration milling for either 90 s or 270 s for each of the media types. They observed that milling with steel did not induce any phase change from the gas-atomized precursor but did reduce the average grain size from 100 nm to 30 nm and 15 nm, for 90 s and 270 s respectively. By contrast, milling with tungsten carbide for 90 s partially transformed the ε phase into τ, and milling for 270 s increased the transformed fraction. This was due to the greater amount of energy imparted by the tungsten carbide balls compared to the steel ones. Given that tungsten carbide is roughly twice the density of steel (15,800 versus 7,600 kg/m^3), they used a model of inelastic collisions between the balls and powder to show that the kinetic energy transferred to the powder from each collision with a ball is approximately double for tungsten carbide compared to steel. Therefore, this additional energy enabled the phase transformation to occur. In keeping with the findings of Zeng *et al.*, they observed that the microstructural changes brought about by milling lowered the onset temperature of the ε to τ transformation from 688 K in the gas-atomized powder to 648 K and 642 K for steel milling for 90 s and 270 s respectively [87]. Milling with tungsten carbide reduced the transformation temperature to 641 K for both milling times. Reducing the tungsten carbide milling time down to 30 s was also shown to form τ phase [166]. They attempted to achieve high H_c and magnetization by annealing the milled powders at optimized temperatures for 10 min under flowing N_2: the magnetic properties are shown in Table 8. They observed that annealing the powders at 628–698 K did achieved a high H_c in the tungsten carbide milled samples due to the imparted strain and grain refinement (H_c = 334 kA/m, 342 kA/m, and 382 kA/m for 30 s, 90 s, and 270 s, respectively) but with poor magnetization ($M_{1.6MA/m}$ = 22 Am^2/kg, 34.2 Am^2/kg, and 30.3 Am^2/kg for 30 s, 90 s, and 270 s, respectively). They attributed this drop in M_s largely to the formation of β phase during annealing from the disordered milled material. However, as shown by Obi *et al*. [82] annealing in flowing N_2 may also promote the formation of non-magnetic nitride phases after milling which would also improve H_c at the cost of magnetization. Additionally, Jia *et al.* identified that there is also a significant difference between "wet" milling in an ethanol environment compared to "dry" milling in Ar [158]. They compared both wet and dry HEBM on an $(Mn_{54}Al_{46})_{97}C_3$ 100 wt.% τ phase precursor ($M_{1.2MA/m}$ = 73 Am^2/kg, H_c = 250 kA/m) for 2 h followed by a recovery anneal at 723 K for 10 min and bonding in

epoxy under an applied field. After wet HEBM and annealing the τ phase was reduced to ~83 wt.% ($M_{1.2MA/m}$ = 75.5 Am^2/kg, H_c = 249 kA/m) while the dry HEBM was reduced to ~65 wt.% ($M_{1.2MA/m}$ = 34.2 Am^2/kg, H_c = 123 kA/m), the remainder had decomposed into β phase. Therefore, the wet HEBM was demonstrated to reduce the decomposition of τ phase into β phase while still imparting a high density of dislocations to improve H_c. Furthermore, the morphology of the dry milled particles was roughly isotropic and 20 μm in diameter, while the wet milled particles were flakes ~4 μm thick and ~55 μm across, similar to results from SABM milling mentioned previously. They calculated that the wet milled flakes had a magnetic texture (as defined in the bulk section) of degree 0.37, compared to the dry milled particles at 0.253. Combining this with electron diffraction patterns they concluded that a degree of *c*-axis crystal texture is developed in the thin flakes as a result of the wet milling.

Similar to what was reported for bulk magnets, powder Mn-Al has been alloyed with other elements in addition to C, including Dy, Pr, Cu, Ni, Si, and Fe. The rare-earth elements, Dy and Pr, were co-alloyed with C in $Mn_{52.3}Al_{45}C_{1.7}Dy_1$ and $Mn_{52.3}Al_{45}C_{1.7}Pr_1$ by Liu *et al.* in melt-spun ribbons spun at 40 $m.s^{-1}$ [24]. The ribbons were then annealed at 927 K for 10 min. Compared to $Mn_{53.3}Al_{45}C_{1.7}$ (H_c = 123 kA/m, M_r = 46 Am^2/kg, M_s = 127 Am^2/kg) prepared by the same method, the addition of the co-alloyants increased the ε to τ phase transformation temperature from 781 K in the $Mn_{53.3}Al_{45}C_{1.7}$ sample to 805 K and 808 K for additions of 1 at.% Dy and Pr, respectively. The substitution of 1 at.% Pr for Mn was reported to increase M_r, M_s, and $(\mathbf{BH})_{max}$ but exact values were not given. Additionally, the substitution of 1 at.% Dy for Mn was reported to improve H_c but at the expense of M_r and M_s, but again exact values were not given. Therefore, it is not possible to quantify the improvement of magnetic properties with the co-alloying of C with Pr and Dy without further data.

As mentioned in the Mn-Al Bulk Processing section, the addition of Cu alone does not benefit the magnetic properties and has been shown to promote the decomposition of the magnetic phase into β phase [167]. However, co-alloying with Cu and C has been shown to prevent decomposition of the τ phase, but more research is needed to show if co-alloying is significantly more beneficial to the magnetic properties than alloying with C alone [61,156,167,168]. Saito *et al.* compared 100 h ball milled and 1173 K annealed powders of composition $Mn_{53}Al_{44.8}C_{1.7}Ni_{0.5}$ with $Mn_{53}Al_{45}C_2$ powders prepared by the same method [169]. The addition of Ni was shown to increase M_s from ~68 Am^2/kg in the $Mn_{53}Al_{45}C_2$ powder to 104 Am^2/kg for $Mn_{53}Al_{44.8}C_{1.7}Ni_{0.5}$. This is a contrast to the results of Mican *et al.* referenced in the bulk section, who saw a decrease in magnetic moment with the addition of 4 at.% Ni [136]. However, in that case, the Ni was substituted for Mn in the alloy whereas in this case the Mn concentration was held constant and Ni was substituted for Al and C. Additionally, the level of alloying here is much lower, at only 0.5 at.%. They observed that this small amount of Ni alloying in substitution for Al did not significantly diminish the magnetization and actually may promote the ε to τ phase transformation. The $Mn_{53}Al_{45}C_2$ powder exhibited a higher H_c than $Mn_{53}Al_{44.8}C_{1.7}Ni_{0.5}$ (203 and 155 kA/m, respectively) but this study did not conclude the microstructural cause. More analysis is needed to understand the complete effect of co-alloying with low levels of Ni and C. Finally, alloying with Si or Fe was explored by Qian *et al.* on $(Mn_{54}Al_{46})_{100-x}D_x$ (D is the alloyant) powders that had undergone annealing into τ phase and then salt-assisted ball milling for 100 min. The final milled powder was magnetically separated to remove non-magnetic particles. Morphologically, the unalloyed and Si-alloyed milled powders were composed of thin flakes, of ~0.3 and ~0.7 μm in diameter, respectively. The Fe-alloyed powder, by contrast, took the form of much larger spherical particles of ~10–90 μm in diameter. They concluded that this was due to the Fe alloyed sample's improved ductility over the other samples, making it more resilient to the collisions of the milling process. The addition of Si at 0.5 and 1 at.% increased T_C from 635 K in the unalloyed powder to 644 K and 673 K, respectively. Alloying with 1 at.% Fe showed an even greater increase of T_C to 680 K. Fe also lowered the onset temperature of the hybrid martensitic-massive ε to τ phase transformation relative to the unalloyed sample, from 700 K to 628 K, yet it also significantly increased the temperature at which the transformation was complete. Whereas Si increased the phase transformation onset temperature to 771 K and 781 K for 0.5 and 1 at.% Si, respectively. Therefore, Fe is shown to lower the activation energy of the phase transformation but also slows the rate of transformation. Si, by contrast, increases the activation energy of the transformation while also slightly slowing the rate of transformation, but to a lesser degree than Fe. As shown in Table 8 below, alloying with either element improved H_c over the unalloyed powder but lowered M_s. Alloying with Fe resulted in a τ phase powder, whereas increasing the amount of Si alloyant was shown to promote the formation of a significant fraction of γ_2 and β phases. This is likely a result of Si raising the activation energy for the ε to τ phase transformation, making the secondary phases more energetically favorable. Interestingly though, the H_c did not trend with increasing fraction of secondary phases; $(Mn_{54}Al_{46})_{99.5}Si_{0.5}$ (358 kA/m) had a higher H_c than $(Mn_{54}Al_{46})_{99}Si_1$ (294 kA/m) despite having more τ phase and less γ_2 and β. Furthermore, $(Mn_{54}Al_{46})_{99}Fe_1$ (334 kA/m) showed little to no secondary phases, yet had a reasonably large H_c. This suggests that other factors, such as grain size and defect density, were the primary contributors to H_c in these powders. Characterization of the microstructure is needed to confirm this and to uncover the source of the improved ductility in the Fe-alloyed powder. M_s did trend with the fraction of secondary phases, with the Si-alloyed powders showing the lowest M_s (60.1 Am^2/kg and 70.3 Am^2/kg for 0.5 and 1 at.%, respectively). The addition of 1 at.% Fe lowered M_s from 102 Am^2/kg in the unalloyed powder to 75.7 Am^2/kg, despite having a high τ phase content. This may be due to the changes in phase transformation kinetics, where Fe is shown to slow the rate of transformation to τ, meaning that the alloyed powder may have had a less ordered $L1_0$ structure and lower magnetization under the annealing conditions prior to milling. It is unclear whether this is the result of changes to the magnetization of the Mn atoms in the unit cell due to the presence of Fe, as research in thin films suggests that 1 at.% Fe substitution for Mn will actually slightly improve M_s overall in a $Mn_{55}Al_{45}$ alloy [170], whereas modeling at 0–0.5 at.% Fe suggests that Fe substitution for Mn will reduce M_s in equi-atomic MnAl [171].

4.4. Mn-Al thin film processing

The complex formation mechanism and thermal instability of τ phase has made it difficult to optimize processing conditions for Mn-Al thin films. However, they show great potential for achieving higher anisotropy and H_c than is possible in bulk samples (See

Table 9
Composition, method, and magnetic properties for selected τ phase Mn-Al thin film magnets.

Reference	Composition	Processing Technique	H_c *kA/m*	M_r *Am^2/kg*	M_s *Am^2/kg* (Saturating Field *kA/m*)	BH_{max} *kJ/m^3*	T_{curie} *K*
Hosoda *et al.* 2012 [173]	$Mn_{54.1}Al_{45.9}$	Sputter deposition onto (0 0 1) MgO/Cr substrate at 473 K under Ar and capped with Ta then 723 K anneal			115 (1592) (⊥) *		
Huang *et al.* 1995 [172]	$Mn_{50}Al_{50}$	0.8 μm film RF sputter deposited onto glass substrate at 303 K under Ar then 683 K anneal for 30 min in vac	239 (⊥) and (‖)		80.8 (796) (‖) *		
Mao *et al.* 2020 [177]	$Mn_{55}Al_{45}$	Molecular beam epitaxy onto (0 0 1) GaAs substrate of 0.8 nm Co_2MnSi buffer at 523 K then 30 nm Mn-Al film at 623 K and capped with Pt	~240 (⊥)		85 (4775) (⊥) *		
Navio *et al.* 2018 [176]	$Mn_{50}Al_{50}$	2 nm thick film of alternating layers deposited by molecular beam epitaxy onto (0 0 1) GaAs substrate at 373 K under Ar and capped with Ta. Then 673 K anneal	653 (⊥)		71.2 (3183) (⊥)*		
		2.3 nm thick film of alternating layers deposited by molecular beam epitaxy onto (0 0 1) GaAs substrate at 523 K under Ar and capped with Ta	279 (⊥)		121 (3183) (⊥)*		
Sato *et al.* 2016 [170]	$(Mn_{97.5}Fe_{2.5})_{55}Al_{45}$	UHV-magnetron sputter deposition onto (1 0 0) MgO substrate with Cr buffer at 773 K, 723 K anneal for 1 h, then capped with Cr	302 (⊥)		77 (2547) (⊥)*	16 (⊥)	
	$Mn_{55}Al_{45}$	"	326 (⊥)		69 (2547) (⊥)*	9.6 (⊥)	
Takata *et al.* 2018 [174]	$Mn_{50}Al_{50}$	15 nm thin film deposited by molecular beam epitaxy onto (0 0 1) MgO substrate at 473 K, then capped with Ta, then 573 K anneal for a few seconds under vac	~20		69.2 (3183) *		
		15 nm thin film deposited by molecular beam epitaxy onto (0 0 1) MgO substrate at 423 K with a 5 nm (0 0 1) Mn_4N buffer, then capped with Ta	318 (⊥)		82.7 (3183) (⊥)*		
		" But onto (0 0 1) $SrTiO_3$ substrate	557 (⊥)		63.5 (3183) (⊥) *		
You *et al.* 2018 [178]	$Mn_{50}Al_{50}$	65 nm DC magnetron sputter-deposition onto (0 0 1) MgO substrate at 773 K. Then 4 nm Co layer added by PEALD	219 (⊥)	44 (⊥) *	52 (1194) (⊥)*	26.6 (⊥)	

Note: Magnetic properties are at room temperature and isotropic unless otherwise noted.
* Moment is converted from emu/cm^3 or kA/m using a density of 5200 kg/m^3 for τ phase.
(⊥) Indicates measurement perpendicular to thin film surface, or out-of-plane.
(‖) Indicates measurement parallel to thin film surface, or in-plane.
~ Indicates a value determined from a graph rather than taken in text.

Tables 7 and 9). Early research by Huang *et al.* demonstrated that $Mn_{50}Al_{50}$ thin films could be fabricated to produce almost 100 wt.% τ phase [172]. They performed radio-frequency (RF) magnetron sputtering onto a glass substrate at 303 K under Ar to form ~100 wt.% ε phase. Raising the temperature of the glass substrate above 303 K, to 373 K and 473 K, decreased the formation of ε phase in favor of an amorphous structure. Therefore, a room temperature substrate is shown to quench the sputter deposited Mn-Al film more rapidly, increasing the crystallinity of the ε phase. Annealing the 303 K sputtered film at 683 K for 30 min under vacuum transformed the ε phase into τ with little to no secondary phases present, indicating a full transformation of the ε phase without decomposition of the τ. However, the 373 and 374 K substrate sputtered films showed lower crystallinity and increasing presence of the γ_2 phase. Thus, the poor crystallinity of the higher temperature substrate films carried over after annealing, forming poorly ordered and partially decomposed τ phase. However, it is worth noting that the easy *c*-axis of the τ phase preferentially formed perpendicularly to the surface of the film for the higher temperature substrates, whereas the 303 K substrate showed a preferential orientation of the τ phase at ~37.9° to the film surface. Optimum magnetic properties for this synthesis technique were obtained for a film thickness of 0.58 μm, a 303 K substrate temperature and a 683 K anneal for 30 min ($H_c = 239$ kA/m, $M_{796kA/m} = 80.8$ Am^2/kg parallel to film plane). M_s was not significantly affected by film thickness, but H_c did not exceed 151 kA/m for films thinner than 0.5 μm. H_c also decreased slightly for increasing film thickness up to 0.8 μm. They concluded that the primary contribution to H_c arose from the induced stress between the rigid amorphous glass substrate and the thin film during the transformation to τ phase, producing stress fields that could inhibit domain wall motion.

The interaction between the thin film and substrate therefore plays a key role in tuning the magnetic properties of the thin film. Hosoda *et al.* fabricated $Mn_{54.1}Al_{45.9}$ thin films by magnetron sputtering onto a (0 0 1) MgO substrate at room temperature to 773 K in Ar [173]. Between the substrate and Mn-Al film they layered a 40 nm Cr buffer layer to minimize crystal lattice mismatch between the film and substrate. The Cr layer also provided a much flatter surface for film deposition than the MgO single crystal. They capped the film with 5 nm of Ta to prevent oxidation and annealed the as-deposited sample at 573–873 K to complete formation of the τ phase. As noted by Huang *et al.* the magnetic anisotropy of the as-deposited film was dependent on the substrate temperature. The room temperature substrate showed a preferred magnetization parallel to the film surface, an orientation which was unchanged after annealing.

On the other hand, the substrates at 573 K or higher showed preferred magnetization of the as-deposited film perpendicular to the surface and again the orientation was the same after annealing. However, for the 473 K substrate they concluded that it was possible to tune the magnetic anisotropy of the *c*-axis by varying the annealing temperature. The as-deposited film was magnetized parallel to the film surface but annealing at 723 K or 773 K changed the preferred magnetization to perpendicular. Therefore, this demonstrates that the easy-axis magnetic alignment can be manipulated by modifying the annealing temperature, allowing for both perpendicular and parallel aligned magnetic films. However, a deeper understanding of the mechanism responsible for the alignment is needed to optimize this technique.

Sato *et al.* explored the effect of introducing alloyants into the Mn-Al layers [170]. Like Hosoda *et al.*, they used magnetron sputtering onto a (0 0 1) MgO substrate with a 10 nm Cr buffer layer. They substituted Co, Cu, Fe, and Ni alloyants (D) for Mn, forming $(Mn_{100-x}D_x)_{55}Al_{45}$ (x = 1–10 at.%) thin films. The as-deposited films were annealed at 723 K for 1 h to form the τ phase, and all showed magnetic anisotropy perpendicular to the film surface. Alloying with Cu and Co from 1 to 10 at.% caused the preferential formation of an "unknown" phase at the expense of the τ phase. This unknown phase was also observed in the Ni-alloyed film at levels of 2.5–10 at.% and Fe-alloyed films at levels of 5–10 at.%. The authors were unable to identify this phase but concluded that since its structure was the same for all alloyants it must be a Mn-Al or a Mn phase formed from the decomposition of τ. Therefore, any improvement to the magnetic moment of the Mn atoms in the τ phase lattice or reduction in AFM Mn coupling can be undermined by the decomposition of the magnetic τ phase. Alloying with up to 2.5 at.% Ni or Fe showed a slight improvement in M_s over the unalloyed film, but this improvement was reversed at higher alloying levels. Thus, a complete analysis of this "unknown" phase is essential to maximizing the benefits of these alloyants. The addition of Co, Cu, Fe, or Ni was shown to lower H_c as they were observed to distort the tetragonality of the τ phase and thus likely lower the magneto-crystalline anisotropy. The optimum magnetic film was obtained for $(Mn_{97.5}Fe_{2.5})_{55}Al_{45}$, which showed a $(\mathbf{BH})_{max}$ of 16 kJ/m^3 (H_c = 302, $M_{2.6MA/m}$ = 77 Am^2/kg) compared to the unalloyed film prepared by the same method of $(\mathbf{BH})_{max}$ = 9.6 kJ/m^3 (H_c = 326, $M_{2.6MA/m}$ = 69 Am^2/kg) despite a decrease in H_c

Takata *et al.* examined the effect of different substrates on Mn-Al films deposited by molecular beam epitaxy (MBE), comparing substrates of (0 0 1) MgO, (0 0 1) $MgAl_2O_4$, and (0 0 1) $SrTiO_3$ [174]. They tested these substrates alone and with a buffer layer of Mn_4N, which is softly FM on its own [175]. They were unable to form τ phase directly on the $MgAl_2O_4$ or $SrTiO_3$ substrates using MBE. However, τ phase was successfully formed on the MgO substrate at 473 K, albeit with a poor H_c (~20 kA/m) and magnetically isotropic behavior. Analysis of the crystal structure of the τ phase showed that on the (0 0 1) MgO substrate its unit cell was distorted to be more cubic than in bulk samples, lacking the tetragonality that gives it high magnetic anisotropy. The addition of a smooth 5 nm (0 0 1) Mn_4N buffer layer deposited at 423 K allowed for anisotropic tetragonal τ phase formation on not just the MgO substrate but also $SrTiO_3$. This was attributed to the excellent lattice matching between Mn_4N and τ phase Mn-Al. The resulting τ phase was highly magnetically anisotropic, aligning its easy axis preferentially perpendicular to the thin film, and displayed a much higher H_c of 318 kA/m and 557 kA/m for the buffered MgO and $SrTiO_3$ substrates, respectively. They also observed no kinks in the VSM curves that would indicate competing magnetization behavior between the τ phase and FM Mn_4N. Therefore, the magnetically hard τ phase and soft Mn_4N effectively exchange coupled, and the addition of the Mn_4N buffer layer improved magnetic performance overall compared to the unbuffered substrates.

Mn-Al films have also been grown by MBE on a GaAs substrate, but the magnetic properties can be affected by the formation of a Mn-Ga-As-Al layer at the interface. This behavior was observed by Navio *et al.* when depositing alternating Mn and Al layers on a (0 0 1) GaAs substrate at 373–523 K using MBE [176]. By this method a soft magnetic Mn-Ga-As-Al phase developed which strongly affected the magnetic hysteresis behavior (see Fig. 21). The clear kinks in the hysteresis curve demonstrate that the Mn-Ga-As-Al do not efficiently exchange-couple, and the magnetization reversal behavior is thus not uniform with the applied field. The overall magnetic performance is actually quite good, for both the sample deposited at 373 K and annealed at 673 K (2 nm thick, H_c = 653, $M_{3.2MA/m}$ = 71.2 Am^2/kg, shown in Fig. 21) and the sample deposited at 523 K without a subsequent anneal (2.3 nm thick, H_c = 279, $M_{3.2MA/m}$ = 121 Am^2/kg), with a strong magnetic anisotropy perpendicular to the film surface in both cases. However, the non-uniform reversal behavior is not desirable in most permanent magnet applications, and therefore adding a buffer layer has been explored to fix this problem. Mao *et al.* added a 0.8 nm single-crystal Co_2MnSi buffer layer on top of the (0 0 1) GaAs substrate at 523 K before depositing a 30 nm $Mn_{55}Al_{45}$ film at 623 K and capping with Pt [177]. Adding the buffer layer was shown to greatly decrease the root-mean square surface roughness of the thin film from 1.66 nm to 0.2 nm, drastically improve the magnetic anisotropy, and roughly doubling M_s to 85 Am^2/kg by improving the crystallinity of the τ phase with a reduction in H_c. from ~400 kA/m to ~240 kA/m. No kinks or non-uniform reversal behavior were observed with the addition of this buffer. It is also possible to use the exchange-coupling effect to improve M_s of the Mn-Al thin film by selecting an appropriate soft magnet capping material. You *et al.* improved the M_s of a 65 nm $Mn_{50}Al_{50}$ thin film deposited by magnetron sputtering onto a (0 0 1) MgO substrate at 773 K by capping it with a thin layer of Co using plasma enhanced atomic layer deposition (PEALD) at 423 K [178]. They tested Co layers of 2 nm, 4 nm, and 6 nm thicknesses. M_s was shown to increase with increasing Co thickness, owing to the high M_s of elemental Co, but similarly H_c decreased with the addition of the soft magnetic material [179]. All the thin films displayed magnetic anisotropy perpendicular to the film surface. The 2 nm and 4 nm Co capped films showed smooth reversal behavior, but the 6 nm capped film showed a kink in the reversal, suggesting that at this thickness the exchange-coupling behavior began to break down between the MnAl and Co layers. This is a logical outcome by simply depositing the Co layer on top of the MnAl film; as the Co layer thickness increases the FM interaction between the MnAl and Co domains takes place over a greater distance. Thus, the domains in the Co layer farthest from the MnAl film can decouple magnetically and start to behave independent of the MnAl domains. Further research may see some benefit therefore to layering the Co film in between layers of MnAl to maximize the exchange-coupling effect.

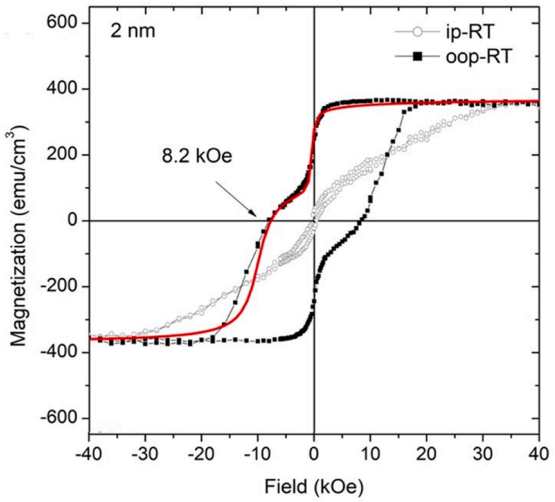

Fig. 21. The non-uniform magnetic reversal behavior of a 2 nm thick $Mn_{50}Al_{50}$ thin film deposited on (0 0 1) GaAs by MBE. The kinks in the curve reflect the presence of a soft magnetic Mn-Ga-As-Al phase which reverses at a lower applied field than the hard magnetic τ phase. The anisotropy is aligned out-of-plane (oop) or perpendicular to the film surface (ip). Licensed under a Creative Commons Attribution (CC BY) license from [176].

5. Comparison of permanent magnets and opportunities

Currently, none of the Mn-based permanent magnet materials have been processed to achieve their theoretical $(\mathbf{BH})_{max}$. Using Mn-based magnets as a replacement for RE magnets requires them to offer an equivalent or lower cost for similar performance (cost per $(\mathbf{BH})_{max}$ in dollars per kJ/m^3) as those currently in use. As shown in Fig. 22 (top), the experimental values of $(\mathbf{BH})_{max}$ for MnGa and Mn_3Ga are far from their theoretical maximum values. As such, they cannot yet be considered as serious candidates for most applications. However, it is also apparent from Fig. 22 (bottom) that Mn-Bi and Mn-Al have been shown experimentally to offer a lower cost per $(\mathbf{BH})_{max}$ than Sm-Co magnets. Furthermore, as shown by the arrows in Fig. 22, Mn-Al could offer the same cost per $(\mathbf{BH})_{max}$ as Nd-Fe-B currently in use if the theoretical $(\mathbf{BH})_{max}$ could be achieved. Keeping in mind the uncertain future of commodity prices and global mining, any large changes in the price of RE elements will only further the economic justification for Mn-Al and Mn-Bi magnets. Therefore, research should not overlook the many opportunities for Mn-based magnets in various applications.

Mn-Ga alloys have drawn interest for memory storage applications, such as for spin-transfer-torque magnetic random-access memory (STT-MRAM). This is because the M_s can be controlled by varying the Mn content, and thin films can be formed with high magneto-crystalline anisotropy perpendicular to the film surface, both desirable features for this application [19]. Applications in magnetic sensors have also been proposed [27]. Therefore, further research into methods to reliably tune H_c and M_s of Mn-Ga magnets remains essential for scaling up their production to levels of conventional manufacturing. As shown in Fig. 22, Mn-Ga magnets on their own are unlikely to be cost competitive with conventional RE magnets for bulk applications. Yet, composite exchange-coupled permanent magnets of hard magnetic Mn-Ga coupled with a soft magnetic material such as Fe or Fe-Co, could mitigate the costs and make higher $(\mathbf{BH})_{max}$ Mn-Ga magnets possible [186]. This requires nanocrystalline control of the grain structure of the magnet, so further research into scalable production and microstructure control strategies will be useful for identifying whether this is possible with Mn-Ga [187]. Additionally, further exploration into alloying elements is needed to understand how the magnetic properties may be improved by ternary element additions, with an emphasis placed on elements which can be substituted for Ga to reduce the cost.

While Bi, at $7.50/kg, does not face the same economic hurdle as Ga for applications in bulk magnets, it does face the problem of rarity in the earth's crust (8.5×10^{-7}%) and as such it is primarily produced as a by-product of mining for other metals such as tungsten [4]. However, the ability to form thin films with tunable anisotropy and very high H_c make Mn-Bi appealing for magneto-optical and spintronic applications [36]. Furthermore, the aforementioned positive H_c temperature coefficient of LTP MnBi make it suitable for high temperature applications such as energy conversion. However, due to the line phase nature of the LTP, further research is needed to optimize preparation methods to prevent decomposition of the LTP during mechanical stress and thermal processing. Replacing some Bi with Mg and Sb has shown great potential for improving the thermal stability of the LTP and HTP [42]. Further research is also needed to fully characterize the QHTP and explore optimum processing routes for applications at low temperatures where it shows the most promise [31]. Novel analysis techniques such as first-order reversal curves (FORCs) are one promising technique to better understand inter-domain interactions in Mn-Bi magnets [65]. Additionally, small-angle neutron scattering (SANS) has shown potential as a method for determining the effects of microstructural defects in bulk Mn-Bi, by measuring the misalignment of magnetization around such defects [188]. Finally, techniques to form Mn-Bi exchange coupled composite magnets with additions of nanostructured soft-magnetic Fe and Co of up to 10 at.% have shown preliminary success at increasing M_s in bulk samples, albeit at the expense of H_c and $(\mathbf{BH})_{max}$ [189]. Therefore, further research is needed to optimize processing conditions for exchange coupled Mn-Bi magnets.

Of the Mn-based magnets discussed in this review, Mn-Al permanent magnets by far show the most promise to fill the property gap between inexpensive low-performance ferrites and expensive high-performance RE magnets due to the abundance and low cost of Al.

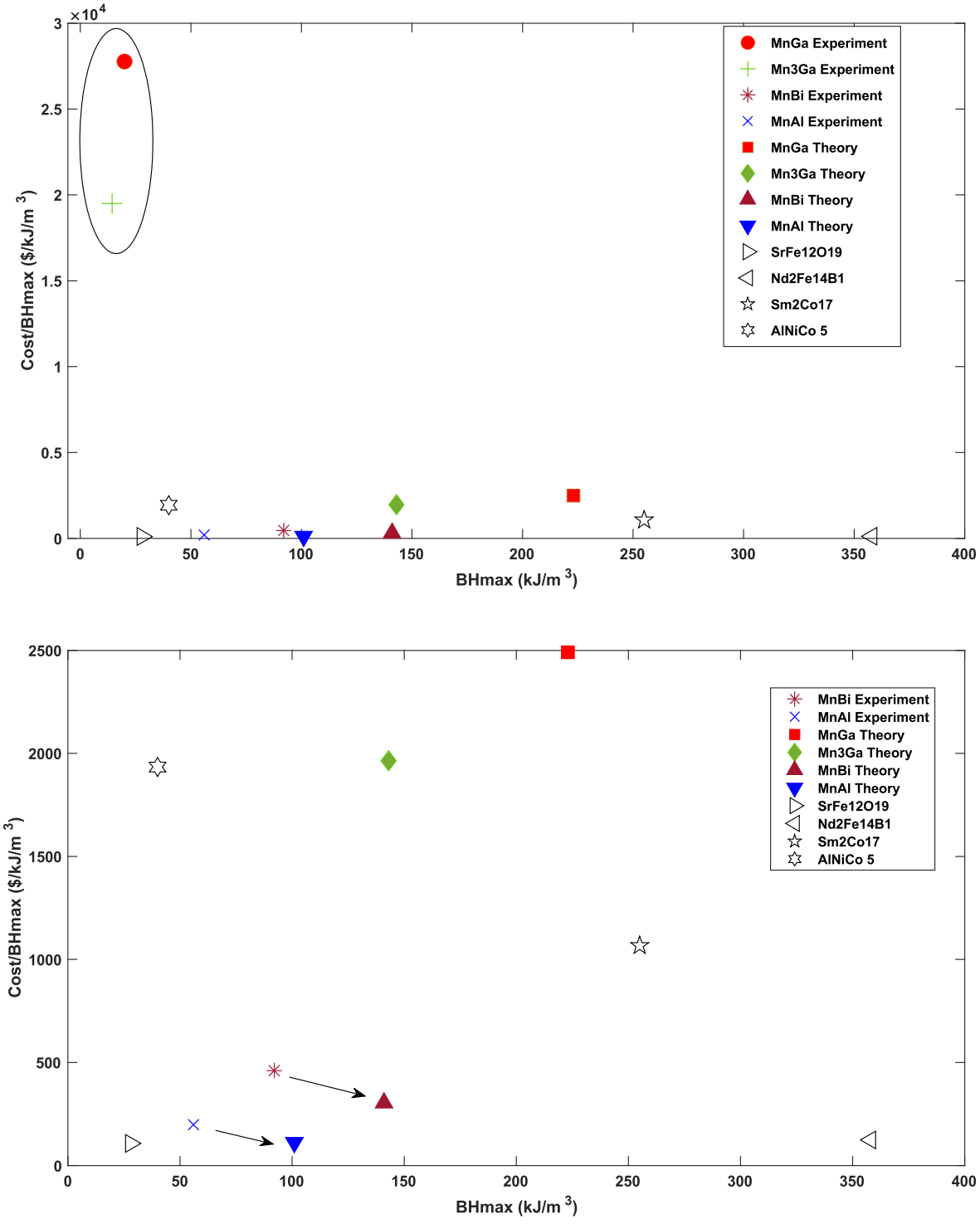

Fig. 22. A comparison of the permanent magnets discussed in this review showing the tradeoff between material cost and performance at room temperature for both the experimental and theoretical (**BH**)max values. Note the high raw material cost and low experimental (**BH**)max values for MnGa and Mn_3Ga enclosed by the ellipse (top), and the same properties with the enclosed points removed (bottom). The arrows (bottom) demonstrate the projected improvement for Mn-Bi and Mn-Al if experimental performance can meet theoretical predictions. All costs are $USD. Data from [1,4,180-185].

This makes them encouraging candidates for large-scale adoption into permanent magnet motors and generators. As shown in this review, methods to improve H_c have typically come at the expense of reduced M_s. Further research is needed to understand how different crystal defects could improve the H_c while minimizing their impact on M_s. Likewise, the phase transformation behavior of the hybrid massive-martensitic τ phase is still not completely understood; a more complete understanding is essential to optimize processing conditions in an informed manner. Furthermore, it is necessary to better understand the processing conditions that form defects such as twins, APBs, and dislocations as well as their effect on magnetic characteristics. Additional research into alloying elements and how they can improve τ phase stability during mechanical stress and thermal processing is also needed. Techniques such as laser-bed fusion sintering and electron beam sintering show some promise as novel ways to consolidate particulates into bulk magnets of complex shapes, but further research is needed to demonstrate how these methods can improve upon more conventional processing methods [190,191]. Similarly, plasma arc deposition (PAD) has shown preliminary success at forming Mn-Al-C nanoparticles by vaporizing a cast ingot in an Ar-H_2 environment but the different vapor pressures between Mn and Al means that the composition of the nanoparticles varies drastically from the starting ingot, making high fractions of the τ phase difficult [192]. Similar to Mn-Bi, reactive sintering has shown promise as a way to form bulk Mn-Al-C τ phase, albeit with low H_c, but the technique is not yet been proven for binary Mn-Al and requires further study. Mn-Al powders (both with and without C alloying) embedded in a polymer matrix have been made into composite filaments used in 3D printing, demonstrating that bonded Mn-Al magnets can be formed into complex shapes [193,194]. Similar to Mn-Ga and Mn-Bi, Mn-Al magnets stand to benefit from the addition soft magnetic materials to form exchange-coupled composite magnets [195]. However, the cost of adding soft magnetic materials must not undermine the economic advantage of using Mn-Al. Therefore, further research is needed to find the appropriate soft-magnet elements or compounds to simultaneously optimize magnetic performance and cost. Finally, inconsistent reporting of different magnetic parameters (H_c, M_s, M_r, and T_c etc.) in the body of research on Mn-Ga, Mn-Bi, and Mn-Al magnets sometimes makes it difficult to directly compare different techniques. This review recommends that the figure-of-merit $(\mathbf{BH})_{max}$ must be accurately measured in every study of permanent magnet materials to allow for rapid and comprehensive comparisons between different magnets and techniques.

6. Summary

Mn-Ga magnets can be processed into the ferrimagnetic Mn_3Ga $D0_{22}$ phase or the ferromagnetic MnGa $L1_0$ phase. The ferrimagnetic Mn_3Ga $D0_{22}$ phase has a theoretical $(\mathbf{BH})_{max}$ of ~143 kJ/m^3 at a density of 7180 kg/m^3 [8]. The highest reported $D0_{22}$ $(\mathbf{BH})_{max}$ is 14.4 kJ/m^3, ~10% of the theoretical maximum [7], using a 14 day bulk $Mn_{75}Ga_{25}$ anneal at 623 K and ice water quench. In that study the long duration and low temperature of the anneal combined with quenching notably improved the coercivity, possibly by slowing grain size growth. The ferromagnetic MnGa $L1_0$ phase has a $(\mathbf{BH})_{max}$ of ~223 kJ/m^3 at a density of 7300 kg/m^3 [12,13]. The highest reported $L1_0$ $(\mathbf{BH})_{max}$ is ~20 kJ/m^3, which was achieved for both powder and thin film samples, reaching ~9% of the theoretical maximum. The $Mn_{56}Ga_{44}$ $L1_0$ powder was prepared by HEBM for 6 h followed by an 873 K anneal for 20 min [20]. The success of this technique was due to taking care to eliminate any Mn_8Ga_5 phase and find the best compromise between long-range ordering (improving M_s) and grain growth (lowering H_c), both of which increased with annealing temperature. The $Mn_{60}Ga_{40}$ $L1_0$ thin film was made by molecular-beam epitaxy at 573 K onto a (0 0 1) Si-GaAs substrate with a GaAs buffer layer [27]. The balance of M_s and H_c was optimized in this study by modifying the substrate temperature; increasing the substrate temperature increased long-range ordering and M_s but lowered the defect density, decreasing H_c.

Mn-Bi magnets can be processed into the ferromagnetic $B8_1$ low-temperature phase (LTP). The theoretical $(\mathbf{BH})_{max}$ for LTP is ~141 kJ/m^3 at a density of 8900 kg/m^3 [34,35], roughly the same as for $D0_{22}$ Mn_3Ga (~143 kJ/m^3) but less than $L1_0$ MnGa (~223 kJ/m^3). Unlike the other magnets in this review, the magneto-crystalline anisotropy energy of LTP increases with temperature. The highest $(\mathbf{BH})_{max}$ reported is 67 kJ/m^3 for bulk, 72 kJ/m^3 for particulate, and 130 kJ/m^3 for thin film samples. All these values are >47% of the theoretical maximum. The same 67 kJ/m^3 bulk value was achieved by both Nguyen and Nguyen and Poudyal *et al.* using two different procedures for sintering a $Mn_{50}Bi_{50}$ powder, as shown in Table 4 [44,46]. Anisotropic alignment of the precursor powder in a magnetic field prior to sintering was critical for the success of these methods. Substitutional alloying of Mg and Sb for Bi in a $Mn_{50}Bi_{46.5}Mg_3Sb_{0.5}$ bulk sample prepared by hot compaction of melt-spun ribbons followed by magnetic field annealing demonstrated a higher bulk $(\mathbf{BH})_{max}$ of 92 kJ/m^3 [42]. They concluded that the presence of the liquid Bi phase during magnetic annealing was key to developing a strong texture. The 72 kJ/m^3 particulate magnet of $Mn_{60}Bi_{40}$ was formed by melt spinning followed by a 673 K anneal for 30 min, SABM for 30 min, and magnetic alignment in epoxy [56]. Magnetic alignment of the powder in epoxy was the main cause of the high anisotropy in this sample, leading to the high $(\mathbf{BH})_{max}$. A 130 kJ/m^3 thin film magnet was prepared by electron-beam evaporation deposition at 398 K on a glass substrate followed by a 563 K anneal for 1 h and then a 673 K anneal for 1 h [36]. This 100 nm thin film's excellent performance was a result of its equi-atomic $Mn_{50}Bi_{50}$ composition, which led to high volume fraction of LTP and strong easy-axis texture developed perpendicular to the film surface.

Mn-Al magnets can be processed into the ferromagnetic $L1_0$ τ phase. However, the metastable nature of the τ phase has made it difficult to optimize processing conditions and achieve the theoretical $(\mathbf{BH})_{max}$ of ~101 kJ/m^3 at a density of 5200 kg/m^3 [72,73]. This value is ~71% the theoretical $(\mathbf{BH})_{max}$ of $D0_{22}$ Mn_3Ga (~143 kJ/m^3), ~45% the theoretical $(\mathbf{BH})_{max}$ of $L1_0$ MnGa (~223 kJ/m^3), and ~72% the theoretical $(\mathbf{BH})_{max}$ of LTP MnBi (~141 kJ/m^3), giving Mn-Al the lowest theoretical $(\mathbf{BH})_{max}$ of the magnets discussed in this review. Bulk processing methods have shown that a combination of mechanical stress and thermal treatment has produced the highest $(\mathbf{BH})_{max}$ magnets so far, approaching ~56 kJ/m^3 in a $Mn_{53}Al_{45}C_2$ alloy, ~55% the theoretical $(\mathbf{BH})_{max}$ [80]. The highest reported $(\mathbf{BH})_{max}$ for unalloyed $Mn_{54}Al_{46}$ was ~37 kJ/m^3, prepared by homogenization, quenching in deionized water, and annealing at 723 K for 1 h [72]. The success of this method was in forming a controlled ratio of τ phase (73.1 wt.%) to the γ_2 and β phases (26.9 wt.% combined); retaining enough τ for high M_s while the γ_2 and β served as pinning sites to increase H_c. The $(\mathbf{BH})_{max}$ of $(Mn_{55}Al_{45})_{98}C_2$

particles reached ~56 kJ/m^3 for a powder that was ball milled for 4 h then annealed at 773 K for 1 h [162]. Of key importance to the success of this process was the post-milling recovery anneal to optimize the balance between M_s and H_c. This 773 K anneal for 1 h recovered a significant amount of M_s, lost due to chemical disordering of the $L1_0$ during milling, and retained the majority of H_c gained through milling. Unalloyed $Mn_{54}Al_{46}$ particles were reported with $(\mathbf{BH})_{max}$ = ~25 kJ/m^3 when melt spun, annealed at 723 K for 45 min, mechanically ground for 15 min, and magnetically aligned in epoxy [86]. Similar to the results for Mn-Bi, the high $(\mathbf{BH})_{max}$ in this case was due largely to the magnetic alignment of the powder in epoxy, which caused high anisotropy in the sample. The highest thin film $(\mathbf{BH})_{max}$ of ~27 kJ/m^3 was found for $Mn_{50}Al_{50}$ deposited by DC magnetron sputtering onto a (0 0 1) MgO substrate at 773 K and capped with 4 nm of Co [178]. The equi-atomic composition of this sample prevented AFM coupling due to excess Mn atoms, which improved M_s. Additionally, the exchange coupling between the Co cap and the τ phase contributed to improved M_s but at the expense of H_c as the thickness of the cap increased. Thus, the appropriate thickness of 4 nm provided the best tradeoff between M_s and H_c.

Declaration of Competing Interest

The authors declare that they have no known competing financial interests or personal relationships that could have appeared to influence the work reported in this paper.

Acknowledgements

This work was supported by U.S. National Science Foundation grant number 2039698.

Appendix A

The differences between the use of Système international (SI) and centimeter-gram-second (CGS) units is a common source of confusion in the magnetism literature. As a resource for the reader, Table 10 is a brief conversion guide for the units discussed in this review using conversion factors from reference [196].

Table 10
SI to CGS magnetic unit conversion guide.

Property	Symbol	CGS units	SI units	Conversion
Magnetic flux density	**B**	gauss (G)	tesla (T)	1 T = 10^4 G
Magnetic field	**H**	oersted (Oe)	A/m	1 A/m = $4\pi \times 10^{-3}$ Oe
Maximum energy product	$(\mathbf{BH})_{max}$	MGOe	kJ/m^3	1 kJ/m^3 = $4\pi \times 10^{-2}$ MGOe
Magnetization	**M**	emu/cm^3	A/m	1 A/m = 10^{-3} emu/cm^3
Magnetic moment per unit mass	**σ**	emu/g	Am^2/kg	1 Am^2/kg = 1 emu/g

References

[1] Cui J, Kramer M, Zhou L, Liu F, Gabay A, Hadjipanayis G, et al. Current progress and future challenges in rare-earth-free permanent magnets. Acta Mater 2018; 158:118–37. https://doi.org/10.1016/j.actamat.2018.07.049.
[2] Cullity BD, Graham CD. Definitions and Units. Introd. to Magn. Mater. 2009. https://doi.org/10.1002/9780470386323.ch1.
[3] Haynes WM. Hand book of Chemistry and Physics, 97th Edition, 2016-. CRC Press; 2016.
[4] U.S. Geological Survey. Mineral Commodity Summaries; 2020. https://doi.org/10.3133/mcs2020.
[5] Hao Liangyan, Xiong Wei. An evaluation of the Mn–Ga system: Phase diagram, crystal structure, magnetism, and thermodynamic properties. Calphad Comput Coupling Phase Diagrams Thermochem 2020;68:101722. https://doi.org/10.1016/j.calphad.2019.101722.
[6] Niida Hiroshi, Hori Tomiei, Onodera Hideya, Yamaguchi Yasuo, Nakagawa Yasuaki. Magnetization and coercivity of $Mn_{3-\delta}Ga$ alloys with a $D0_{22}$-type structure. J Appl Phys 1996;79(8):5946. https://doi.org/10.1063/1.362115.
[7] Winterlik J, Balke B, Fecher GH, Felser C, Alves MCM, Bernardi F, et al. Structural, electronic, and magnetic properties of tetragonal $Mn_{3-x}Ga$: Experiments and first-principles calculations. Phys Rev B - Condens Matter Mater Phys 2008;77:1–12. https://doi.org/10.1103/PhysRevB.77.054406.
[8] Wei JZ, Wu R, Yang YB, Chen XG, Xia YH, Yang YC, et al. Structural properties and large coercivity of bulk $Mn_{3-x}Ga$ ($0 \leq \times \leq 1.15$). J Appl Phys 2014;115: 15–8. https://doi.org/10.1063/1.4866844.
[9] Krén E, Kádár G. Neutron diffraction study of Mn_3Ga. Solid State Commun 1970;8(20):1653–5. https://doi.org/10.1016/0038-1098(70)90484-9.
[10] Yang Zongxian, Li Jun, Wang Ding-sheng, Zhang Kaiming, Xie Xide. Electronic structure and magnetic properties of δ-MnGa. J Magn Magn Mater 1998;182(3): 369–74. https://doi.org/10.1016/S0304-8853(97)01029-9.
[11] Sakuma Akimasa. Electronic structures and magnetism of CuAu-type MnNi and MnGa. J Magn Magn Mater 1998;187(1):105–12. https://doi.org/10.1016/S0304-8853(98)00115-2.
[12] Lu QM, Wang DJ, Li CH, Zhang HG, Yue M. Recrystallization induced coercivity and magnetic properties enhancement in hot-deformed $L1_0$-$Mn_{1.8}Ga$ magnet. J Magn Magn Mater 2019;474:167–72. https://doi.org/10.1016/j.jmmm.2018.11.005.
[13] Lu QM, Yue M, Zhang HG, Wang ML, Yu F, Huang QZ, et al. Intrinsic magnetic properties of single-phase $Mn_{1+x}Ga$ ($0<x<1$) alloys. Sci Rep 2015;5:1–5. https://doi.org/10.1038/srep17086.
[14] Okamoto Hiroaki. Supplemental literature review of binary phase diagrams: Ag-Sn, Al-Pd, Ba-Gd, Ba-Pr, Cu-P, Dy-Ni, Ga-Mn, Gd-Sb, Gd-Zr, Ho-Te, Lu-Sb, and Mn-Nb. J Phase Equilibria Diffus 2014;35(1):105–16. https://doi.org/10.1007/s11669-013-0262-x.
[15] Mix T, Müller KH, Schultz L, Woodcock TG. Formation and magnetic properties of the $L1_0$ phase in bulk, powder and hot compacted Mn-Ga alloys. J Magn Magn Mater 2015;391:89–95. https://doi.org/10.1016/j.jmmm.2015.04.097.
[16] Kharel P, Huh Y, Al-Aqtash N, Shah VR, Sabirianov RF, Skomski R, et al. Structural and magnetic transitions in cubic Mn_3Ga. J Phys Condens Matter 2014;26 (12):126001. https://doi.org/10.1088/0953-8984/26/12/126001.
[17] Huh Y, Kharel P, Shah VR, Krage E, Skomski R, Shield JE, et al. Magnetic and structural properties of rapidly quenched tetragonal $Mn_{3-x}Ga$ nanostructures. IEEE Trans Magn 2013;49:3277–80. https://doi.org/10.1109/TMAG.2013.2244856.

[18] Balke B, Fecher GH, Winterlik J, Felser C. Mn_3Ga, a compensated ferrimagnet with high Curie temperature and low magnetic moment for spin torque transfer applications. Appl Phys Lett 2007;90:3–6. https://doi.org/10.1063/1.2722206.

[19] Mizukami S, Kubota T, Wu F, Zhang X, Miyazaki T, Naganuma H, et al. Composition dependence of magnetic properties in perpendicularly magnetized epitaxial thin films of Mn-Ga alloys. Phys Rev B - Condens Matter Mater Phys 2012;85(1). https://doi.org/10.1103/PhysRevB.85.014416.

[20] Cui BZ, Marinescu M, Liu JF. Ferromagnetic tetragonal $L1_0$-Type MnGa isotropic nanocrystalline microparticles. IEEE Trans Magn 2013;49:3322–5. https://doi.org/10.1109/TMAG.2013.2245868.

[21] Ener Semih, Skokov Konstantin P, Karpenkov Dmitriy Yu, Kuz'min Michael D, Gutfleisch Oliver. Magnet properties of $Mn_{70}Ga_{30}$ prepared by cold rolling and magnetic field annealing. J Magn Magn Mater 2015;382:265–70. https://doi.org/10.1016/j.jmmm.2015.02.001.

[22] Gong W, Zhao X, Fan W, Feng J, Lin A, He J, et al. Structure, Magnetic Properties, and Coercivity Mechanism of Rapidly Quenched Mn_xGa Ribbons. IEEE Trans Magn 2015;51:10–3. https://doi.org/10.1109/TMAG.2015.2434936.

[23] Saito Tetsuji, Nishimura Ryuji. Hard magnetic properties of Mn-Ga melt-spun ribbons. J Appl Phys 2012;112(8):083901. https://doi.org/10.1063/1.4759351.

[24] Liu Z, Su K, Cheng Y, Ramanujan RV. Structure and Properties Evolutions for Hard Magnetic MnAl and MnGa Based Alloys Prepared by Melt Spinning or Mechanical Milling. Mater Sci Eng with Adv Res 2015;1:12–9. https://doi.org/10.24218/msear.2015.03.

[25] Feng JN, Liu W, Gong WJ, Zhao XG, Kim D, Choi CJ, et al. Magnetic Properties and Coercivity of MnGa Films Deposited on Different Substrates. J Mater Sci Technol 2017;33(3):291–4. https://doi.org/10.1016/j.jmst.2016.04.010.

[26] Rode K, Baadji N, Betto D, Lau YC, Kurt H, Venkatesan M, et al. Site-specific order and magnetism in tetragonal Mn_3Ga thin films. Phys Rev B - Condens Matter Mater Phys 2013;87:1–14. https://doi.org/10.1103/PhysRevB.87.184429.

[27] Zhu Lijun, Nie Shuaihua, Meng Kangkang, Pan Dong, Zhao Jianhua, Zheng Houzhi. Multifunctional $L1_0$-$Mn_{1.5}Ga$ films with ultrahigh coercivity, giant perpendicular magnetocrystalline anisotropy and large magnetic energy product. Adv Mater 2012;24(33):4547–51. https://doi.org/10.1002/adma.v24.3310.1002/adma.201200805.

[28] Sugihara A, Suzuki KZ, Miyazaki T, Mizukami S. Magnetic properties of ultrathin tetragonal Heusler $D0_{22}$-Mn_3Ge perpendicular-magnetized films. J Appl Phys 2015;117:3–7. https://doi.org/10.1063/1.4908144.

[29] Kurt H, Baadji N, Rode K, Venkatesan M, Stamenov P, Sanvito S, et al. Magnetic and electronic properties of $D0_{22}$-Mn_3Ge (001) films. Appl Phys Lett 2012;101(13):132410. https://doi.org/10.1063/1.4754123.

[30] Wu Feng, Mizukami Shigemi, Watanabe Daisuke, Naganuma Hiroshi, Oogane Mikihiko, Ando Yasuo, et al. Epitaxial $Mn_{2.5}Ga$ thin films with giant perpendicular magnetic anisotropy for spintronic devices. Appl Phys Lett 2009;94(12):122503. https://doi.org/10.1063/1.3108085.

[31] Chen D, Aagard RL. MnBi films: High-temperature phase properties and curie-point writing characteristics. J Appl Phys 1970;41(6):2530–4. https://doi.org/10.1063/1.1659259.

[32] Gabay AM, Hadjipanayis GC, Cui J. Effect of Sb substitution on crystal structure, texture and hard magnetic properties of melt-spun MnBi alloys. J Alloys Compd 2019;792:77–86. https://doi.org/10.1016/j.jallcom.2019.03.407.

[33] Chen Tu, Stutius W. The phase transformation and physical properties of the MnBi and $Mn_{1.08}Bi$ compounds. IEEE Trans Magn 1974;10:581–6. https://doi.org/10.1109/TMAG.1974.1058367.

[34] Park J, Hong Y-K, Lee J, Lee W, Kim S-G, Choi C-J. Electronic Structure and Maximum Energy Product of MnBi. Metals (Basel) 2014;4:455–64. https://doi.org/10.3390/met4030455.

[35] Köhler J, Kübler J. Calculated magneto-optical properties of pure and doped MnBi. J Phys Condens Matter 1996;8(44):8681–94. https://doi.org/10.1088/0953-8984/8/44/017.

[36] Zhang Wenyong, Kharel Parashu, Valloppilly Shah, Yue Lanping, Sellmyer David J. High-energy-product MnBi films with controllable anisotropy. Phys Status Solidi Basic Res 2015;252(9):1934–9. https://doi.org/10.1002/pssb:v252.910.1002/pssb:201552075.

[37] Cui Jun, Choi Jung-Pyung, Polikarpov Evgueni, Bowden Mark E, Xie Wei, Li Guosheng, et al. Effect of composition and heat treatment on MnBi magnetic materials. Acta Mater 2014;79:374–81. https://doi.org/10.1016/j.actamat.2014.07.034.

[38] Xiang Zhen, Wang Taolei, Ma Shangjun, Qian Liwei, Luo Zhengyi, Song Yiming, et al. Microstructural evolution and phase transformation kinetics of MnBi alloys. J Alloys Compd 2018;741:951–6. https://doi.org/10.1016/j.jallcom.2018.01.147.

[39] Andresen AF, Hälg W, Fischer P, Stoll E, Eriksson G, Blinc R, et al. The Magnetic and Crystallographic Properties of MnBi Studied by Neutron Diffraction. Acta Chem Scand 1967;21:1543–54. https://doi.org/10.3891/acta.chem.scand.21-1543.

[40] Guo X, Altounian Z, Ström-Olsen JO. Formation of MnBi ferromagnetic phases through crystallization of the amorphous phase. J Appl Phys 1991;69(8):6067–9. https://doi.org/10.1063/1.347771.

[41] Chen Yu-Chun, Gregori Giuliano, Leineweber Andreas, Qu Fei, Chen Chia-Chin, Tietze Thomas, et al. Unique high-temperature performance of highly condensed MnBi permanent magnets. Scr Mater 2015;107:131–5. https://doi.org/10.1016/j.scriptamat.2015.06.003.

[42] Gabay AM, Hadjipanayis GC, Cui J. New anisotropic MnBi permanent magnets by field-annealing of compacted melt-spun alloys modified with Mg and Sb. J Magn Magn Mater 2020;495:165860. https://doi.org/10.1016/j.jmmm.2019.165860.

[43] Si PZ, Yang Y, Yao LL, Qian HD, Ge HL, Park J, et al. Magnetic-field-enhanced reactive synthesis of MnBi from Mn nanoparticles. J Magn Magn Mater 2019;476:243–7. https://doi.org/10.1016/j.jmmm.2018.12.077.

[44] Poudyal Narayan, Liu Xubo, Wang Wei, Nguyen V Vuong, Ma Yilong, Gandha Kinjal, et al. Processing of MnBi bulk magnets with enhanced energy product. AIP Adv 2016;6(5):056004. https://doi.org/10.1063/1.4942955.

[45] Zhang DT, Cao S, Yue M, Liu WQ, Zhang JX, Qiang Y. Structural and magnetic properties of bulk MnBi permanent magnets. J Appl Phys 2011;109(7):07A722. https://doi.org/10.1063/1.3561784.

[46] Van Nguyen V, Nguyen TX. Effects of microstructures on the performance of rare-earth-free MnBi magnetic materials and magnets. Phys B Condens Matter 2018;532:103–7. https://doi.org/10.1016/j.physb.2017.06.018.

[47] Cao J, Huang YL, Hou YH, Zhang GQ, Shi ZQ, Zhong ZC, Liu ZW. Effects of intergranular phase on the coercivity for MnBi magnets prepared by spark plasma sintering. AIP Adv 2018;8. https://doi.org/10.1063/1.5019870.

[48] Liu Y, Zhang J, Cao S, Zhang X, Jia G, Ren Z, et al. Microstructure, crystallization, and magnetization behaviors in MnBi-Bi composites aligned by applied magnetic field. Phys Rev B - Condens Matter Mater Phys 2005;72:1–7. https://doi.org/10.1103/PhysRevB.72.214410.

[49] Mitsui Y, Umetsu RY, Takahashi K, Koyama K. Reactive sintering process of ferromagnetic MnBi under high magnetic fields. J Magn Magn Mater 2018;453:231–5. https://doi.org/10.1016/j.jmmm.2018.01.026.

[50] Qian Hui-Dong, Park Jihoon, Lim Jung Tae, Yang Yang, Si Ping-Zhan, Kim Jong-Woo, et al. Magnetic properties of MnBi bulk magnets with NaCl and C addition. AIP Adv 2019;9(11):115213. https://doi.org/10.1063/1.5122677.

[51] Saito T, Nishimura R, Nishio-Hamane D. Magnetic properties of Mn-Bi melt-spun ribbons. J Magn Magn Mater 2014;349:9–14. https://doi.org/10.1016/j.jmmm.2013.08.031.

[52] Kim Sumin, Moon Hongjae, Jung Hwaebong, Kim Su-Min, Lee Hyun-Sook, Choi-Yim Haein, et al. Magnetic properties of large-scaled MnBi bulk magnets. J Alloys Compd 2017;708:1245–9. https://doi.org/10.1016/j.jallcom.2017.03.067.

[53] Yang JB, Yelon WB, James WJ, Cai Q, Roy S, Ali N. Structure and magnetic properties of the MnBi low temperature phase. J Appl Phys 2002;91:7866–8. https://doi.org/10.1063/1.1451306.

[54] Zhang DT, Geng WT, Yue M, Liu WQ, Zhang JX, Sundararajan JA, et al. Crystal structure and magnetic properties of Mn_xBi_{100-x} (x=48, 50, 55 and 60) compounds. J Magn Magn Mater 2012;324(11):1887–90. https://doi.org/10.1016/j.jmmm.2012.01.017.

[55] Li Bingbing, Ma Yilong, Shao Bin, Li Chunhong, Chen Dengming, Sun JianChun, et al. Preparation and magnetic properties of anisotropic MnBi powders. Phys B Condens Matter 2018;530:322–6. https://doi.org/10.1016/j.physb:2017.11.085.

[56] Cao J, Huang YL, Hou YH, Shi ZQ, Yan XT, Zhong ZC, et al. Microstructure and magnetic properties of MnBi alloys with high coercivity and significant anisotropy prepared by surfactant assisted ball milling. J Magn Magn Mater 2019;473:505–10. https://doi.org/10.1016/j.jmmm.2018.10.052.

[57] Xie W, Polikarpov E, Choi JP, Bowden ME, Sun K, Cui J. Effect of ball milling and heat treatment process on MnBi powders magnetic properties. J Alloys Compd 2016;680:1–5. https://doi.org/10.1016/j.jallcom.2016.04.097.

[58] Chakka VM, Altuncevahir B, Jin ZQ, Li Y, Liu JP. Magnetic nanoparticles produced by surfactant-assisted ball milling. J Appl Phys 2006;99(8):08E912. https://doi.org/10.1063/1.2170593.

[59] Gaunt P. Ferromagnetic domain wall pinning by a random array of inhomogeneities. Philos Mag B Phys Condens Matter; Stat Mech Electron Opt Magn Prop 1983;48(3):261–76. https://doi.org/10.1080/13642818308228288.

[60] Kanari K, Sarafidis C, Gjoka M, Niarchos D, Kalogirou O. Processing of magnetically anisotropic MnBi particles by surfactant assisted ball milling. J Magn Magn Mater 2017;426:691–7. https://doi.org/10.1016/j.jmmm.2016.10.141.

[61] Su KP, Wang J, Wang HO, Huo DX, Li LW, Cao YQ, et al. Strain-induced coercivity enhancement in $Mn_{51}Al_{46}C_3$ flakes prepared by surfactant-assisted ball milling. J Alloys Compd 2015;640:114–7. https://doi.org/10.1016/j.jallcom.2015.04.040.

[62] Ly V, Wu X, Smillie L, Shoji T, Kato A, Manabe A, et al. Low-temperature phase MnBi compound: A potential candidate for rare-earth free permanent magnets. J Alloys Compd 2014;615:S285–90. https://doi.org/10.1016/j.jallcom.2014.01.120.

[63] Saleem Imran Y, Smyth Hugh DC. Micronization of a soft material: Air-jet and micro-ball milling. AAPS PharmSciTech 2010;11(4):1642–9. https://doi.org/10.1208/s12249-010-9542-5.

[64] Rama Rao NV, Hadjipanayis GC. Influence of jet milling process parameters on particle size, phase formation and magnetic properties of MnBi alloy. J Alloys Compd 2015;629:80–3. https://doi.org/10.1016/j.jallcom.2014.12.202.

[65] Wu Q, Li JT, Ge HL, Tu YH, Pan MX, Zhang PY. Coercivity mechanism and FORC analysis of MnBi-based permanent alloy. J Magn Magn Mater 2020;503:166600. https://doi.org/10.1016/j.jmmm.2020.166600.

[66] Chen Di. Preparation and stability of MnBi thin films. J Appl Phys 1971;42(9):3625–8. https://doi.org/10.1063/1.1660779.

[67] Céspedes E, Villanueva M, Navío C, Mompeán FJ, García-Hernández M, Inchausti A, et al. High coercive LTP-MnBi for high temperature applications: From isolated particles to film-like structures. J Alloys Compd 2017;729:1156–64. https://doi.org/10.1016/j.jallcom.2017.09.234.

[68] Qin X, Sui C, Di L, Wang L, Xu X. Studies on preparation and properties of low temperature phase of MnBi prepared by electrodeposition. J Alloys Compd 2019;787:1272–9. https://doi.org/10.1016/j.jallcom.2019.02.109.

[69] Anand K, Pulikkotil JJ, Auluck S. Study of ferromagnetic instability in τ-MnAl, using first-principles. J Alloys Compd 2014;601:234–7. https://doi.org/10.1016/j.jallcom.2014.01.251.

[70] Zeng Q, Baker I, Yan ZC. Nanostructured Mn-Al permanent magnets produced by mechanical milling. J Appl Phys 2006;99:8–11. https://doi.org/10.1063/1.2159187.

[71] Xiang Z, Xu C, Wang T, Song Y, Yang H, Lu W. Enhanced magnetization and energy product in isotropic nanocrystalline Mn55Al45 alloys with boron doping. Intermetallics 2018;101:13–7. https://doi.org/10.1016/j.intermet.2018.07.003.

[72] Park JH, Hong YK, Bae S, Lee JJ, Jalli J, Abo GS, et al. Saturation magnetization and crystalline anisotropy calculations for MnAl permanent magnet. J Appl Phys 2010;107(9):09A731. https://doi.org/10.1063/1.3337640.

[73] Palanisamy Dhanalakshmi, Singh Shailesh, Srivastava Chandan, Madras Giridhar, Chattopadhyay Kamanio. Predicting Pathways for Synthesis of Ferromagnetic τ Phase in Binary Heusler Alloy Al-55 pct Mn Through Understanding of the Kinetics of ε–τ Transformation. Metall Mater Trans A Phys Metall Mater Sci 2016;47(12):6555–68. https://doi.org/10.1007/s11661-016-3756-4.

[74] Palanisamy Dhanalakshmi, Srivastava Chandan, Madras Giridhar, Chattopadhyay Kamanio. High-temperature transformation pathways for metastable ferromagnetic binary Heusler (Al–55 at.%Mn) alloy. J Mater Sci 2017;52(7):4109–19. https://doi.org/10.1007/s10853-016-0673-2.

[75] Shukla Adarsh, Pelton Arthur D. Thermodynamic Assessment of the Al-Mn and Mg-Al-Mn Systems 2009;30(1):28–39. https://doi.org/10.1007/s11669-008-9426-5.

[76] Huang JH, Kuo PC. Phase transformation of Mn-Al alloy powders. Scr Metall Mater 1993;28(1):133–8. https://doi.org/10.1016/0956-716X(93)90550-C.

[77] Si PZ, Qian HD, Choi CJ, Park J, Ge HL. A novel method for measuring the phase transformation temperature and enhanced coercivity in cold-rolled $MnAlC_x$ (x = 0–5) alloys. J Magn Magn Mater 2018;451:540–5. https://doi.org/10.1016/j.jmmm.2017.11.094.

[78] Qian Hui-Dong, Si Ping-Zhan, Choi Chul-Jin, Park Jihoon, Cho Kyung Mox. Phase transformation and magnetic properties of MnAl powders prepared by elemental-doping and salt-assisted ball milling. AIP Adv 2018;8(5):056216. https://doi.org/10.1063/1.5007176.

[79] Shafeie Samrand, Fang Hailiang, Hedlund Daniel, Nyberg Axel, Svedlindh Peter, Gunnarsson Klas, et al. One step towards MnAl-based permanent magnets - Differences in magnetic, and microstructural properties from an intermediate annealing step during synthesis. J Solid State Chem 2019;274:229–36. https://doi.org/10.1016/j.jssc.2019.03.035.

[80] Ohtani T, Kato N, Kojima S, Kojima K, Sakamoto Y, Konno I, et al. Magnetic properties of Mn-Al-C permanent magnet alloys. IEEE Trans Magn 1977;13(5):1328–30. https://doi.org/10.1109/TMAG.1977.1059574.

[81] Tang Nguyen V, Calvayrac F, Bajorek A, Randrianantoandro N. Mechanical alloying and theoretical studies of MnAl(C) magnets. J Magn Magn Mater 2018;462:96–104. https://doi.org/10.1016/j.jmmm.2018.05.001.

[82] Obi O, Burns L, Chen Y, Fitchorov T, Kim S, Hsu K, et al. Magnetic and structural properties of heat-treated high-moment mechanically alloyed MnAlC powders. J Alloys Compd 2014;582:598–602. https://doi.org/10.1016/j.jallcom.2013.08.086.

[83] Mitsui Yoshifuru, Takanaga Yudai, Kobayashi Ryota, Koyama Keiichi. Effect of carbon addition on the phase stability of hcp-Mn-Al. Phys B Condens Matter 2020;595:412379. https://doi.org/10.1016/j.physb:2020.412379.

[84] Lee CT, Han KH, Kook IH, Choo WK. Phase and lattice parameter relationships in rapidly solidified and heat-treated $(Mn_{0.53}Al_{0.47}0)_{100-x}C_x$ pseudo-binary alloys. J Mater Res 1992;7:1690–5. https://doi.org/10.1557/JMR.1992.1690.

[85] Han Kwan Hee, Lee Chong Tak, Choo Woong Kil. On the Position of Carbon Atom in the τ-Phase of Carbon-Doped Mn-Al Permanent Magnets. Phys Status Solidi 1993;136(1):21–8. https://doi.org/10.1002/(ISSN)1521-396X10.1002/pssa:v136:110.1002/pssa:2211360103.

[86] Wei JZ, Song ZG, Yang YCBC, Liu SQ, Du HL, Han JZ, et al. τ-MnAl with high coercivity and saturation magnetization. AIP Adv 2014;4. https://doi.org/10.1063/1.4903773.

[87] Zeng Q, Baker I, Cui JB, Yan ZC. Structural and magnetic properties of nanostructured Mn-Al-C magnetic materials. J Magn Magn Mater 2007;308(2):214–26. https://doi.org/10.1016/j.jmmm.2006.05.032.

[88] Lee CT, Kook IH, Choo WK, Introduction I. Phase and lattice parameter relationships in rapidly solidified and heat-treated (Mn53Al47)100-xCx pseudo-binary alloys; 1992.

[89] Müller C. Metallurgy of the Magnetic t-phase in Mn-Al and Mn-Al-C; 1996.

[90] Marenkin SF, Ril' AI. Al–Mn Hard Magnetic Alloys as Promising Materials for Permanent Magnets (Review). Russ J Inorg Chem 2020;65:2007–19. https://doi.org/10.1134/s003602362014003x.

[91] Fang H, Cedervall J, Casado FJM, Matej Z, Bednarcik J, Ångström J, et al. Insights into formation and stability of τ-$MnAlZ_x$ (Z = C and B). J Alloys Compd 2017;692:198–203. https://doi.org/10.1016/j.jallcom.2016.09.047.

[92] Palanisamy D, Raabe D, Gault B. On the compositional partitioning during phase transformation in a binary ferromagnetic MnAl alloy. Acta Mater 2019;174:227–36. https://doi.org/10.1016/j.actamat.2019.05.037.

[93] Lu Wei, Niu Junchao, Wang Taolei, Xia Kada, Xiang Zhen, Song Yiming, et al. Phase transformation kinetics and microstructural evolution of MnAl permanent magnet alloys. J Alloys Compd 2016;685:992–6. https://doi.org/10.1016/j.jallcom.2016.06.285.

[94] Janotová I, Švec P, Švec P, Mat'ko I, Janičkovič D, Zigo J, et al. Phase analysis and structure of rapidly quenched Al-Mn systems. J Alloys Compd 2017;707:137–41. https://doi.org/10.1016/j.jallcom.2016.11.171.

[95] Van Den Broek JJ, Donkersloot H, Van Tendeloo G, Van Landuyt J. Phase transformations in pure and carbon-doped $Al_{45}Mn_{55}$ alloys. Acta Metall 1979;27(9):1497–504. https://doi.org/10.1016/0001-6160(79)90172-X.

[96] Crisan AD, Vasiliu F, Nicula R, Bartha C, Mercioniu I, Crisan O. Thermodynamic, structural and magnetic studies of phase transformations in MnAl nanocomposite alloys. Mater Charact 2018;140:1–8. https://doi.org/10.1016/j.matchar.2018.03.034.

[97] Dehghan H, Rezayat M, Ebrahimi SA Seyyed. Materials Science & Engineering A Modeling of strain induced transformation during hot deformation of an Mn – Al – C alloy. Mater Sci Eng A 2020;776:139006. https://doi.org/10.1016/j.msea.2020.139006.

[98] Hoydick DP, Palmiere EJ, Soffa WA. On the formation of the metastable $L1_0$ phase in manganese-aluminum-base permanent magnet materials. Scr Mater 1997; 36:151–6. https://doi.org/10.1016/S1359-6462(96)00356-9.

[99] Kinemuchi Y, Fujita A, Ozaki K. High-pressure synthesis of $L1_0$ MnAl with near-stoichiometric composition. Dalt Trans 2016;45(27):10936–41. https://doi.org/10.1039/C6DT00947F.

[100] Kim YJ, Perepezko JH. The thermodynamics and competitive kinetics of metastable τ phase development in MnAl-base alloys. Mater Sci Eng A 1993;163(1): 127–34. https://doi.org/10.1016/0921-5093(93)90586-4.

[101] Yanar C, Wiezorek JMK, Soffa WA, Radmilovic V. Massive transformation and the formation of the ferromagnetic $L1_0$ phase in manganese-aluminum-based alloys. Metall Mater Trans A Phys Metall Mater Sci 2002;33(8):2413–23. https://doi.org/10.1007/s11661-002-0363-3.

[102] Sologubenko Alla S, Müllner Peter, Heinrich Helge, Kostorz Gernot. On the plate-like τ-phase formation in MnAl–C alloys. Zeitschrift Für Met 2004;95(6): 486–91. https://doi.org/10.3139/146.017981.

[103] Kojima S, Ohtani T, Kato N, Kojima K, Sakamoto Y, Konno I, et al. Crystal transformation and orientation of Mn-Al-C hard magnetic alloy 2008;768:768–9. https://doi.org/10.1063/1.30281.

[104] Hoydick DP, Palmiere EJ, Soffa WA. Microstructural development in MnAl-base permanent magnet materials: New perspectives. J Appl Phys 1997;81(8): 5624–6. https://doi.org/10.1063/1.364619.

[105] Wiezorek Jorg MK, Kulovits Andreas K, Yanar Cagatay, Soffa William A. Grain boundary mediated displacive-diffusional formation of τ-phase MnAl. Metall Mater Trans A Phys Metall Mater Sci 2011;42(3):594–604. https://doi.org/10.1007/s11661-010-0308-1.

[106] Si PZ, Qian HD, Choi CJ, Park J, Han S, Ge HL, et al. In situ observation of phase transformation in MnAl(C) magnetic materials. Materials (Basel) 2017;10. https://doi.org/10.3390/ma10091016.

[107] Müllner P, Bürgler BE, Heinrich H, Sologubenko AS, Kostorz G. Observation of the shear mode of the $\varepsilon \rightarrow \tau$ phase transformation in a Mn-Al-C single crystal. Philos Mag Lett 2002;82(2):71–9. https://doi.org/10.1080/09500830110103225.

[108] Genc Ayse Merve, Acar Ozgun, Turan Servet, Kalay Ilkay, Savacı Umut, Kalay Yunus Eren. Investigation of phase selection hierarchy in Mn–Al alloys. Intermetallics 2019;115:106617. https://doi.org/10.1016/j.intermet.2019.106617.

[109] Shao Z, Zhao H, Zeng J, Zhang Y, Yang W, Lai Y, et al. One step preparation of pure τ-MnAl phase with high magnetization using strip casting method. AIP Adv 2017;7. https://doi.org/10.1063/1.4974277.

[110] Saravanan P, Vinod VTP, Černík M, Selvapriya A, Chakravarty D, Kamat SV. Processing of Mn-Al nanostructured magnets by spark plasma sintering and subsequent rapid thermal annealing. J Magn Magn Mater 2015;374:427–32. https://doi.org/10.1016/j.jmmm.2014.08.076.

[111] Muñoz-Rodríguez C, Feng L, Palmero EM, Mix T, Rial J, Olsson F, et al. Fabrication of bulk τ MnAl–C magnets by hot-pressing from ε-phase gas-atomized and milled powder. J Alloys Compd 2020;847:156361. https://doi.org/10.1016/j.jallcom.2020.156361.

[112] Sologubenko AS, Zurich ETH, Heinrich H, Woligarten M. The effect of composition and stress on the selection of epsilon to tau transformation modes in MnAl-C. J Phys IV Fr 2003;112:1071.

[113] Arapan S, Nieves P, Cuesta-López S, Gusenbauer M, Oezelt H, Schrefl T, et al. Influence of antiphase boundary of the MnAl τ -phase on the energy product. Phys Rev Mater 2019;3:1–5. https://doi.org/10.1103/PhysRevMaterials.3.064412.

[114] Bance S, Bittner F, Woodcock TG, Schultz L, Schrefl T. Role of twin and anti-phase defects in MnAl permanent magnets. Acta Mater 2017;131:48–56. https://doi.org/10.1016/j.actamat.2017.04.004.

[115] Bittner F, Schultz L, Woodcock TG. Twin-like defects in $L1_0$ ordered τ-MnAl-C studied by EBSD. Acta Mater 2015;101:48–54. https://doi.org/10.1016/j.actamat.2015.08.044.

[116] Jia Y, Wu Y, Zhao S, Zuo S, Skokov KP, Gutfleisch O, et al. $L1_0$ rare-earth-free permanent magnets: The effects of twinning versus dislocations in Mn-Al magnets. Phys Rev Mater 2020;4:1–17. https://doi.org/10.1103/PhysRevMaterials.4.094402.

[117] Bittner F, Freudenberger J, Schultz L, Woodcock TG. The impact of dislocations on coercivity in $L1_0$-MnAl. J Alloys Compd 2017;704:528–36. https://doi.org/10.1016/j.jallcom.2017.02.028.

[118] Si Pingzhan, Qian Huidong, Wang Xinyou, Yang Yang, Park Jihoon, Ge Hongliang, et al. High-Pressure Synthesis of High Coercivity Bulk MnAl-C Magnets from Melt-Spun Ribbons. J Electron Mater 2019;48(2):794–8. https://doi.org/10.1007/s11664-018-6798-0.

[119] Jia Y, Wu Y, Zhao S, Wang J, Jiang C. Relation between solidification microstructure and coercivity in MnAl permanent-magnet alloys. Intermetallics 2018;96: 41–8. https://doi.org/10.1016/j.intermet.2018.02.011.

[120] Zhang C, Zhang T, Wang J, Zhao S, Wu Y, Jiang C. Anisotropic single-variant of $(Mn_{54}Al_{46})_{97}C_3$. Scr Mater 2018;143:72–6. https://doi.org/10.1016/j.scriptamat.2017.09.008.

[121] Kubo T, Ohtani T, Kojima S, Kato N, Kojima K, Sakamoto Y, et al. Machinable anisotropic permanent magnets of Mn-Al-C Alloys. 3,976,519; 1976.

[122] Kubo T, Ohtani T, Kojima S, Kato N, Kojima K, Sakamoto Y, et al. Anisotropic permanent magnet of Mn-Al-C alloy. 4,023,991; 1977.

[123] Thielsch J, Bittner F, Woodcock TG. Magnetization reversal processes in hot-extruded τ-MnAl-C. J Magn Magn Mater 2017;426:25–31. https://doi.org/10.1016/j.jmmm.2016.11.045.

[124] Landuyt JV, Tendeloo GV, Broek JJVD, Donkersloot H, Zijlstra H. Defect structure and magnetic properties of MnAI permanent magnet materials. IEEE Trans Magn 1978;14:679–81. https://doi.org/10.1109/TMAG.1978.1059949.

[125] Sakamoto Y, Ohtani T, Kojima S. New MnA1C permanent magnets exhibiting macroscopically-plane magnetic-anisotropy. IEEE Trans Magn 1980;16:1056–8. https://doi.org/10.1109/TMAG.1980.1060672.

[126] Ibata A, Sakamoto Y. Permanent Mn-Al-C alloy magnets and method for making same. 4,579,607; 1986.

[127] Dehghan H, Seyyed Ebrahimi SA. Effect of hot deformation conditions on magnetic properties of rare earth free magnetic Mn-Al-C alloy. J Magn Magn Mater 2019;477:55–61. https://doi.org/10.1016/j.jmmm.2018.12.108.

[128] Madugundo Rajasekhar, Koylu-Alkan Ozlem, Hadjipanayis George C. Bulk Mn-Al-C permanent magnets prepared by various techniques. AIP Adv 2016;6(5): 056009. https://doi.org/10.1063/1.4943242.

[129] Rial J, Švec P, Švec P, Bollero A, Deledda S. Coercivity development in MnAl ribbons by microstructural modifications achieved through cold-rolling process. J Magn Magn Mater 2021;529:167826. https://doi.org/10.1016/j.jmmm.2021.167826.

[130] Chaturvedi A, Yaqub R, Baker I. Microstructure and magnetic properties of bulk nanocrystalline MnAl. Metals (Basel) 2014;4:20–7. https://doi.org/10.3390/met4010020.

[131] Si PZ, Park J, Qian HD, Choi CJ, Li YS, Ge HL. Enhanced magnetic performance of bulk nanocrystalline MnAl-C prepared by high pressure compaction of gas atomized powders. Bull Mater Sci 2019;42:6–11. https://doi.org/10.1007/s12034-019-1768-6.

[132] Tyrman Muriel, Ahmim Smail, Pasko Alexandre, Etgens Victor, Mazaleyrat Frédéric, Quetel-Weben Simon, et al. Anisotropy of the ferromagnetic L10 phase in the Mn-Al-C alloys induced by high-pressure spark plasma sintering. AIP Adv 2018;8(5):056217. https://doi.org/10.1063/1.5007241.

[133] Wang HX, Si PZ, Jiang W, Lee JG, Choi CJ, Liu JJ, et al. Structural Stabilizing Effect of Zn Substitution on MnAl and Its Magnetic Properties. Open J Microphys 2011;01(02):19–22. https://doi.org/10.4236/ojm.2011.12003.

[134] Kontos Sofia, Fang Hailiang, Li Jiheng, Delczeg-Czirjak Erna Krisztina, Shafeie Samrand, Svedlindh Peter, et al. Measured and calculated properties of B-doped τ-phase MnAl – A rare earth free permanent magnet. J Magn Magn Mater 2019;474:591–8. https://doi.org/10.1016/j.jmmm.2018.11.006.

[135] Si Ping-Zhan, Choi Chul-Jin, Park Jihoon, Ge Hong-Liang, Du Juan. Phase transformation and enhanced coercivity in B-N-doped MnAl nanocrystalline bulk alloys prepared by high pressure torsion. AIP Adv 2020;10(1):015320. https://doi.org/10.1063/1.5130064.

[136] Mican Sever, Benea Diana, Hirian Razvan, Gavrea Radu, Isnard Olivier, Pop Viorel, et al. Structural, electronic and magnetic properties of the $Mn_{50}Al_{46}Ni_4$ alloy. J Magn Magn Mater 2016;401:841–7. https://doi.org/10.1016/j.jmmm.2015.11.011.

[137] Gavrea R, Hirian R, Mican S, Benea D, Isnard O, Coldea M, et al. Structural, electronic and magnetic properties of the $Mn_{54-x}Al_{46}Ti_x$ (x = 2; 4) alloys. Intermetallics 2017;82:101–6. https://doi.org/10.1016/j.intermet.2016.11.012.

[138] Feng Le, Nielsch Kornelius, Woodcock Thomas George. Enhanced thermal stability of the τ-phase in MnAl-C alloys with Ni additions. J Alloys Compd 2021; 871:159554. https://doi.org/10.1016/j.jallcom.2021.159554.
[139] Geng Yunlong, Lucis Michael J, Rasmussen Pamela, Shield Jeffrey E. Phase transformation and magnetic properties of rapidly solidified Mn-Al-C alloys modified with Zr. J Appl Phys 2015;118(3):033905. https://doi.org/10.1063/1.4927289.
[140] Xiang Zhen, Baiwen·Deng, Zhang Xiang, Wang Xiao, Cui Erbiao, Yu Lunzhou, et al. Nanocrystalline MnAlV rare-earth-free Permanent Magnetic Alloys with Improved Magnetization and Thermal Stability. Intermetallics 2020;116:106638. https://doi.org/10.1016/j.intermet.2019.106638.
[141] Zhao Shuang, Wu Yuye, Wang Jingmin, Jia Yuxiao, Zhang Tianli, Zhang Tianle, et al. Realization of large coercivity in MnAl permanent-magnet alloys by introducing nanoprecipitates. J Magn Magn Mater 2019;483:164–8. https://doi.org/10.1016/j.jmmm.2019.03.103.
[142] Mix T, Bittner F, Müller KH, Schultz L, Woodcock TG. Alloying with a few atomic percent of Ga makes MnAl thermodynamically stable. Acta Mater 2017;128: 160–5. https://doi.org/10.1016/j.actamat.2017.02.011.
[143] Mix T, Woodcock TG. Advanced thermal stability investigations of the Mn–Al-Ga system. Results Mater 2020;5:100068. https://doi.org/10.1016/j.rinma.2020.100068.
[144] Zhao S, Wu Y, Jiao Z, Jia Y, Xu Y, Wang J, et al. Evolution of Intrinsic Magnetic Properties in $L1_0$ Mn-Al Alloys Doped with Substitutional Atoms and Correlated Mechanism: Experimental and Theoretical Studies. Phys Rev Appl 2019;11:1. https://doi.org/10.1103/PhysRevApplied.11.064008.
[145] Klemmer T, Hoydick D, Okumura H, Zhang B, Soffa WA. Magnetic Hardening and Coercitiy in $L1_0$ ordered FePd Ferromagents. Scripta Metallurgica et Materialia 1995;33:1793–805.
[146] Xiang Zhen, Wang Xiao, Song Yiming, Yu Lunzhou, Cui Erbiao, Deng Baiwen, et al. Effect of cooling rates on the microstructure and magnetic properties of MnAl permanent magnetic alloys. J Magn Magn Mater 2019;475:479–83. https://doi.org/10.1016/j.jmmm.2018.12.003.
[147] Marshall LG, McDonald IJ, Lewis LH. Quantification of the strain-induced promotion of τ-MnAl via cryogenic milling. J Magn Magn Mater 2016;404:215–20. https://doi.org/10.1016/j.jmmm.2015.12.006.
[148] Lu Wei, Niu Junchao, Wang Taolei, Xia Kada, Xiang Zhen, Song Yiming, et al. Low-energy mechanically milled τ-phase MnAl alloys with high coercivity and magnetization. J Alloys Compd 2016;675:163–7. https://doi.org/10.1016/j.jallcom.2016.03.098.
[149] Park Jihoon, Qian Hui-Dong, Si Ping-Zhan, Choi Chul-Jin. Phase Transformation of Micrometer-Sized Mn – Al –. C 2018;54(1):1–3.
[150] Baker I. Nanostructured Mn-Al permanent magnets and methods of producing same. WO 2008/048277 A2; 2008.
[151] Baker I. Nanostructured Mn-Al permanent magnets and methods of producing same. US 8,999,233 B2; 2015.
[152] Pareti L, Bolzoni F, Leccabue F, Ermakov AE. Magnetic anisotropy of MnAl and MnAlC permanent magnet materials. J Appl Phys 1986;59(11):3824–8. https://doi.org/10.1063/1.336723.
[153] Singh N, Mudgil V, Anand K, Srivastava AK, Kotnala RK, Dhar A. Influence of processing on structure property correlations in τ-MnAl rare-earth free permanent magnet material. J Alloys Compd 2015;633:401–7. https://doi.org/10.1016/j.jallcom.2015.02.041.
[154] Lee Jung-Goo, Wang Xiao-Lei, Zhang Zhi-Dong, Choi ChuI-Jin. Effect of mechanical milling and heat treatment on the structure and magnetic properties of gas atomized Mn-Al alloy powders. Thin Solid Films 2011;519(23):8312–6. https://doi.org/10.1016/j.tsf.2011.03.094.
[155] Jian H, Skokov KP, Gutfleisch O. Microstructure and magnetic properties of Mn-Al-C alloy powders prepared by ball milling. J Alloys Compd 2015;622:524–8. https://doi.org/10.1016/j.jallcom.2014.10.138.
[156] Su KP, Chen XX, Wang HO, Huo DX, Liu ZW. Effect of milling on the structure and magnetic properties in $Mn_{54}Al_{46}$ flakes prepared by surfactant-assisted ball milling. Mater Charact 2016;114:263–6. https://doi.org/10.1016/j.matchar.2016.03.011.
[157] Lucis MJ, Prost TE, Jiang X, Wang M, Shield JE. Phase transitions in mechanically milled Mn-Al-C permanent magnets. Metals (Basel) 2014;4:130–40. https://doi.org/10.3390/met4020130.
[158] Jia Yuxiao, Wu Yuye, Zhao Shuang, Jiang Chengbao. Tailoring precursor and medium of ball milling to optimize magnetic properties in Mn-Al bonded permanent magnets. J Magn Magn Mater 2021;530:167933. https://doi.org/10.1016/j.jmmm.2021.167933.
[159] Chaturvedi Anurag, Yaqub Rumana, Baker Ian. A comparison of τ-MnAl particulates produced via different routes. J Phys Condens Matter 2014;26(6):064201. https://doi.org/10.1088/0953-8984/26/6/064201.
[160] Zhao Shuang, Wu Yuye, Zhang Chi, Wang Jingmin, Fu Zhongheng, Zhang Ruifeng, et al. Stabilization of τ-phase in carbon-doped MnAl magnetic alloys. J Alloys Compd 2018;755:257–64. https://doi.org/10.1016/j.jallcom.2018.04.318.
[161] Liu ZW, Chen C, Zheng ZG, Tan BH, Ramanujan RV. Phase transitions and hard magnetic properties for rapidly solidified MnAl alloys doped with C, B, and rare earth elements. J Mater Sci 2012;47(5):2333–8. https://doi.org/10.1007/s10853-011-6049-8.
[162] Fang Hailiang, Kontos Sofia, Ångström Jonas, Cedervall Johan, Svedlindh Peter, Gunnarsson Klas, et al. Directly obtained τ-phase MnAl, a high performance magnetic material for permanent magnets. J Solid State Chem 2016;237:300–6. https://doi.org/10.1016/j.jssc.2016.02.031.
[163] Fang Hailiang, Cedervall Johan, Hedlund Daniel, Shafeie Samrand, Deledda Stefano, Olsson Fredrik, et al. Structural, microstructural and magnetic evolution in cryo milled carbon doped MnAl. Sci Rep 2018;8(1). https://doi.org/10.1038/s41598-018-20606-8.
[164] Øygarden V, Rial J, Bollero A, Deledda S. Phase-pure τ-MnAlC produced by mechanical alloying and a one-step annealing route. J Alloys Compd 2019;779: 776–83. https://doi.org/10.1016/j.jallcom.2018.11.175.
[165] Rial J, Švec P, Palmero EM, Camarero J, Švec P, Bollero A. Severe tuning of permanent magnet properties in gas-atomized MnAl powder by controlled nanostructuring and phase transformation. Acta Mater 2018;157:42–52. https://doi.org/10.1016/j.actamat.2018.07.010.
[166] Rial J, Palmero EM, Bollero A. Efficient Nanostructuring of Isotropic Gas-Atomized MnAl Powder by Rapid Milling (30 s). Engineering 2020;6(2):173–7. https://doi.org/10.1016/j.eng.2019.03.013.
[167] Su KP, Wang HO, Huang S, Chen XX, Liu JJ, Huo DX, et al. Magnetic anisotropy and enhanced remanence in textured polycrystalline MnAlCuC-based flakes. J Mater Sci 2018;53(13):9823–9. https://doi.org/10.1007/s10853-018-2274-8.
[168] Su KP, Hu SL, Wang HO, Huang S, Chen XX, Liu JJ, et al. Structural and magnetic properties of $Mn_{54}Al_{46}Cu_4C_3$ flakes obtained by surfactant-assisted ball milling. Mater Res Express 2019;6. https://doi.org/10.1088/2053-1591/ab4227.
[169] Saito T. Magnetic properties of Mn-Al-C alloy powders produced by mechanical grinding. J Appl Phys 2005;97:2003–6. https://doi.org/10.1063/1.1852330.
[170] Sato T, Ohsuna T, Kaneko Y. Enhanced saturation magnetization in perpendicular $L1_0$-MnAl films upon low substitution of Mn by 3d transition metals. J Appl Phys 2016;120(24):243903. https://doi.org/10.1063/1.4972972.
[171] Manchanda P, Kashyap A, Shield JE, Lewis LH, Skomski R. Magnetic properties of Fe-doped MnAl. J Magn Magn Mater 2014;365:88–92. https://doi.org/10.1016/j.jmmm.2014.04.007.
[172] Huang JH, Kuo PC, Shen SC. High Coercivity and High Saturation Magnetization: Mn-Al Thin Films. IEEE Trans Magn 1995;31:2494–8. https://doi.org/10.1109/20.406550.
[173] Hosoda Masaki, Oogane Mikihiko, Kubota Miho, Kubota Takahide, Saruyama Haruaki, Iihama Satoshi, et al. Fabrication of $L1_0$-MnAl perpendicularly magnetized thin films for perpendicular magnetic tunnel junctions. J Appl Phys 2012;111(7):07A324. https://doi.org/10.1063/1.3676428.
[174] Takata F, Gushi T, Anzai A, Toko K, Suemasu T. Structural characterization and magnetic properties of $L1_0$-MnAl films grown on different underlayers by molecular beam epitaxy. J Cryst Growth 2018;486:19–23. https://doi.org/10.1016/j.jcrysgro.2018.01.008.
[175] Yasutomi Y, Ito K, Sanai T, Toko K, Suemasu T. Perpendicular magnetic anisotropy of Mn_4N films on MgO(001) and SrTiO3(001) substrates. J Appl Phys 2014; 115:10–3. https://doi.org/10.1063/1.4867955.
[176] Navío C, Villanueva M, Céspedes E, Mompeán F, García-Hernández M, Camarero J, et al. Ultrathin films of $L1_0$-MnAl on GaAs (001): A hard magnetic MnAl layer onto a soft Mn-Ga-As-Al interface. APL Mater 2018;6(10):101109. https://doi.org/10.1063/1.5050852.
[177] Mao Si-Wei, Lu Jun, Yang Long, Ruan Xue-Zhong, Wang Hai-Long, Wei Da-Hai, et al. Ultrafast Magnetization Precession in Perpendicularly Magnetized $L1_0$-MnAl Thin Films with Co_2MnSi Buffer Layers. Chinese Phys Lett 2020;37(5):058501. https://doi.org/10.1088/0256-307X/37/5/058501.
[178] You J, Guo Y. Plasma enhanced atomic layer deposition of Co thin film on τ-MnAl for effective magnetic exchange coupling and enhanced energy products. J Alloys Compd 2018;758:116–21. https://doi.org/10.1016/j.jallcom.2018.05.075.

[179] Wang ZH, Choi CJ, Kim BK, Kim JC, Zhang ZD. Characterization and magnetic properties of carbon-coated cobalt nanocapsules synthesized by the chemical vapor-condensation process. Carbon N Y 2003;41(9):1751–8. https://doi.org/10.1016/S0008-6223(03)00127-1.
[180] Hsu JS, Adams DJ, Scudiere MB, Jenkins SM, Ott GW, Mckeever JW, et al. Low-Inertia Axial-Gap Permanent-Magnet Motors; 2009.
[181] Nakamura H. The current and future status of rare earth permanent magnets. Scr Mater 2018;154:273–6. https://doi.org/10.1016/j.scriptamat.2017.11.010.
[182] Palasyuk A, Blomberg E, Prozorov R, Yue L, Kramer MJ, Mccallum RW, et al. Advances in characterization of non-rare-earth permanent magnets: Exploring commercial alnico grades 5–7 and 9. Jom 2013;65(7):862–9. https://doi.org/10.1007/s11837-013-0618-z.
[183] Rodrigues D, da Silva BFA, Janasi SR, de Campos MF. Rare-earth bonded hybrid magnets produced with the addition of strontium ferrite powders. Proc Int Euro Powder Metall Congr Exhib Euro PM 2012;2012:1.
[184] Zwyssig C, Kolar JW, Thaler W, Vohrer M. Design of a 100 W, 500000 rpm permanent-magnet generator for mesoscale gas turbines. Conf Rec - IAS Annu Meet (IEEE Ind Appl Soc 2005;1:253–60. https://doi.org/10.1109/IAS.2005.1518318.
[185] Kramer MJ, McCallum RW, Anderson IA, Constantinides S. Prospects for non-rare earth permanent magnets for traction motors and generators. Jom 2012;64 (7):752–63. https://doi.org/10.1007/s11837-012-0351-z.
[186] Kneller EF, Hawig R. The Exchange-Spring Magnet 1991;27:3588–600.
[187] Skomski Ralph, Coey JMD. Giant energy product in nanostructured two-phase magnets. Phys Rev B 1993;48(21):15812–6. https://doi.org/10.1103/PhysRevB.48.15812.
[188] Malyeyev A, Titov I, Bender P, Bersweiler M, Pipich V, Mühlbauer S, et al. Neutron study of magnetic correlations in rare-earth-free Mn-Bi magnets 2020:1–7.
[189] Ma YL, Liu XB, Gandha K, Vuong NV, Yang YB, Yang JB, et al. Preparation and magnetic properties of MnBi-based hard/soft composite magnets. J Appl Phys 2014;115(17):17A755. https://doi.org/10.1063/1.4868078.
[190] Krakhmalev P, Yadroitsev I, Baker I, Yadroitsava I. Manufacturing of intermetallic Mn-46%Al by laser powder bed fusion. Procedia CIRP 2018;74:64–7. https://doi.org/10.1016/j.procir.2018.08.031.
[191] Radulov IA, Popov VV, Koptyug A, Maccari F, Kovalevsky A, Essel S, et al. Production of net-shape Mn-Al permanent magnets by electron beam melting. Addit Manuf 2019;30:100787. https://doi.org/10.1016/j.addma.2019.100787.
[192] Lee Jung-Goo, Li Pu, Choi Chul-Jin, Dong Xing-Long. Synthesis of Mn-Al alloy nanoparticles by plasma arc discharge. Thin Solid Films 2010;519(1):81–5. https://doi.org/10.1016/j.tsf.2010.07.063.
[193] Palmero Ester M, Rial Javier, de Vicente Javier, Camarero Julio, Skårman Björn, Vidarsson Hilmar, et al. Development of permanent magnet MnAlC/polymer composites and flexible filament for bonding and 3D-printing technologies. Sci Technol Adv Mater 2018;19(1):465–73. https://doi.org/10.1080/14686996.2018.1471321.
[194] Thongsamrit W, Charoensuk T, Saetang P, Jantaratana P. Effects of Carbon Doping and Annealing Temperature on Magnetic MnAl Powders and MnAl Polymeric Composites; 2021.
[195] Lewis LH, Shield JE, Katayun BV. Rare earth - free permanent magnetic material. US 2018 / 0114614 A1; 2018.
[196] Moskowitz BM. Fundamental Physical Constants and Conversion Factors. Glob. Earth Phys. A Handb. Phys. Constants, American Geophysical Union 1995: 346–55. https://doi.org/10.1029/RF001p0346.
[197] Rama Rao NV, Gabay AM, Hu X, Hadjipanayis GC. Fabrication of anisotropic MnBi nanoparticles by mechanochemical process. J Alloys Compd 2014;586: 349–52. https://doi.org/10.1016/j.jallcom.2013.10.067.
[198] Chraplyvy A, Croat JJ, Herbst JF. Selective magnetization of manganese-aluminum alloys. 4,312,684; 1982.
[199] Qian Hui-Dong, Si Ping-Zhan, Park Jihoon, Cho Kyung Mox, Choi Chul-Jin. Structure and Magnetic Properties of Nanocrystalline MnAl-C Prepared by Solid-State Reaction and High-Pressure Compaction. J Electron Mater 2019;48(3):1395–9. https://doi.org/10.1007/s11664-018-06848-2.
[200] Law JY, Rial J, Villanueva M, López N, Camarero J, Marshall LG, et al. Study of phases evolution in high-coercive MnAl powders obtained through short milling time of gas-atomized particles. J Alloys Compd 2017;712:373–8. https://doi.org/10.1016/j.jallcom.2017.04.038.